Jordan Journal of
PHYSICS
An International Peer-Reviewed Research Journal

Volume 9, No. 2, 2016, 1438 H

Jordan Journal of Physics (*JJP*): An International Peer-Reviewed Research Journal funded by the Scientific Research Support Fund, Ministry of Higher Education and Scientific Research, Jordan, and published biannually by the Deanship of Research and Graduate Studies, Yarmouk University, Irbid, Jordan.

Manuscripts should be submitted to:

Prof. Nehad M. Tashtoush
Editor-in-Chief, Jordan Journal of Physics
Deanship of Research and Graduate Studies
Yarmouk University-Irbid-Jordan
Tel. 00 962 2 7211111 Ext. 2075
E-mail: *jjp@yu.edu.jo*
Website: *http://Journals.yu.edu.jo/jjp*

Jordan Journal of
PHYSICS
An International Peer-Reviewed Research Journal

Volume 9, No. 2, 2016, 1438 H

INTERNATIONAL ADVISORY BOARD

Prof. Dr. Ahmad Saleh
Department of Physics, Yarmouk University, Irbid, Jordan.
salema@yu.edu.jo

Prof. Dr. Aurore Savoy-Navarro
LPNHE Universite de Paris 6/IN2P3-CNRS, Tour 33, RdC 4, Place Jussieu, F 75252, Paris Cedex 05, France.
auore@lpnhep.in2p3.fr

Prof. Dr. Bernard Barbara
Laboratoire Louis Neel, Salle/Room: D 108, 25, Avenue des Martyrs BP 166, 38042-Grenoble Cedex 9, France.
Barbara@grenoble.cnrs.fr

Prof. Dr. Bruno Guiderdoni
Observatoire Astronomique de Lyon, g, avenue Ch. Antre-F-69561, Saint Genis Laval Cedex, France.
Bruno.guiderdoni@olos.univ-lyon1.fr

Prof. Dr. Buford Price
Physics Department, University of California, Berkeley, CA 94720, U. S. A.
bprice@berkeley.edu

Prof. Dr. Colin Cough
School of Physics and Astronomy, University of Birmingham, B15 2TT, U. K.
c.gough@bham.ac.uk

Prof. Dr. Desmond Cook
Department of Physics, Condensed Matter and Materials Physics Research Group, Old Dominion University, Norfolk, Virginia 23529, U. S. A.
Dcook@physics.odu.edu

Prof. Dr. Evgeny Sheshin
MIPT, Institutskij per. 9, Dogoprudnyi 141700, Russia.
sheshin@lafeet.mipt.ru

Prof. Dr. Hans Ott
Laboratorium Fuer Festkorperphysik, ETH Honggerberg, CH-8093 Zurich, Switzerland.
ott@solid.phys.ethz.ch

Prof. Dr. Herwig Schopper
President SESAME Council, Chairman Scientific Board UNESCO IBSP Programme, CERN, 1211 Geneva, Switzerland.
Herwig.Schopper@cern.ch

Prof. Dr. Humam Ghassib
Department of Physics, The University of Jordan, Amman 11942, Jordan.
humamg@ju.edu.jo

Prof. Dr. Ingo Hofmann
GSI Darmstadt, Planckstr. 1, 64291, Darmstadt, Germany.
i.hofmann@gsi.de

Prof. Dr. Jozef Lipka
Department of Nuclear Physics and Technology, Slovak University of Technology, Bratislava, Ilkovicova 3, 812 19 Bratislava, Slovakia.
Lipka@elf.stuba.sk

Prof. Dr. Khalid Touqan
Chairman of Jordan Atomic Energy Commission, Amman, Jordan.

Prof. Dr. Mark J. Hagmann
Desert Electronics Research Corporation, 762 Lacey Way, North Salt Lake 84064, Utah, U. S. A.
MHagmann@NewPathResearch.Com.

Prof. Dr. Nasr Zubeidey
President*: Al-Zaytoonah University of Jordan, Amman, Jordan.*
President@alzaytoonah.edu.jo

Prof. Dr. Patrick Roudeau
Laboratoire de I'Accelerateur, Lineaire (LAL), Universite Paris-Sud 11, Batiment 200, 91898 Orsay Cedex, France.
roudeau@mail.cern.ch

Prof. Dr. Paul Chu
Department of Physics, University of Houston, Houston, Texas 77204-5005, U. S. A.
Ching-Wu.Chu@mail.uh.edu

Prof. Dr. Peter Dowben
Nebraska Center for Materials and Nanoscience, Department of Physics and Astronomy, 255 Behlen Laboratory (10th and R Streets), 116 Brace Lab., P. O. Box 880111, Lincoln, NE 68588-0111, U. S. A.
pdowben@unl.edu

Prof. Dr. Peter Mulser
Instiute fuer Physik, T.U. Darmstadt, Hochschulstr. 4a, 64289 Darmstadt, Germany.
Peter.mulser@physik.tu-darmstadt.de

Prof. Dr. Rasheed Azzam
Department of Electrical Engineering, University of New Orleans New Orleans, Louisiana 70148, U. S. A.
razzam@uno.edu

Dr. Richard G. Forbes
University of Surrey, FEPS (X1), Guildford, Surrey GU2 7XH, U. K.
R.Forbes@surrey.ac.uk

Prof. Dr. Roy Chantrell
Physics Department, York University, York, YO10 5DD, U. K.
Rc502@york.ac.uk

Prof. Dr. Shawqi Al-Dallal
Department of Physics, Faculty of Science, University of Bahrain, Manamah, Kingdom of Bahrain.

Prof. Dr. Susamu Taketomi
Matsumoto Yushi-Seiyaku Co. Ltd., Shibukawa-Cho, Yao City, Osaka 581-0075, Japan.
staketomi@hotmail.com

Prof. Dr. Wolfgang Nolting
Institute of Physics / Chair: Solid State Theory, Humboldt-University at Berlin, Newtonstr. 15 D-12489 Berlin, Germany
Wolfgang.nolting@physik.hu-berlin.de

The Hashemite Kingdom of Jordan

Yarmouk University

Jordan Journal of
PHYSICS

An International Peer-Reviewed Research Journal
Funded by the Scientific Research Support Fund

Volume 9, No. 2, 2016, 1438 H

Instructions to Authors

Instructions to authors concerning manuscript organization and format apply to hardcopy submission by mail, and also to electronic online submission via the Journal homepage website (http://jjp.yu.edu.jo).

Manuscript Submission

1- **E-mail to** : jjp@yu.edu.jo

2- **Online**: Follow the instructions at the journal homepage website.

Original *Research Articles*, *Communications* and *Technical Notes* are subject to critical review by minimum of two competent referees. Authors are encouraged to suggest names of competent reviewers. *Feature Articles* in active Physics research fields, in which the author's own contribution and its relationship to other work in the field constitute the main body of the article, appear as a result of an invitation from the Editorial Board, and will be so designated. The author of a *Feature Article* will be asked to provide a clear, concise and critical status report of the field as an introduction to the article. *Review Articles* on active and rapidly changing Physics research fields will also be published. Authors of *Review Articles* are encouraged to submit two-page proposals to the Editor-in-Chief for approval. Manuscripts submitted in *Arabic* should be accompanied by an Abstract and Keywords in English.

Organization of the Manuscript

Manuscripts should be typed double spaced on one side of A4 sheets (21.6 x 27.9 cm) with 3.71 cm margins, using Microsoft Word 2000 or a later version thereof. The author should adhere to the following order of presentation: Article Title, Author(s), Full Address and E-mail, Abstract, PACS and Keywords, Main Text, Acknowledgment. Only the first letters of words in the Title, Headings and Subheadings are capitalized. Headings should be in **bold** while subheadings in *italic* fonts.

Title Page: Includes the title of the article, authors' first names, middle initials and surnames and affiliations. The affiliation should comprise the department, institution (university or company), city, zip code and state and should be typed as a footnote to the author's name. The name and complete mailing address, telephone and fax numbers, and e-mail address of the author responsible for correspondence (designated with an asterisk) should also be included for official use. The title should be carefully, concisely and clearly constructed to highlight the emphasis and content of the manuscript, which is very important for information retrieval.

Abstract: A one paragraph abstract not exceeding 200 words is required, which should be arranged to highlight the purpose, methods used, results and major findings**.**

Keywords: A list of 4-6 keywords, which expresses the precise content of the manuscript for indexing purposes, should follow the abstract.

PACS: Authors should supply one or more relevant PACS-2006 classification codes, (available at http://www.aip.org/pacs/pacs06/pacs06-toc.html)

Introduction: Should present the purpose of the submitted work and its relationship to earlier work in the field, but it should not be an extensive review of the literature (e.g., should not exceed 1 ½ typed pages).

Experimental Methods: Should be sufficiently informative to allow competent reproduction of the experimental procedures presented; yet concise enough not to be repetitive of earlier published procedures.

Results: should present the results clearly and concisely.

Discussion: Should be concise and focus on the interpretation of the results.

Conclusion: Should be a brief account of the major findings of the study not exceeding one typed page.

Acknowledgments: Including those for grant and financial support if any, should be typed in one paragraph directly preceding the References.

References: References should be typed double spaced and numbered sequentially in the order in which they are cited in the text. References should be cited in the text by the appropriate Arabic numerals, enclosed in square brackets. Titles of journals are abbreviated according to list of scientific periodicals. The style and punctuation should conform to the following examples:

1. Journal Article:

a) Heisenberg, W., Z. Phys. 49 (1928) 619.

b) Bednorz, J. G. and Müller, K. A., Z. Phys. B64 (1986) 189

c) Bardeen, J., Cooper, L.N. and Schrieffer, J. R., Phys. Rev. 106 (1957) 162.

d) Asad, J. H., Hijjawi, R. S., Sakaji, A. and Khalifeh, J. M., Int. J. Theor. Phys. 44(4) (2005), 3977.

2. Books with Authors, but no Editors:

a) Kittel, C., "Introduction to Solid State Physics", 8th Ed. (John Wiley and Sons, New York, 2005), chapter 16.

b) Chikazumi, S., C. D. Graham, JR, "Physics of Ferromagnetism", 2nd Ed. (Oxford University Press, Oxford, 1997).

3. Books with Authors and Editors:

a) Allen, P. B. "Dynamical Properties of Solids", Ed. (1), G. K. Horton and A. A. Maradudin (North-Holland, Amsterdam, 1980), p137.

b) Chantrell, R. W. and O'Grady, K., "Magnetic Properities of Fine Particles" Eds. J. L. Dormann and D. Fiorani (North-Holland, Amsterdam, 1992), p103.

4. Technical Report:

Purcell, J. "The Superconducting Magnet System for the 12-Foot Bubble Chamber", report ANL/HEP6813, Argonne Natt. Lab., Argonne, III, (1968).

5. Patent:

Bigham, C. B., Schneider, H. R., US patent 3 925 676 (1975).

6. Thesis:

Mahmood, S. H., Ph.D. Thesis, Michigan State University, (1986), USA (Unpublished).

7. Conference or Symposium Proceedings:

Blandin, A. and Lederer, P. Proc. Intern. Conf. on Magnetism, Nottingham (1964), P.71.

8. Internet Source:

Should include authors' names (if any), title, internet website, URL, and date of access.

9. Prepublication online articles (already accepted for publication):

Should include authors' names (if any), title of digital database, database website, URL, and date of access.

For other types of referenced works, provide sufficient information to enable readers to access them.

Tables: Tables should be numbered with Arabic numerals and referred to by number in the Text (e.g., Table 1). Each table should be typed on a separate page with the legend above the table, while explanatory footnotes, which are indicated by superscript lowercase letters, should be typed below the table.

Illustrations: Figures, drawings, diagrams, charts and photographs are to be numbered in a consecutive series of Arabic numerals in the order in which they are cited in the text. Computer-generated illustrations and good-quality digital photographic prints are accepted. They should be black and white originals (not photocopies) provided on separate pages and identified with their corresponding numbers. Actual size graphics should be provided, which need no further manipulation, with lettering (Arial or Helvetica) not smaller than 8 points, lines no thinner than 0.5 point, and each of uniform density. All colors should be removed from graphics except for those graphics to be considered for publication in color. If graphics are to be submitted digitally, they should conform to the following minimum resolution requirements: 1200 dpi for black and white line art, 600 dpi for grayscale art, and 300 dpi for color art. All graphic files must be saved as TIFF images, and all illustrations must be submitted in the actual size at which they should appear in the journal. Note that good quality hardcopy original illustrations are required for both online and mail submissions of manuscripts.

Text Footnotes: The use of text footnotes is to be avoided. When their use is absolutely necessary, they should be typed at the bottom of the page to which they refer, and should be cited in the text by a superscript asterisk or multiples thereof. Place a line above the footnote, so that it is set off from the text.

Supplementary Material: Authors are encouraged to provide all supplementary materials that may facilitate the review process, including any detailed mathematical derivations that may not appear in whole in the manuscript.

Revised Manuscript and Computer Disks

Following the acceptance of a manuscript for publication and the incorporation of all required revisions, authors should submit an original and one more copy of the final disk containing the complete manuscript typed double spaced in Microsoft Word for Windows 2000 or a later version thereof. All graphic files must be saved as PDF, JPG, or TIFF images.

Allen, P.B., "…………….", in: Horton, G.K., and Muradudin, A. A., (eds.), "Dynamical…….", (North……..), pp….

Reprints

Twenty (20) reprints free of charge are provided to the corresponding author. For orders of more reprints, a reprint order form and prices will be sent with the article proofs, which should be returned directly to the Editor for processing.

Copyright

Submission is an admission by the authors that the manuscript has neither been previously published nor is being considered for publication elsewhere. A statement transferring copyright from the authors to Yarmouk University is required before the manuscript can be accepted for publication. The necessary form for such transfer is supplied by the Editor-in-Chief. Reproduction of any part of the contents of a published work is forbidden without a written permission by the Editor-in-Chief.

Disclaimer

Opinions expressed in this Journal are those of the authors and neither necessarily reflects the opinions of the Editorial Board or the University, nor the policy of the Higher Scientific Research Committee or the Ministry of Higher Education and Scientific Research. The publisher shoulders no responsibility or liability whatsoever for the use or misuse of the information published by JJP.

Indexing

JJP is currently applying for indexing and abstracting to all related International Services.

Jordan Journal of

PHYSICS

An International Peer-Reviewed Research Journal

Volume 9, No. 2, 2016, 1438 H

Table of Contents:

English Articles	Pages
Crystallization Behavior of $Se_{85}Cd_8Zn_7$ Chalcogenide Glass Omar A. Lafi	71-79
Radon Concentration and Lung Cancer Risk in Bashika District Ahmed Khalef, Hana Ihsan Hasan and Yasir Yahya Kasim	81-85
Variational Calculations of the Exchange Energy of a Two-Electron Quantum Dot in a Magnetic Field A. Shaer, M.K. ELSAID and M. Elhasan	87-93
The Change in the Properties of ^{130}Xe - ^{130}Nd Isobar States Imad Mamdouh Ahmed	95-102
Robust High Resolution Fat-Water Separation in the Abdomen during Free-Breathing by Self-Gated 2D Radial TrueFISP Imaging Riad S. Ababneh, Thomas Benkert and Felix A. Breuer	103-108
Evaluation of Annual Effective Dose Due to Ingestion in Some Commonly Consumed Vegetables in Lagos State, Nigeria M. A. Olaoye, T. J. Aluko, J. A. RABIU, O. A. Jegede and O. O. Adeleke	109-112
Effects of Thermal Annealing on Structural and Optical Properties of Nanocrystalline $Cd_xPb_{1-x}S$ Thin Films Prepared by CBD S. M. Ahmad, S. J. Kasim and L. A. Latif	113-122
Applying Titius-Bode's Law on Exoplanetary Systems M. B. Altaie, Z. Yousef and A. I. Al-Sharif	123-130

Volume 9, Number 2, 2016. pp. 71-79

Jordan Journal of Physics

ARTICLE

Crystallization Behavior of $Se_{85}Cd_8Zn_7$ Chalcogenide Glass

Omar A. Lafi

Department of Physics, Faculty of Science, Al-Balqa Applied University, Al-Salt-19117, Jordan.

Received on: 12/4/2016; Accepted on: 16/8/2016

Abstract: Ternary $Se_{85}Cd_8Zn_7$ chalcogenide glass was prepared by melt quenching technique. Experimental measurements by differential scanning calorimeter (DSC) are used for studying crystallization behavior of this glass under non-isothermal conditions. DSC curves show well defined endothermic and exothermic peaks at glass transition (T_g) and crystallization peak (T_c) temperatures. The T_c dependence on the heating rate (β) is utilized in the determination of the crystallization activation energy (E_c) and the Avrami exponent (n). These crystallization parameters were deduced using Kissinger, Takhor, Augis-Bennett and Ozawa-Matusita methods. The theoretical derivations of these methods were discussed in this work. The resulting values of E_c obtained from the different methods agree good with each other and the obtained value of Avrami exponent ($n = 0.87$) indicated that the crystal growth in $Se_{85}Cd_8Zn_7$ glass occurs in one dimension.

Keywords: Chalcogenide glasses; Differential scanning calorimeter (DSC); Crystallization activation energy; Dimensionality of crystal growth.

Introduction

Over the past few decades, the unique properties of chalcogenide glasses (including selenium, tellurium, sulfur and their compounds) have encouraged researchers to understand the important processes proceeding in these materials for further development and search for new application possibilities. Crystallization (the process when glass in a metastable state is heated high enough for its structure to be able to "de-freeze" and transform into a more thermodynamically stable crystalline state) is one of the important processes in the field of chalcogenide glass. The most promising properties of chalcogenide glass, in its amorphous state, have been found to deteriorate drastically during crystallization. Therefore, studying and then understanding the crystallization mechanism to impede or control crystallization is a prerequisite for most of the applications, as stability against crystallization determines effective working limits [1]. Several attempts [2-8] are still made nowadays to investigate the crystallization kinetics of binary or multi-component chalcogenide systems.

Studying the crystallization kinetics can be carried out by two basic methods: isothermal and non-isothermal. In the isothermal method, the sample is brought quickly to a fixed temperature above the glass transition temperature (T_g) and the heat evolved during the crystallization process at this constant temperature is recorded as a function of time. In the non-isothermal method, the sample is heated at a fixed rate (β) and the heat evolved is recorded as a function of temperature. Non-isothermal measurements using a constant heating rate are more commonly used because of their several advantages, such as the quick performance and the rapid information they provide on the transformation temperatures, like glass transition temperature (T_g) and crystallization temperature (T_c) [9]. Differential scanning caliometry (DSC) is an extremely popular method for studying non-isothermal transformation kinetics. The appeal of this

Corresponding Author: Omar A. Lafi **Email**: olafi66@yahoo.com, olafi66@bau.edu.jo

method is simplicity and flexibility in the selection of heating (cooling) rates. Crystallization kinetics (under non-isothermal conditions) can always be analyzed by the determination of crystallization activation energy (E_c) and the dimensionality of crystal growth (m).

Zinc selenide (ZnSe) has unique physical properties, such as wide optical energy band gap, high refractive index and low optical absorption in the visible and infrared spectral regions. Therefore, it has several potential applications, such as blue light emitting diodes, photodiodes, thin film transistors and Cr-doped ZnSe laser [10]. On the other hand, cadmium selenide (CdSe) is widely preferred in fabrication of solar cells, photodetectors, light emitting diodes and other opto-electronic devices owing to its high photosensitive behavior [11]. According to the author's knowledge, no work has been conducted to study crystallization behavior of Se-based ternary chalcogenide glasses containing both Cd and Zn as dopant materials. Therefore, this work aims to investigate, using differential scanning calorimeter, the crystallization kinetics of the ternary $Se_{85}Cd_8Zn_7$ chalcogenide glass under non-isothermal conditions. The dependence of the crystallization peak temperature (T_c) on heating rate (β) will be used for the calculation of the crystallization activation energy of $Se_{85}Cd_8Zn_7$ glass, using different theoretical methods which will be discussed in this work. This further will be used for determining the dimensionality of crystal growth.

Theoretical Basis

The general Johnson-Mehl-Avrami (JMA) equation for solid state transformation can be used to describe the kinetics of crystallization for many amorphous materials [12]. This equation is based upon the following assumptions [13]: (1) the system is in a quasi-equilibrium state and the rate at which the atoms leave the initial state is so small that the energy distribution of the initial state is undisturbed, (2) the rate is not diffusion limited and (3) the crystallization mechanism is of a nucleation and growth type, (4) nucleation is spatially random and (5) the process takes place under isothermal conditions. JMA equation describes the time evolution of the overall crystallinity. According to these assumptions, the fraction X of the material that crystallized after a time t can be written as [14-17]:

$$X = 1 - \exp[-(Kt)^n]; \qquad (1)$$

where n is the Avrami exponent that reflects the details of crystal growth. K is the effective overall reaction rate (including both nucleation and growth), which is actually a measure of the rate of crystallization and usually assigned Arrhenius temperature dependence:

$$K = K_0 \exp(-\frac{E_c}{RT}) . \qquad (2)$$

Here, K_0, a frequency factor, indicates the number of attempts to overcome the energy barrier and E_c is the activation energy for crystallization. Based on JMA equation, different authors [18-23] have developed different methods to study the crystallization process by calculating the crystallization activation energy E_c and the order of crystallization n.

Kissinger Method

This method is most widely used in analyzing crystallization data obtained from DSC measurements. In non-isothermal DSC experiments, at a constant heating rate β (= dT/dt), the sample temperature T changes linearly with time according to the relation:

$$T = T_i + \beta t ; \qquad (3)$$

where T_i is the temperature at the beginning of the experiment which is usually equal to room temperature.

The derivative of K with respect to time can be obtained from Eqs. (2) and (3) as follows:

$$\frac{dK}{dt} = \left(\frac{dK}{dT}\right)\left(\frac{dT}{dt}\right) = \left(\frac{\beta E_c}{RT^2}\right)K . \qquad (4)$$

Eq. (1) can be differentiated as:

$$\frac{dX}{dt} = n(Kt)^{n-1}[K + (dK/dt)t](1 - X) . \qquad (5)$$

Substituting Eq. (4) in Eq. (5), we get:

$$\frac{dX}{dt} = nK^n t^{n-1}[1 + \alpha t](1 - X) ; \qquad (6)$$

where $\alpha = (\beta E_c / RT^2)$.

According to Kissinger [18], the term αt can be neglected in comparison to unity ($(E_c / RT^2) << 1$), and then Eq. (6) becomes:

$$\frac{dX}{dt} = (1-X)nK^n t^{n-1} \quad . \tag{7}$$

If we express t in terms of X from Eq. (1), the crystallization rate dX/dt can be written as:

$$\frac{dX}{dt} = AnK\,(1-X) \ ; \tag{8}$$

where $A = [-\ln(1-X)]^{(n-1)/n}$.

Using Eqs. (4) and (8), the second derivative $d^2X/dt^2 = 0$ at the crystallization peak temperature T_c, then Kissinger showed that [18]:

$$\ln\left(\frac{\beta}{T_c^2}\right) = -\frac{E_c}{RT_c} + C \quad . \tag{9}$$

This equation is used to calculate the activation energy of crystallization by plotting $\ln(\beta/T_c^2)$ *versus* $1/T_c$.

Takhor Method

Takhor [22] suggested a method which makes the assumption of ignoring the time dependence of K in the second differentiation. Assuming that $K \neq K(t)$, the differentiation of Eq. (7) with respect to time yields:

$$\frac{d^2X}{dt^2} = nK^n t^{n-2}[(n-1) - nK^n t^n] \ . \tag{10}$$

The maximum rate of crystallization occurs at peak crystallization temperature T_c and time t_p, where $d^2X/dt^2 = 0$, and if we convert the value of t_p to temperature T_c from Eq. (3), we get [24]:

$$n\ln\beta - n\ln(T_c - T_i) = \ln\frac{nK_0}{n-1} - \frac{nE_c}{RT_c} \ . \tag{11}$$

With the assumption that $n\ln(T_c - T_i)$ is a function which changes more slowly with heating rate than $1/T_c$, we get:

$$\frac{d\ln\beta}{d(1/T_c)} = -\frac{E_c}{R} \ . \tag{12}$$

On this basis, the slope of $\ln\beta$ *versus* $1/T_c$ should yield the crystallization activation energy E_c.

Augis-Bennett Method

The standard method of Augis and Bennet gives more exact results for deducing the crystallization parameters when the crystallization appears at a temperature much higher than the initial one ($T_c >> T_i$). Based on substituting $u = KT$ in Eq. (6), we get:

$$\frac{dX}{dt} = X' = nKu^{n-1}[1+\alpha t](1-X) \ . \tag{13}$$

Since $u' = K'T + K$ and using Eq. (4), one obtains:

$$X' = nu'u^{n-1}(1-X) \tag{14}$$

and

$$X'' = [u''u - (u')^2(nu^n - n + 1)]nu^{n-2}(1-X) \ . \tag{15}$$

$X'' = d^2X/dt^2 = 0$ at crystallization peak temperature T_c, where the maximum rate of crystallization occurs. This gives:

$$u''u - (u')^2(nu^n - n + 1) = 0 \ . \tag{16}$$

From substituting $u = KT$ and $T = T_i + \beta t$ in JMA equation, one can find that:

$$u' = \frac{u}{t} + \alpha u = u\left(\frac{1}{t} + \alpha\right) \ ; \tag{17}$$

$$\left.\begin{aligned} u'' &= u'\left(\frac{1}{t}+\alpha\right) - \frac{u}{t^2} \\ &= u\left[\left(\frac{1}{t}+\alpha\right)^2 - \frac{1}{t^2}\right] - \frac{2\alpha u}{t} \end{aligned}\right\} \ . \tag{18}$$

The last term in Eq. (18) above was omitted in the original derivation of Augis and Bennet [21], and this equation can be simplified as:

$$u'' = u\alpha^2 \ . \tag{19}$$

Substituting for u' and u'' from Eqs. (17) and (19) into Eq. (16) gives:

$$nu^n - n + 1 = \left(\frac{\alpha t}{1+\alpha t}\right)^2 \ . \tag{20}$$

Eq. (20) is discussed in light of the possible values of αt and the relation between the temperatures T and T_i. The term αt can be expressed by substituting the value of $\beta = \alpha RT^2/E_c$ in Eq. (3) as [25]:

$$\alpha t = \frac{E_c}{RT}\left(1 - \frac{T_i}{T}\right) \ . \tag{21}$$

When $\alpha t \ll 1$ and the temperature T is slightly higher than T_i ($(E_c / RT) \ll 1$), we can neglect the term αt and Eq. (20) leads directly to Kissinger equation. Besides, when $\alpha t \gg 1$ and $T \gg T_i$, then $(E_c / RT) \gg 1$, the right hand side of Eq. (20) approaches unity and this gives $u^n = 1$ and hence $u = 1$. Therefore, we can write:

$$u = (Kt)_p = K_0 \exp\left(\frac{E_c}{RT_c}\right)\left[\frac{T_c - T_i}{\beta}\right] \cong 1. \tag{22}$$

This equation can be written in logarithmic form as:

$$\ln\left(\frac{\beta}{T_c - T_i}\right) = -\frac{E_c}{RT_c} + \ln K_0 \ . \tag{23}$$

Finally, in the case of ($T_c \gg T_i$), this equation can be approximated as:

$$\ln\left(\frac{\beta}{T_c}\right) = -\frac{E_c}{RT_c} + \ln K_0 . \tag{24}$$

The activation energy E_c can be evaluated from the slope of the plot of ln (β / T_c) as a function of $1/T_c$.

Determination of Avrami Exponent (n)

Avrami exponent (n) can be simply found from the original JMA equation. Substituting the value of t from Eq. (3) in the JMA equation (Eq. (1)) and rearranging we get:

$$1 - X = \exp\left[-\left(\frac{K\,(T - T_i)}{\beta}\right)^n\right]. \tag{25}$$

By taking the double logarithm of the above equation, one can find that:

$$\frac{d \ln[-\ln(1-X)]}{d \ln \beta} = -n . \tag{26}$$

This relation was derived individually by Ozawa [19, 20] and Matusita *et al.* [21]. According to this relation, Avrami exponent (n) can be evaluated by plotting $\ln[-\ln(1-X)]$ as a function of $\ln\beta$ at a constant temperature T. The fraction X crystallized at any temperature T is given as $X = A_T/A$, where A is the total area of the exothermic peak between the temperature T_1 where crystallization just begins and the temperature T_2 where crystallization is completed and A_T is the area between T_1 and a given temperature T as shown in Fig. 1. For as-quenched glass containing no preexisting nuclei, the dimensionality of crystal growth (m) is equal to ($n - 1$) and m will be 1 if n is less than 2, whereas for a glass containing a sufficiently large number of nuclei, which might occur due to annealing of the as-quenched glass, $m = n$. In this work, as-quenched samples are studied, then the value of m is taken as $m = n - 1$ [23].

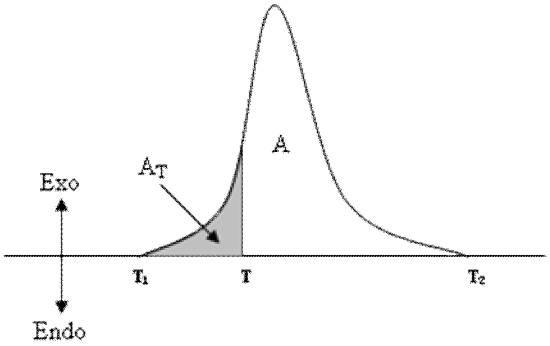

FIG. 1. A typical DSC exothermic peak indicating the estimation of the fraction X crystallized at any temperature T.

Material Preparation and Experimental Technique

$Se_{85}Cd_8Zn_7$ glass was prepared by melt quenching technique. High purity (5N) Se, Cd and Zn in appropriate atomic weight percentage (at. wt %) proportions were weighed into a quartz ampoule and sealed at a vacuum of 10^{-5} Torr. The ampoules were then heated at 900 ◦C for about 15 h with continuous rotation to facilitate the homogenization of the sample. The molten sample was rapidly quenched in ice-cooled water to produce a glassy state. The ingot of the so-produced glassy sample was taken out of the ampoule by breaking the ampoule and then grinding the sample gently in a mortar and pestle to obtain a powder form. About 10 mg of the powder samples were capsulated in aluminum pan and subjected to the differential scanning calorimeter (NETZSCH DSC 200 *F3*) at five heating rates (5, 10, 15, 20 and 25 K/min) in the temperature range from room temperature to about 750K. The temperature accuracy of this equipment is ± 0.1K. The DSC equipment is calibrated prior to measurements, using high purity standard Pb, Sn and In with well-known melting points. The operation of a differential scanning calorimeter is based on the measurement of the thermal response of an unknown specimen as compared with a standard when the two are uniformly heated. A typical differential scanning calorimeter consists of two sealed pans; a sample pan and an empty reference pan. These pans are often covered by or composed of aluminum, which acts as a radiation shield. The two pans are uniformly heated, or cooled, while the heat flow difference between the two is monitored.

Results and Discussion

Typical DSC curves of $Se_{85}Cd_8Zn_7$ glass at five different heating rates (5, 10, 15, 20 and 25 K/min) are shown in Fig.2. Two characteristic phenomena are evident in these DSC curves in the temperature range of investigation. The first one (endothermic peak) corresponds to the glass transition region and is represented by the glass transition temperature (T_g). The second one (exothermic peak) corresponds to the crystallization region and is represented by the crystallization peak temperature (T_c). At this temperature (T_c), the crystallization rate reaches two-thirds of its value [4]. The appearance of single glass transition peak and single crystallization peak confirms that the glassy sample under investigation is homogeneous. Both T_g and T_c have been defined [1, 9] as the temperatures which correspond to the intersection of two linear portions adjoining the transition elbow of the DSC traces in the endothermic and exothermic directions, respectively. The values of T_g and T_c at all heating rates are given in Table 1. From this table, one can notice that both T_c and T_g of the studied samples are much higher than room temperature. Thus, one can expect that the studied sample may remain stable in its amorphous and crystalline phases at room temperature. In addition, the temperature difference ($T_c - T_g$) is large. This is an advantage of the studied glass, as it is essential to prevent self-transition between the two amorphous and crystalline phases, making it attractive for optical recording applications [26].

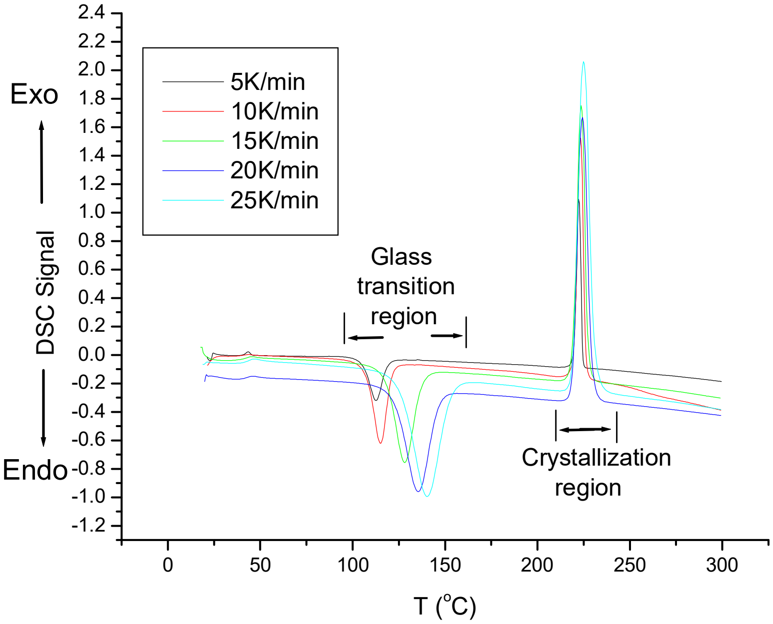

FIG. 2. Typical DSC curves for $Se_{85}Cd_8Zn_7$ glass at five different heating rates (5, 10, 15, 20 and 25 K/min).

TABLE. 1. The values of T_g and T_c of the studied glass at different heating rates

Heating rate (K/min)	T_g (K)	T_c (K)
5	377.2	495.0
10	385.7	496.2
15	390.1	496.9
20	394.0	497.4
25	396.5	497.9

The crystallization kinetics of the studied glass were analyzed by calculating the crystallization activation energy (E_c) and Avrami exponent (n) which is related to the dimensionality of crystal growth (m). These parameters were calculated from the dependence of the crystallization peak temperature (T_c) on heating rate (β) according to the theoretical methods discussed in Section 2. Firstly, according to Eq. (9), which was derived by Kissinger, the data of $\ln(\beta/T_c^2)$ *versus* $(10^3/T_c)$ for $Se_{85}Cd_8Zn_7$ glass is fitted to linear function by least square fitting as shown in Fig. 3. From the slope of this fit, the value of the activation energy (E_c) is obtained to be (1143 ± 24) kJ/mol. Secondly, E_c was determined using Takhor method according to Eq. (12). In this method, the activation energy is evaluated from the slope of the least square fitting of the plot of $\ln\beta$ *versus* $(10^3/T_c)$ which is shown in Fig. 4. The value of E_c deduced by this method is (1151 ± 24) kJ/mol. Finally, E_c was calculated using Augis and Bennett approximation method as given in Eq. (24). Fig. 5 shows the plot of $\ln(\beta/T_c)$ against $(10^3/T_c)$ and from the slope of the straight line of the least square fitting of all points, the value of E_c is obtained to be (1147 ± 24) kJ/mol.

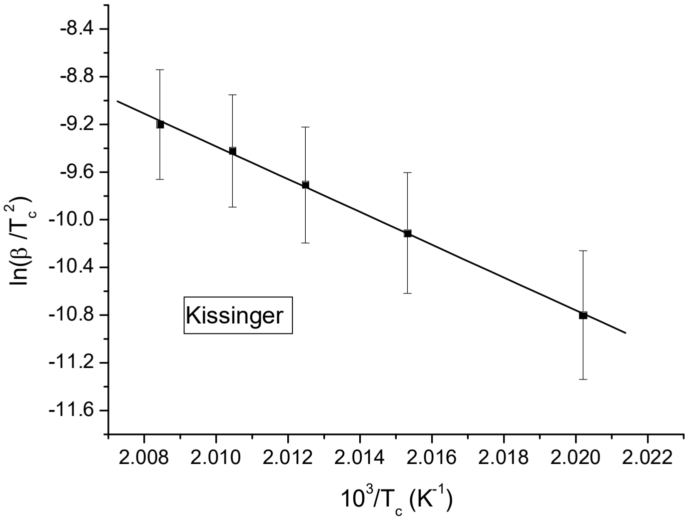

FIG. 3. Plot of $\ln(\beta/T_c^2)$ *vs.* $(10^3/T_c)$ for $Se_{85}Cd_8Zn_7$ glass (solid line is least-square fit to Kissinger relation (Eq. 9)).

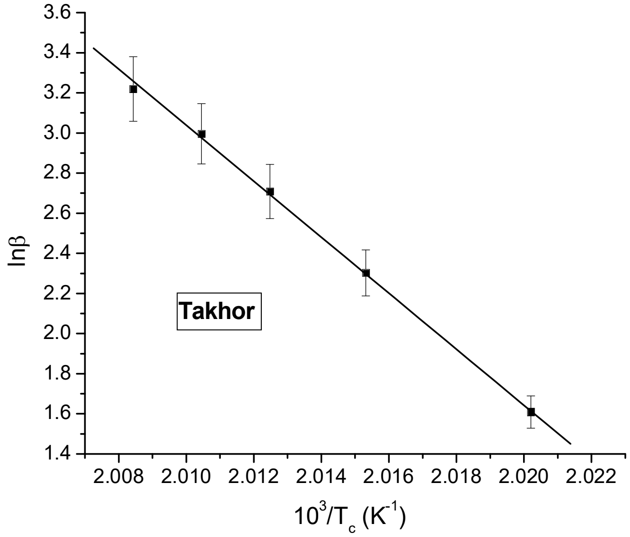

FIG. 4. Plot of $\ln\beta$ *vs.* $(10^3/T_c)$ for $Se_{85}Cd_8Zn_7$ glass (solid line is least-square fit to Takhor relation (Eq. 12)).

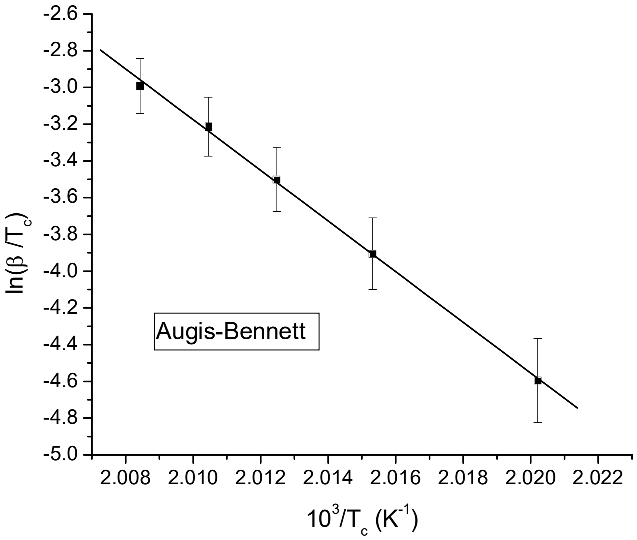

FIG. 5. Plot of $\ln(\beta / T_c)$ *vs.* $(10^3 / T_c)$ for $Se_{85}Cd_8Zn_7$ glass (solid line is least-square fit to Augis and Bennett approximation relation (Eq. 24)).

The above E_c values, obtained from the three methods, are well consistent with each other. However, Augis and Bennet method gives more exact results for deducing E_c value when the crystallization appears often at a temperature which is much higher than the initial one $T_c >> T_i$. It was shown [27] that this method can be applied, not only in the case $T_c >> T_i$, but also when $T_c > T_i$; that is, when the two temperatures differ by about 10%. Besides, the crystallization activation energy is an indication of the speed of rate of crystallization which is useful to characterize the glass for optical recording and other applications [28]. It is clear that the value of E_c of $Se_{85}Cd_8Zn_7$ glass, which is required to complete the crystallization process, is higher than that of similar glasses. This could be explained on the basis of bond formation in the complex matrices.

According to Schotmiller et al. [29], in amorphous Se, about 40% of the atoms have a ring structure (Se_8) and 60% of the atoms are bonded as polymeric chains (–Se–Se–Se–). Strong covalent bonds exist between the atoms in the chains and rings, whereas the inter-structural forces are weak bonds of Van der Waal's type [30]. When Zn is incorporated to Se, the metallic Zn bonds dissolved in Se chains and the weaker Se–Se bonds (bond energy = 44.0 kcal/mole) are replaced by the strong Se–Zn bonds (bond energy = 64.0 kcal/mole) [31]. In addition to Se–Zn heteronuclear bonds, Zn–Zn and Se–Se homonuclear bonds are expected to exist. Further, when Cd is added to the Se-Zn system, it forms bonds with Se (Se-Cd bond energy = 37.1 kcal/mole [9]), while the formation of Zn–Cd, Cd–Cd and Se–Zn–Cd can also exist in the same matrix. The extensive existence of heteronuclear and homonuclear bonds heavily cross-linked the ternary matrix structure and increased the steric hindrance, which play a dominant role in the glass configuration [32]. On the other hand, Pauling defined the electronegativity of an atom as its power to attract electrons to itself in the molecule [33]. When two elements of different electronegativity values combine to form an alloy, then the element of higher electronegativity attracts an electron pair more than the other elements and behaves as an anion. The other element will behave as a cation [34]. The values of electronegativity of Se, Cd and Zn are 2.4, 1.7, and 1.6, respectively. Therefore, Se behaves as an anion, while both of Zn and Cd (from the same IIB group) are considered as cations. The presence of Zn and Cd cations together can create a large number of unsaturated hydrogen - like bonds accompanied with Van der Waal's bonds, substantially increasing the structural and thermal stability of the glass [35]. This is responsible for increasing the strength or rigidity of the lattice, which increases the tendency of the glass against crystallization and consequently the crystallization activation energy.

The order of crystallization reaction (Avrami exponent) for $Se_{85}Cd_8Zn_7$ glass was obtained using the method suggested by Ozawa and

Matusita. The plot of $\ln[-\ln(1-X)]$ *vs.* $\ln\beta$ for $Se_{85}Cd_8Zn_7$ glass is shown in Fig. 6 at different temperatures (494K, 495K, 496K and 497K). The average value of Avrami exponent *n*, obtained from the slopes of the fitted straight lines in Fig.6, comes out to be 0.87. Based on this value, the crystal growth in $Se_{85}Cd_8Zn_7$ glass occurs in one dimension (or growth from surface nuclei). This value of Avrami exponent is non-integer. A non-integer value of *n* indicates that two crystallization mechanisms were working during the amorphous–crystalline transformation [26, 36]. Lastly, it is worth to mention that some other thermal models [37-40] used in the study of the non-isothermal crystallization mechanism suggested that the values of *n* and E_c are not necessarily constant, but show variations in different stages of the transformation. The models used in this work are proposed for analyzing the non-isothermal crystallization kinetics, in the case of as-quenched glasses which contain a large number of nuclei, "site saturation". This "site saturation" assumption is important for this process, where the crystallization rate is only defined by the temperature and shows little dependence on the thermal history, and then the variation in the values of the crystallization parameters (*n* and E_c) during all stages of transformation process is not expected [41].

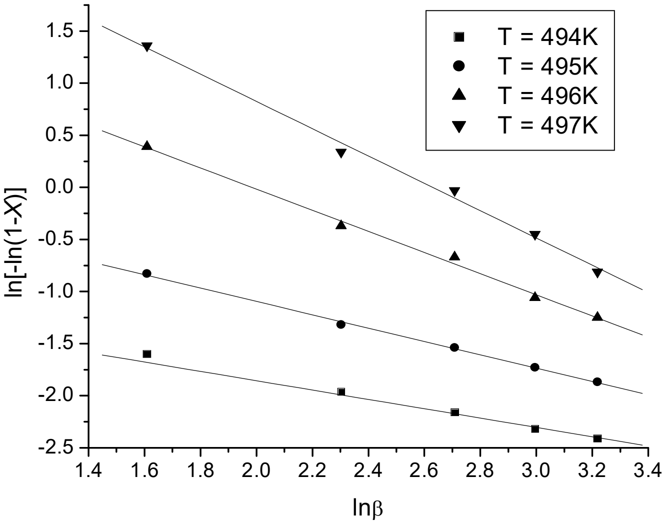

FIG. 6. Plot of $\ln[-\ln(1-X)]$ *vs.* $\ln\beta$ for $Se_{85}Cd_8Zn_7$ glass at different selected temperatures (solid lines are least-square fits to Ozawa-Matusita relation (Eq. 26)).

Conclusions

Crystallization kinetics for $Se_{85}Cd_8Zn_7$ glass have been investigated using differential scanning calorimeter DSC under non-isothermal conditions. The obtained data has been analyzed by several theoretical methods. The following conclusions were drawn:

1. The glassy alloy under investigation shows single glass transition region and single crystallization region, confirming the homogeneity of the glassy sample.
2. The values of E_c obtained using the three different methods; Kissinger, Takhor and Augis-Bennett, are in good agreement with each other. Thus, one can use any of these methods to deduce the activation energy of crystallization.
3. One-dimensional crystal growth occurs in $Se_{85}Cd_8Zn_7$ glass, indicated by the estimated value of Avrami exponent ($n = 0.87$).

Acknowledgment

This work has been carried out during sabbatical leave granted to the author (O.A. Lafi) from Al-Balqa Applied University during the academic year 2015/2016; therefore, it deserved great thanks. The author is also grateful to the Department of Physics at the University of Jordan for providing all facilities during this research work.

References

[1] Imran, M.M.A., Bhandari, D. and Saxena, N.S., J. Therm. Anal. Calorim., 65 (2001) 257.

[2] Lafi, O.A., Imran, M.M.A., Abu-Shaweesh, N.I., Al-Kurdi, F.M. and Khatatbeh, I.K., J. Phys. Chem. Solids, 75 (2014) 790.

[3] Lafi, O.A., Imran, M.M.A, Abdullah, M.K. and Al-Sakhel, S.A., Thermochimica Acta, 560 (2013) 71.

[4] Imran, M.M.A., Physica B, 406 (2011) 482.

[5] Tanwar, N. and Saraswat, V.K., J. Non-Cryst. Solids, 394 (2014) 1.

[6] Xu, W., Ren, J. and Guorong, C., J. Non-Cryst. Solids, 398-399 (2014) 42.

[7] Svoboda, R. and Málek, J., J. Alloys Comp., 627 (2015) 287.

[8] Štrbac, G.R., Štrbac, D.D., Lukić-Petrović, S.R. and Šiljegović, M.V., J. Non-Cryst. Solids, 426 (2015) 92.

[9] Lafi, O.A., J. Alloys Comp., 519 (2012) 123.

[10] Abdel-Rahim, M.A., Hafiz, M.M., Elwhab, A. and Alwany, B., Optics and Laser Technology, 44 (2012) 1116.

[11] Kalita, KR.P., Sarma, B.K. and Das, H.L., Bull. Mater. Sci., 26(6) (2003) 613.

[12] Marseglia, E.A., J. Non-Cryst. Solids, 41 (1980) 31.

[13] White, K., Crane, R.N. and Snide, J.A., J. Non-Cryst. Solids, 103 (1988) 210.

[14] Johnson, W.A. and Mehl, K.F., Trans. Amer. Inst. Mining Met. Egrs., 135 (1981) 315.

[15] Avrami, M., J. Chem. Phys., 7 (1939) 1103.

[16] Avrami, M., J. Chem. Phys., 8 (1940) 212.

[17] Avrami, M., J. Chem. Phys., 9 (1941) 177.

[18] Kissinger, H.E., J. Res. Nat. Bur. Stand., 57(4) (1956) 217.

[19] Ozawa, T., Bul. Chem. Soc., Japan, 38 (1965) 1881.

[20] Ozawa, T., Polymer, 12 (1971) 150.

[21] Augis, J.E. and Bennet, J., J. Therm. Anal., 13 (1978) 283.

[22] Takhor, R.L., "Advance in Nucleation and Crystallization of Glasses", (American Ceramic Society, Columbus, 1972), p.253.

[23] Matusita, T., Komatsu, T. and Yokota, R., J. Mat. Science, 19 (1984) 291.

[24] Uinnon, H. and Uhlmann, D.R., J. Non-Cryst. Solids, 54 (1983) 253.

[25] Kozmidis- Petrović, A.F., Štrbac, G.R. and Štrbac, D.D., J. Non-Cryst. Solids, 353 (2007) 2014.

[26] Srivastava, S., Zulfequar, M., Agrahari, S.K. and Kumar, A., Physica B, 403 (2008) 3429.

[27] Kozmidis-Petrović, A.F., Lukić, S.R. and Štrbac, G.R., J. Non-Cryst. Solids, 356 (2010) 2151.

[28] Khan, S.A., Al-Hazmi, F.S., Faidah, A.S. and Al-Ghamdi, A.A., Curr. Appl. Phys., 9 (2009) 567.

[29] Schotmiller, J., Tabak, M., Lucovsky, G. and Ward, A., J. Non-Cryst. Solids, 4 (1970) 80.

[30] Thiruvikraman, P.K., Bull. Mater. Sci., 29(4) (2006) 371.

[31] Abdel-Rahim, M.A., Hafiz, M.M., Elwhab, A. and Alwany, B., Optics and Laser Technology, 47 (2013) 88.

[32] Singh, A.K., Optik, 124 (2012) 2187.

[33] Pauling, L., "The Nature of the Chemical Bond", 3rd Ed. (Cornell University Press, 1960).

[34] Shukla, R.K., Swarupt, S., Kumar, A. and Nigam, A.N., Semicond. Sci. Technol., 4 (1988) 681.

[35] Singh, A.K., J. Alloys Comp., 552 (2013) 166.

[36] Al-Heniti, S.H., J. Alloys Comp., 484 (2009) 177.

[37] Vyazovkin, S., New J. Chem., 24 (2000) 913.

[38] Vyazovkin, S., Thermochimica Acta, 355 (2000) 269.

[39] Abdel-Rahim, M.A., Hafiz, M.M. and Mahmoud, A.Z., Progress in Natural Science: Materials International, 25 (2015) 169.

[40] Abdelazim, N.M., Abdel-Latief, A.Y., Abu-Sehly, A.A. and Abdel-Rahim, M.A., J. Non-Cryst. Solids, 387 (2014) 79.

[41] Málek, J., Thermochimica Acta, 355 (2000) 239.

Volume 9, Number 2, 2016. pp. 81-85

Jordan Journal of Physics

ARTICLE

Radon Concentration and Lung Cancer Risk in Bashika District

Ahmed Khalef, **Hana Ihsan Hasan** and **Yasir Yahya Kasim**

Physics Department, College of Education for Pure Sciences, Mosul University, Iraq.

Received on: 15/10/2015; Accepted on: 23/10/2016

Abstract: In this work, the indoor radon concentration level and lung cancer risks have been measured in Bashika district, east of Mosul city-Iraq, during the summer season, by using time integrated passive radon dosimeters containing CR-39 plastic track detectors. These measurements were carried out in the sitting room of ten dwellings built by plaster for an exposure time of 60 days. The radon concentration in these dwellings ranges from (18.32-54.87) $Bq.m^{-3}$with an average of (33.44 $Bq.m^{-3}$), which lies below the acceptable radon levels (50-150) $Bq.m^{-3}$ recommended by the International Commission of Radiation Protection (ICRP). The average value of the PAEC was 3.61×10^{-3} in working level (WL) and the average value of potential alpha energy concentration (PAEC) in working level month per year (WLM/Y) was 0.14. The average absorption effective dose equivalent for a person living in homes for which the investigation was done was found to be ($0.79mSv.y^{-1}$). In the recent report (ICRP), the recommended action levels of radon in dwellings should be within the range of (3-10 mSv). It is observed that the average lung cancer cases per year per 10^6 persons were found to be 14.31.

Keywords: CR-39; Radon-222 concentration; AEDE; PAEC.

Introduction

The three isotopes of radon ^{219}Rn, ^{220}Rn and ^{222}Rn are radioactive gases with half- lives of 3.96s, 55.6s and 3.825d, respectively. These isotopes are produced by decay of the natural radio nuclides ^{235}U, ^{232}Th and ^{238}U. ^{222}Rn can be considered to be of the most dangerous radioactive elements in the environment, because of its short half-life. Its character as a noble gas allows it to spread through the atmosphere [1]. The main natural sources of indoor ^{222}Rn level are soil, building materials (sand, rocks, cement, … etc.), water born transport and natural energy sources like gas, coal, … etc, which contain traces of ^{238}U [1,2]. The indoor radon concentration depends mainly on radon exhalation from surrounding materials. ^{222}Rn and its airborne daughters can cause a significant internal health hazard (for example lung cancer), especially when uranium or radium content in the soil is high or when radon and its daughters are concentrated in enclosed areas and in particular in dwelling areas. Several reports have appeared in the literature, demonstrating that residential ^{222}Rn may be responsible for 7% of lung cancer in Germany, 4% in Netherlands, 20% in Sweden and (10-15) % in the United States [3].

Concentration of ^{222}Rn gas in dwelling areas has been reviewed and summarized by the United Scientific Committee on the Effects of Atomic Radiation (UNSCEAR) [4]. The data is available for over 20 European countries and shows that the average ^{222}Rn concentration varies widely from < 25 $Bq.m^{-3}$ in the Netherlands, the United Kingdom and Cyprus, to over 100 $Bq.m^{-3}$ in Estonia, Finland, Sweden, Luxembourg, the Czech Republic, Hungary and Albania. For many countries, the variation in indoor ^{222}Rn levels within the country is enormous, and individual dwellings with ^{222}Rn gas concentrations above 10000 Bq/m^3 have been found in Finland, Norway, Sweden,

Corresponding Author: Y. Y Kasim **Email**: yasr_physics@yahoo.com

Belgium, Germany, Switzerland, the United Kingdom, the Czech Republic and Spain [4, 5].

In a recent multi-year survey conducted on Guam by the local Environmental Protection Agency (EPA), indoor ^{222}Rn levels exceeded the U.S. EPA air quality standard of 148 Bq/m^{3}, m~40% of all buildings tested. By the mid 1990s, it was widely publicized that radon was the second leading cause of lung cancer after smoking. Shortly thereafter, the U.S. EPA estimated that indoor radon exposures account for approximately 21,000 lung cancer deaths annually in the U.S. This represents about 14% of all U.S. lung cancer deaths. The number of lung cancer cases reported for each village between 1993 and 2007 ranged from 5-159 and were tightly correlated with village population size (r = 0.95) [6].It can be concluded that lung cancer rate may show a negative correlation with natural radon concentration [7]. Measurement of indoor ^{222}Rn is rather important, because the radiation dose of humans constitutes more than 60% of the total equivalent dose of annual exposures of humans, including exposure from natural sources [6, 8]. Several techniques have been used to measure the concentration of ^{222}Rn and its daughters. Solid state nuclear track detectors, such as LR-115 and CR-39, have been widely used for the measurement of time integrated radon levels in dwellings under different conditions [9, 10].

The present study aims to measure some important parameters, such as the indoor ^{222}Rn concentration in dwellings of Bashika district, the potential alpha energy concentration, the absorption effective dose exposure and the lung cancer cases per year per 10^6 persons. These evaluations can help in establishing a reference level of activity concentration from which any further increase in those levels for any reason could be detected.

Experimental Procedure

This study assesses the indoor ^{222}Rn concentration in dwellings of Bashika district situated in the east of Mosul city in Iraq. The dwelling spaces under study were in general buildings with cement bricks, with a concrete and iron structure. The walls of the dwellings are often covered with gypsum board and several of these materials are expected to contribute significantly to sources of indoor ^{222}Rn.

The passive ^{222}Rn dosimeter (as in Fig. 1) is a closed chamber into which ^{222}Rn diffuses and is composed of a plastic cup of 7 cm in diameter and 4.6 cm in depth. A circular hole of sponge with an area of (2x2) cm^2 and a thickness of 0.5 cm is sealed to the interior surface of the lid. The design of the chamber ensures that aerosol particles and thoron (^{220}Rn) are deposited on the sponge from outside and ^{222}Rn, among other gases, diffuses through it to the sensitive volume of the chamber. The cup contains a CR-39 alpha track detector fixed to the bottom by double-side cello-tape.

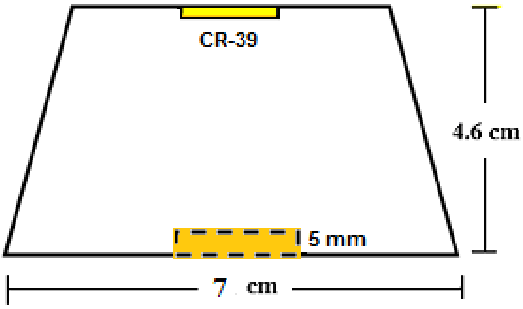

FIG. 1. Irradiation chamber

The measurements were carried out in the sitting room of the dwelling for an exposure time of 60 days during the summer season (August) of 2007. The detectors were collected and chemically etched using the aqueous solution of 6.25 N of NaOH at a temperature of 70 ^{o}C for 4 hours. After etching, the detectors were rinsed in distilled water and cleaned. An optical microscope with a magnification of X400 was used to count the number of tracks per cm^2 in each detector.

The calibration process for the dosimeter of this type and dimension was done by [3]. The concentration of ^{222}Rn (C_{Rn}) in units of Bq/m^3 was determined by measuring the track density (ρ) of the exposed detector inside the cup according to the following relation [11]:

$$\frac{c_o\, t_o}{\rho_o} = \frac{c_{Rn}\, t}{\rho} \; ; \qquad (1)$$

where c_0 is the concentration during the calibration process which equal to 90 kBq/m^3, ρ_o is the track density on the calibrated dosimeters which is equal to 96768 tracks/cm^2, t_o is the exposure time for calibrated dosimeters which is equal to 48 hours and t is the exposure time which is equal to 60 days.

Our aim is to find the following parameters:

1- (PAEC) in working level (WL) of radon daughters estimated according to the following equation [1, 3]:

$$C_a = \frac{F\,C_{Rn}}{3700}. \qquad (2)$$

First find the concentration of ^{222}Rn, so the equivalent equilibrium concentration *EEC* of radon is deduced as in the equation: $EEC = F \times C_{Rn}$.

F is the equilibrium factor which is equal to 0.4 indoor, *EEC* times 0.01 is the *PAEC* in (*WLM*), while $WLMY^1$ is equivalent to working level *WL* times factor 40.

2- The absorption effective dose equivalent (*AEDE*) is estimated by using the dose conversion factor of 5.5 mSv/*WLM* [1, 12].

$$\left. \begin{array}{l} AEDE\ (mSv\ /\ y) = \\ \quad (5.5\ mSv\ /WLM\ ) * (WLM\ /\ y) \end{array} \right\} \qquad (3)$$

3- Lung cancer cases per year per 10^6 persons are estimated by using the risk factor lung cancer induction of 18×10^{-6} mSv^{-1} [1, 12].

$$\left. \begin{array}{l} \text{Lung cancer cases per year per } 10^6 \text{ persons} \\ = AEDE\,(mSv\ /\ y\,) * 18 * 10^{-6}\ (mSv^{-1}) \end{array} \right\} (4)$$

Results and Discussion

Table 1 summarizes the track density ρ (tracks/cm^2), the radon concentration C_{Rn} (Bq/m^3), the potential alpha energy concentration *PAEC* (*WL*), the absorption effective dose equivalent *AEDE* (mSv.y^{-1}) and the lung cancer cases per year per 10^6 persons in different dwellings in Bashika district. Fig. 2 shows the radon concentration in dwellings with the location number in Bashika district. The analysis of the measured values of radon concentration shows that there is only one dwelling with a value of more than 50 Bq/m^3, six dwellings with values between (30-49) Bq/m^3 and three dwellings with values less than 30 Bq.m^{-3}. The lowest radon concentration was measured in dwelling no.5 which is 18.32 Bq/m^3 and the highest was in dwelling no.7 which is 54.87 Bq/m^3. It is believed that the reason behind the high ^{222}Rn level in dwelling no.7 (Bartilla root) is due to the presence of uranium, where its average content in Bartilla soil was found to be 5.27 ppm [13]. The average radon concentration for all the studied dwellings was 33.44 Bq/m^3, which lies below the acceptable ^{222}Rn limits of (50-150) Bq/m^3 recommended by the ICRP. The ICRP refined this recommendation in 2014 in Publication126. The commission now “strongly encourages national authorities to set a national derived reference level that is as low as reasonably achievable in the range of 100-300 Bq/m^3, taking the prevailing economic and societal circumstances into account” [14]. This is because exposure to radon earlier in life increases the risk of developing lung cancer during lifetime. The Canadian radon guideline recommends that remedial measures be undertaken in a dwelling whenever the average annual radon concentration exceeds 200 Bq/m^3 in the normal occupancy area, and the higher the radon concentration, the sooner remedial measures should be undertaken [15]. The ^{222}Rn concentration levels in Bashika district are lower than those found in other regions in Iraq (northern of Baghdad), like Erbil governorate (44 Bq/m^3) [1]. The variation in radon concentrations is fundamentally related to the type of construction, ventilation rate, size and age of the building. The average ^{222}Rn concentration was found to be lower than those measured by other works in other countries (see Table 2) [16]. The potential alpha energy concentration (*PAEC*) levels range between (1.98-5.92) × 10^{-3} *WL* with an average value of 3.61×10^{-3} *WL*. The average absorption effective dose equivalent for a person living in one of the homes for which the investigation was done was found to be 0.79 mSv/y. In the recent report of the ICRP, the recommended action levels of radon in dwellings should be within the range of (3-10) *mSv* [17]. On the basis of this ICRP recommendation, it has been observed that the dwellings monitored for indoor ^{222}Rn concentration show values below the action levels. According to our estimations, the ^{222}Rn induced lung cancer risk for dwellings in Bashika district ranges from 7.83 to 23.47 with an average of 14.31 per 10^6 persons.

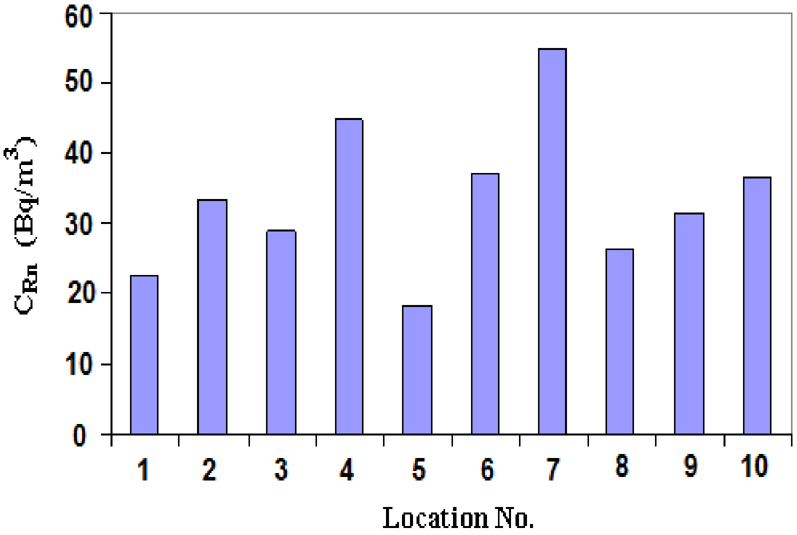

FIG. 2. Histogram of radon concentration in dwellings versus location number.

TABLE 1. Radon concentration, potential alpha energy concentration, absorption effective dose equivalent and lung cancer cases in Bashika district

No.	Location	ρ Tr./cm^2	C_{Rn} Bq/m^3	PAEC WL x10^{-3}	PAEC$^{(a)}$ WLM/y	AEDE mSv/y	Lung Cancer Cases /10^6 person
1	Oil Station	732	22.693	2.45	0.09	0.53	9.70
2	Rass Al-Aien	1074	33.29	3.59	0.14	0.79	14.25
3	Al-Islaam Cartier	930	28.83	3.11	0.12	0.68	12.27
4	Bashika Center	1442	44.70	4.83	0.19	1.06	19.11
5	Al-Kaba Cartier	591	18.32	1.98	0.07	0.43	7.83
6	Al-Fathlya Root	1200	37.20	4.02	0.16	0.88	15.94
7	Bartilla Root	1770	54.87	5.92	0.23	1.30	23.47
8	Al-Rabee Cartier	849	26.32	2.84	0.11	0.62	11.28
9	Al-Shabak Cartier	1020	31.62	3.42	0.13	0.75	13.57
10	Bahzany	1180	36.58	3.95	0.15	0.86	15.64
	Average	1078.8	33.45	3.61	0.14	0.79	14.31

(a) PAEC (WLM/Y) = PAEC (WL) × 40 taken from refs. [1, 16].

TABLE 2. Arithmetic mean of radon concentrations in dwellings in various European countries based on UNSCEAR [4, 18]

Country	C_{Rn} (Bq/m^3)	Country	C_{Rn} (Bq/m^3)
Denmark	53	Hungary	107
Finland	120	Poland	41
Sweden	108	Romania	45
Belgium	48	Slovakia	87
France	62	Italy	75
Germany	50	Spain	86
Switzerland	70	Bashika (Iraq)	34
Australia	11	Korea	53
Italy	70	Uk	20
USA	46		

Conclusions

As the ^{222}Rn induced lung cancer risk for dwellings in Bashika district ranges from 7.83 to 23.47 with an average of about 14.31 per10^6 persons, this implies that people who live in these dwellings are subjected to a relatively low risk factor for radon induced lung cancer.

References

[1] Mansur, H.H., Radiation Measurement, 40 (2005) 544.

[2] Banman, A., Hervat, D.J., Lokobauer, N., In Vahra, K.J. et al., "Natural Radiation Environment", (Eds), (Willy Rastern Ltd., New Delhi, 401, 1982).

[3] Al-Kofahi, M.M., Khader, B.R., Lehlooh, A.D. and Kullab, M.K., Nucl. Tracks Radiat. Meas., 20 (1992) 377.

[4] UNSCEAR, "United Nations Scientific Committee on the Effect of Atomic Radiation", (Sources and Effects of Ionizing Radiation, 1, 2000).

[5] Darby, S.C. and Hill, D.C., Radiation Protection Dosimetry, 104(4) (2003) 321.

[6] Denton, G.R.W. and Namazi, S., Procedia Environmental Sciences, 18 (2013) 157.

[7] Mortazavi, S.M.J., Ghiassi-Nejad, M. and Rezaiean, M., International Congress Series, 1276 (2005) 436.

[8] UNSCEAR, "United Nations Scientific Committee on the Effect of Atomic Radiation", (United Nations, New York, 1998).

[9] Barillon, R., Klein, D., Chambaudet, A., Membrey, F. and Fromm, M., Nuclear Tracks Radiat. Meas., 19(1-4) (1991) 291.

[10] Neri, A., Stewart, S.L. and Angell, W., Prev. Chronic. Dis. 10 (2013) 120337.

[11] Al-Bataina, B.A., Ismail, A.M., Kullab, M.K., Abumurad, K.M. and Mustafa, H., Radiat. Meas., 28 (1-6) (1997) 591.

[12] Reto, C. and Werner, B., Radiat. Phys., 34(2) (1989) 251.

[13] Hasan, H.I., Ph.D. Thesis, Dept. of Physics, College of Science, Mosul University, (2004), Iraq.

[14] Gue, L., "Revisiting Canadas Radon Guideline", (David Suzuki Foundation, 2015).

[15] Chen, J., Int. J. Environ. Res. Public Health, 10 (2013) 1916.

[16] Lagarde, F., Axelsson, G., Damker, L., Mellander, H., Nyberg, F. and Pershagen, G., Epidemiology, 12 (2001) 396.

[17] ICRP, "Lung Cancer Risk from Indoor Exposure to Radon Daughters", Publication 66, 2000.

[18] IAEA,"National and Regional Surveys of Radon Concentration in Dwellings", Analytical Quality in Nuclear Applications, Series No. 33, Vienna, 2013.

Volume 9, Number 2, 2016. pp. 87-93

Jordan Journal of Physics

ARTICLE

Variational Calculations of the Exchange Energy of a Two-Electron Quantum Dot in a Magnetic Field

A. Shaer, M.K. ELSAID and M. Elhasan

Physics Department, Faculty of Science, An-Najah National University, Nablus, West Bank, Palestine.

Received on: 2/3/2016; Accepted on: 21/7/2016

Abstract: The ground-state energies of a two-electron quantum dot are calculated using the variational calculation method to solve the relative part Hamiltonian of a two-dimensional quantum dot presented in a uniform magnetic field. We have shown the dependence of the exchange energy of the two-electron quantum dot on the confining frequency and strength of the magnetic field. The transitions in the angular momentum and spin of the quantum dot ground state are also shown. Based on comparisons with different works, the variational method gives very good results.

Keywords: Quantum dots; Variational method; Magnetic field; Exchange energy.

PACS: 73.21. La; 61.30.Gd; 31.15.Pf; 71.70.Gn

Introduction

Quantum dots (QDs), or artificial atoms, have been the subject of intense research studies over the past few years. The growing interest is motivated by the physical effects and potential device applications. Different experimental [1-5] and theoretical [6-31] studies have been conducted to investigate the energy spectrum and the correlation effects of the interacting electrons confined in a quantum dot in the presence of an applied uniform magnetic field. One of the most interesting features of electron correlation is the change of the spin and angular momenta structure in the ground state of the QD system in the presence of the magnetic field. The QD, in this case, has the potential to serve as a qubit of a quantum computer, since the magnetic field can be used to tune the transition in the spin of the ground state of the quantum dot from singlet (S=0) to triplet (S=1) state [28-30]. In this work, we shall use the variational method to solve the relative part Hamiltonian of a two-dimensional (2D) quantum dot under the effect of a magnetic field. We shall compare our computed results against the corresponding ones produced by different authors [29-31].

The Quantum Dot Hamiltonian

The effective-mass two-dimensional Hamiltonian for two interacting electrons confined in a quantum dot-helium by a parabolic potential in a uniform magnetic field of strength B is given as:

$$H = \left\{ \sum_{i=1}^{2} \left\{ \frac{p_i^2}{2m^*} + \frac{1}{2} m^* \left[\omega_0^2 + \frac{\omega_c^2}{4} \right] r_i^2 + \frac{\omega_c}{2} \hat{L}_{i_z} \right\} + \frac{e^2}{\kappa \left| \vec{r}_2 - \vec{r}_1 \right|} \right\} ; \quad (1)$$

where ω_0 is the confining frequency and κ is the dielectric constant for the GaAs medium. $\vec{r}_1$ and $\vec{r}_2$ describe the positions of the first and second electrons in the xy-plane. $\omega_c = \frac{eB}{m^* c}$ is the cyclotron frequency and the symmetric

Corresponding Author: M. K. Elsaid **Email**: mkelsaid@najah.edu

gauge $\vec{A}_i = \frac{1}{2}\vec{B}\times\vec{r}_i$ is used in Eq.(1). Upon introducing the center-of-mass (cm) $\vec{R} = \frac{\vec{r}_1 + \vec{r}_2}{2}$ and the relative coordinates $\vec{r} = \vec{r}_1 - \vec{r}_2$, the Hamiltonian in Eq.(1) can be decoupled to a center-of-mass $\left(H_R\right)$ and a relative $\left(H_r\right)$ parts. The cm-part is a harmonic oscillator type with well-known eigenenergies [27, 29, 30]:

$$\left.\begin{aligned} E_{cm} &= \left(2n_{cm} + |m_{cm}| + 1\right)\hbar\left[\omega_0^2 + \frac{\omega_c^2}{4}\right]^{1/2} \\ &\quad + m_{cm}\frac{\hbar\omega_c}{2} \end{aligned}\right\}; \tag{2}$$

where $n_{cm} = 0,1,2,\ldots$ and $m_{cm} = 0 \pm 1, \pm 2, \ldots$.

The main task in this work is to solve the relative two-dimensional Hamiltonian part,

$$\left.\begin{aligned} H_r &= \frac{p^2}{2\mu} + \frac{1}{4}\left[\omega_0^2 + \frac{\omega_c^2}{4}\right]r^2 \\ &\quad + \frac{e^2}{\kappa|\vec{r}|} + m\frac{\hbar\omega_c}{2} \end{aligned}\right\} \tag{3}$$

by using the variational calculation method.

Variational Calculation Method

Dyblaski, in a recent work [31], has used successfully the variational method to study the electronic structure of the quantum dot. Encouraged by the accuracy of the variational method used in Ref. [31], we apply the variational technique to calculate the complete eigenenergy spectra of the QD Hamiltonian and the exchange energy (J) as a function of confining frequency and magnetic field strength. In this work, we adopted a one- variation parameter wave function as:

$$\psi(r) = \sqrt[4]{\alpha}\,\frac{u_m(\rho)e^{im\phi}}{\sqrt{2\pi}\,\sqrt{\rho}}; \tag{4}$$

where:

$$u_m(\rho) = \rho^{1/2+|m|}(1 + \beta\rho)e^{-\left(\frac{\rho^2}{2}\right)}; \tag{5}$$

$$\rho = \sqrt{\alpha}\,r. \tag{6}$$

The first power term and the third exponential term in the wave function $u_m(\rho)$ in Eq. (5) both give the correct asymptotic behaviors as $\rho \to 0 \; and \; \rho \to \infty$, respectively. In addition, these states are a very good choice, because they are the eigenstates of parabolically confined electrons in a magnetic field, and the parabolic form is a successful potential model used by many authors in different works to study and explain the behavior of electronic, thermal and magnetic properties of the quantum dot.

The Schrödinger equation, with complete two-dimensional Hamiltonian form and full variational wave function can be written as:

$$\left(-\frac{\hbar^2}{m}\left(r^{-1/2}\frac{\partial^2}{\partial r^2}r^{1/2} + \frac{1}{r^2}\left(\frac{\partial^2}{\partial\phi^2} + \frac{1}{4}\right)\right) + 4\,mr^2\,\alpha^2 - \frac{1}{2}i\hbar\frac{\partial}{\partial\phi}\,\omega_c + \frac{e^2}{\epsilon|r|}\right)\sqrt[4]{\alpha}\,\frac{u_m(\rho)e^{im\phi}}{\sqrt{2\pi}\,\sqrt{\rho}} = E_r\,\sqrt[4]{\alpha}\,\frac{u_m(\rho)e^{im\phi}}{\sqrt{2\pi}\,\sqrt{\rho}} \tag{7}$$

In our calculations, we have used the following atomic Rydberg units:

$e^2 = 2, \hbar = 1, m = 1, \epsilon = 1$.

Finally, the relative Hamiltonian part is:

$$-2\frac{d^2}{dr^2} + 2\left(m^2 - \frac{1}{4}\right)\frac{1}{r^2} + \frac{1}{2}\omega_c m + 2r^2\alpha^2 + \frac{2}{r} \tag{8}$$

We have normalized our wave function:

$$u_m(\rho) = C_m\,\rho^{1/2+|m|}(1 + \beta\rho)e^{-\left(\frac{\rho^2}{2}\right)} \tag{9}$$

by calculating the normalizing constant as:

$$C_m^2 = \frac{2\sqrt{\alpha}}{(1+\beta^2)\Gamma[1+|m|] + \beta^2|m|\Gamma[1+|m|] + 2\beta\Gamma\left[\frac{3}{2}+|m|\right]} \tag{10}$$

The above normalization constant can be expressed in terms of new parameters,

$$C_m^2 - \frac{\sqrt{\alpha}}{d + e\beta + f\beta^2}; \tag{11}$$

where:

$$d = \frac{1}{2\,\Gamma[1+|m|]}; \tag{12}$$

$$e = \Gamma\left[\frac{3}{2} + |m|\right]; \tag{13}$$

$$f = \frac{1}{2\Gamma[2+|m|]}. \tag{14}$$

We have found the energy spectra of the relative part Hamiltonian:

$$\frac{1}{2}\omega_c m+\frac{C_m^2\times 2\alpha}{\sqrt{\alpha}}\left(\frac{1}{2}m^2\Gamma[|m|]+\frac{1}{2}|m|\Gamma[|m|]+\frac{5}{8}\beta^2|m|\Gamma[|m|]+\frac{1}{2}m^2\beta^2\Gamma[|m|]+\frac{\Gamma\left[\frac{1}{2}+|m|\right]}{2\sqrt{\alpha}}-\frac{1}{4}\beta\Gamma\left[\frac{1}{2}+|m|\right]+m^2\beta\Gamma\left[\frac{1}{2}+|m|\right]+\frac{\beta^2\Gamma\left[\frac{1}{2}+|m|\right]}{4\sqrt{\alpha}}+\frac{\beta^2|m|\Gamma\left[\frac{1}{2}+|m|\right]}{2\sqrt{\alpha}}+\frac{\beta\Gamma[1+|m|]}{\sqrt{\alpha}}-\frac{1}{8}\beta^2\Gamma[1+|m|]+\frac{1}{2}m^2\beta^2\Gamma[1+|m|]+\beta\Gamma\left[\frac{3}{2}+|m|\right]+\frac{1}{2}\Gamma[2+|m|]+\beta^2\Gamma[2+|m|]+\frac{1}{2}\beta^2|m|\Gamma[2+|m|]+\beta\Gamma\left[\frac{5}{2}+|m|\right]\right) \tag{15}$$

The energy matrix element in Eq. (15) can be rewritten in a closed form as:

$$E_r(\beta)=-\frac{1}{2}m\omega_c+2\alpha\frac{a+b\beta+c\beta^2}{d+e\beta+f\beta^2}\;; \tag{16}$$

where:

$$a=\frac{e}{(2|m|+1)\sqrt{\alpha}}+2f\;; \tag{17}$$

$$b=\frac{2d}{\sqrt{\alpha}}+2(|m|+1)e\;; \tag{18}$$

$$c=\frac{e}{2\sqrt{\alpha}}+(2|m|^2+4|m|+3)d\;. \tag{19}$$

The constants: d, e and f are as defined previously in Eqs. (12-14).

The energy eigenvalues of H_r can be obtained by minimizing the energy expression in Eq. (16) with respect to the variational parameter (β); namely,

$$\frac{\partial E}{\partial \beta}=0,\frac{\partial^2 E}{\partial \beta^2}>0\;. \tag{20}$$

The value of the parameter β which satisfies the minimum energy requirement is:

$$\beta_{min,m}=\frac{2cd-2af-\sqrt{(2cd-2af)^2-4(bd-ae)(ce-bf)}}{2(-ce+bf)} \tag{21}$$

So, the final energy expression in terms of the variational parameter value which satisfies the minimization condition is:

$$E_r(\beta_{min})=-\frac{1}{2}m\omega_c+2\alpha\frac{a+b\beta_{min}+c\beta_{min}^2}{d+e\beta_{min}+f\beta_{min}^2} \tag{22}$$

Having obtained the eigenenergies for the QD system for any state labeled by quantum numbers: n, m, we are able to calculate the exchange energy (J) defined as:

$$J=E_{triplet}-E_{singlet} \tag{23}$$

for any range of magnetic field strength and parabolic potential confining frequency.

2. Results and Discussion

Our computed results for 2e quantum dot are presented in Figs. 1 to 4 and Tables 1 to 3. In Fig. 1, we have displayed the computed eigenenergies of the relative part 2D-Hamiltonian for two interacting electrons at a confining frequency of $\omega_0=\frac{2}{3}R^*$ in a QD system. The figure clearly shows the transitions in the angular momentum of the ground state energy as the magnetic field increases. The origin of these transitions is due to the effect of the Coulomb interaction energy in the QD Hamiltonian. For this purpose, we have plotted, in Fig. 2, the energy spectra of two independent (zero Coulomb interaction) QDs. The figure shows no energy level crossings, and the state with $m=0$ is always the ground state.On the other hand, the ground state of the interacting electron model of the QD oscillates with the angular momentum m as we have mentioned.For example, the angular momentum changes from $m=0\ to\ m=-1\ and\ m=-2$....Since the total spin of the two electrons is $S=\frac{[1-(-1)^m]}{2}$, this leads to an exchange in the sequence of the singlet (S) and triplet (T) states. These transitions in the angular momentum of the QD system are expected to manifest themselves as cusps in the spectra of thermodynamic quantities of the QD: like heat capacity, magnetization and magnetic susceptibility [7, 9,10]. Our computed results by the present variational method are also listed in Table 1 for the sake of comparison. The underlined energy values show the angular momentum transitions of the ground state of the QD. These underlined ground state transitions agree very well with the corresponding ones shown in Fig. 1 of Ref. [31]. We have also compared, in Table 2, the present computed results against the data of Ref. [29, 30]. The tabulated results (up to six significant figures) show excellent agreement between both works. In Fig. 3, we have plotted the exchange energy (J), defined in Eq. (23), as a function of magnetic field strength (ω_c) and confining frequency: $\omega_0 = 0.4\, R^*$ (solid line —) and $\omega_0 = 0.8\, R^*$ (dashed line – – –) .

The figure clearly shows the effect of the strength of the confining frequency ω_0 on the transition of the angular momentum of the ground state energy. As the confining frequency increases, the transiton (J =0) shifts to hihger magnetic field. For example, the first transition occurs at $\omega_c = 0.35$ for $\omega_0 = 0.4$, while for $\omega_0 = 0.8$ the trasition occurs at a higher confining frequency value, $\omega_c = 0.9$. This shows that as the parabolic confinement increases, more magnetic energy is needed to make the ground state transition. In Table 3, we have listed the values of the calculated exchange energy (J) as a function of ω_c for different values of confining frequency. Furthermore, we have displayed, in Fig. 4, the singlet-triplet phase diagram ($\omega_0 - \omega_c$) of the QD showing the singlet – triplet regions separated by J=0-lines.

TABLE 1. The ground state eigenenergies, in (R^*) ,calculated by using the variational method for various values of magnetic field strength (ω_c) and different angular momentum values (m=0, 1, 2, 3 and 4) of a QD system with a confining frequency, $\omega_0 = \frac{2}{3} R^*$. The underlined energy values show the angular momentum transitions of the QD ground state

	m				
ω_c	0	1	2	3	4
0.0	1.6998	2.000	2.5219	3.10835	3.7226
0.4	1.7566	1.8743	2.2218	2.6356	3.0780
0.8	1.9119	**1.8788**	2.0975	2.3876	2.7082
1.2	2.1341	1.9751	2.0992	2.3015	2.5371
1.6	2.3954	2.1286	2.1813	2.3200	2.4950
2.0	2.6708	2.3164	**2.3131**	2.4039	2.5341
2.4	2.9715	2.5246	2.4758	2.5292	2.6251
2.8	3.2702	2.7453	2.6583	2.6815	2.7502
3.2	3.5707	2.9737	2.8538	**2.8518**	2.8983
3.6	3.8714	3.2068	3.0580	3.0346	3.0624
4.0	3.2462	3.2381	3.2781	3.3348	3.4022

TABLE 2. The present ground state energies (in R^*) of QD as a function of dimensionless Coulomb coupling parameter $\lambda - \frac{e^2\alpha}{\hbar\omega}$ obtained from exact diagonlization method (second column) compared with reported work (third column) taken from Ref. [29, 30]. The parameter $\alpha = \sqrt{\frac{m\omega}{\hbar}}$ has the dimension of inverse length

λ	E(Present work)	E(Ref. [29, 30])
0	2.00000	2.00000
1	3.000969	3.00097
2	3.721433	3.72143
3	4.318718	4.31872
4	4.847800	4.84780
5	5.332238	5.33224
6	5.784291	5.78429
7	6.211285	6.21129
8	6.618042	6.61804
9	7.007949	7.00795
10	7.383507	7.38351

TABLE 3. The exchange energy (J), in meV, listed against the magnetic field strength ω_c for different QD confining frequencies: $\omega_0 = 0.4 \quad and \;\; 0.8 \;\; R^*$

ω_c	ω_0=0.4 R^*	ω_0=0.8 R^*
0.0	0.1492	0.3807
0.2	0.0558	0.2845
0.4	-0.0255	0.1959
0.6	-0.07852	0.1144
0.8	- 0.0346	0.0394
1.0	0.0009	-0.0295

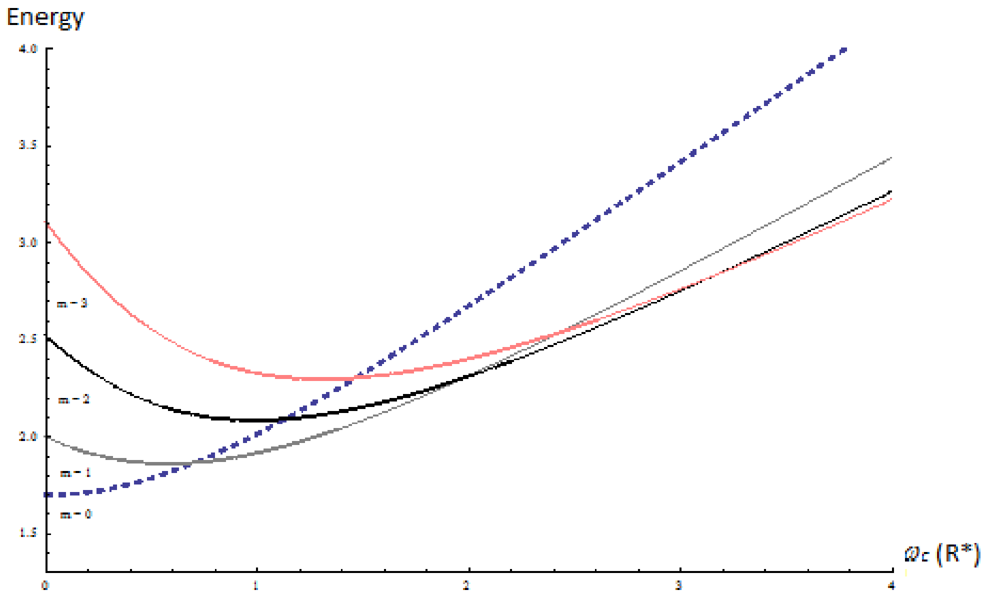

FIG. 1. The computed relative motion energy spectra (in R^*) of two interacting electrons quantum dot against the magnetic field strength ω_c $(in\ R^*)$ for a confining frequency $\omega_0 = \frac{2}{3}R^*$ and an angular momentum m = 0, 1, 2 and 3.

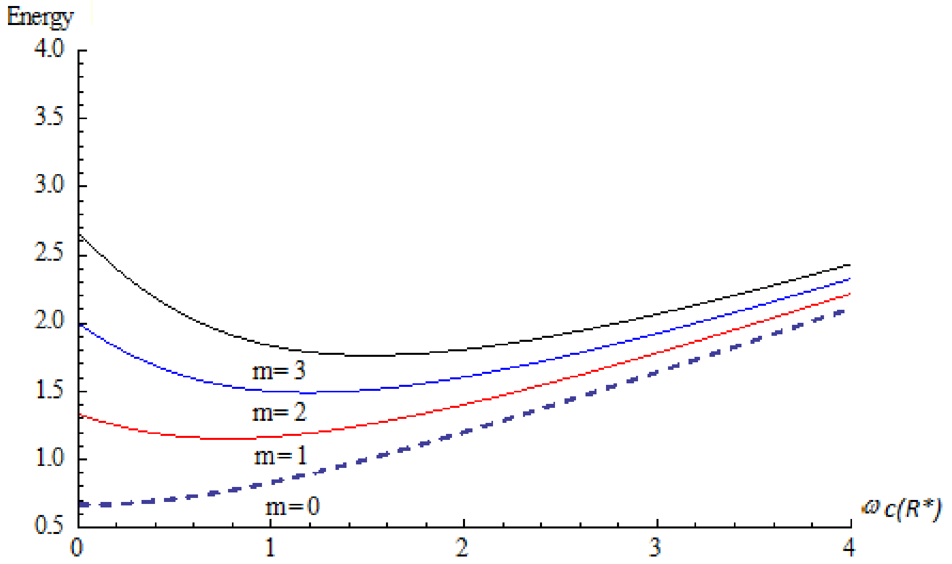

FIG. 2. The energy spectra (in R^*) of two non-interacting electrons (Coulomb=zero) in a quantum dot calculated at $\omega_0 = \frac{2}{3}R^*$ against the confining frequency ω_c $(in\ R^*)$.

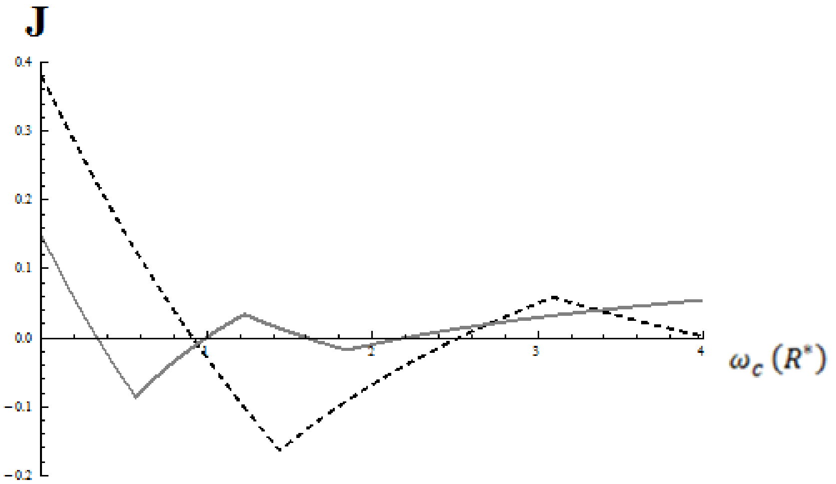

FIG. 3. The exchange energy, J, (in meV) against the magnetic field strength $\omega_c\ (in\ R^*)$ for QD confining frequencies $\omega_0 = 0.4\ R^*\ (solid\ \ line)\ \ and\ 0.8\ R^*\ (dashed\ line\ )$.

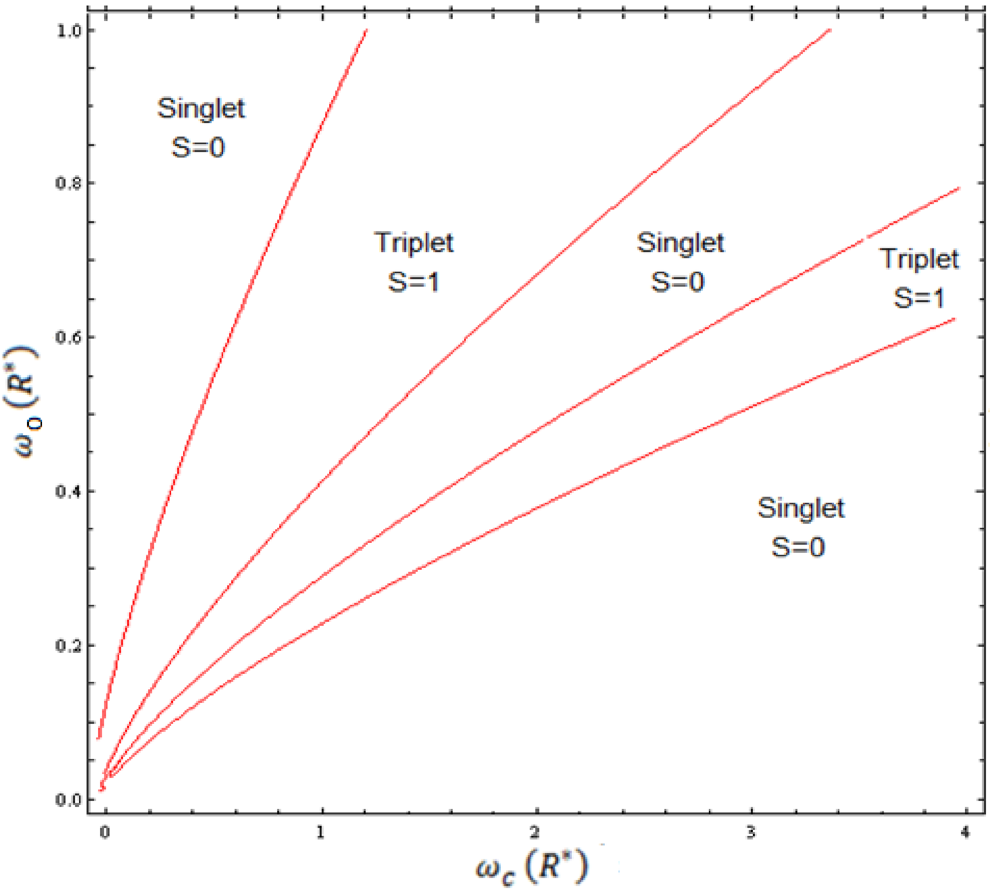

FIG. 4. The QD singlet-triplet phase diagram $(\omega_c - \omega_0)$. S=0, singlet and S=1, triplet states.

3. Conclusion

In conclusion, we have studied the ground state properties of the 2e QD in the presence of an applied uniform magnetic field. The ground state energies of the QD are calculated for various values of field strength and confining frequency. We also have shown the spin single-triplet transition in the ground state of the QD and the phase diagram. The present computed eigenenergy results, given in Figs. 1 and 2 and Tables 1 and 2 are compared with the corresponding ones in References [7, 29-31]. The comparisons give very good results for all ranges of the magnetic field strength and confining frequency of the QD system.

References

[1] Drexler, H. *et al.*, Phys. Rev. Lett., 73 (1994) 2252.

[2] Sikorski, C. and Merks, U., Phys. Rev. Lett., 62 (1989) 2164.

[3] Demel, T., Hietmann, D., Grambow, P. and Plog, K., Phys. Rev. Lett., 64 (1990) 788.

[4] Lorke, A., Kothaus, J.P. and Plog, K., Phys. Rev. Lett., 64 (1990) 2259.

[5] Ashoori, R.C. *et al.*, Phys. Rev. Lett., 71 (1993) 613.

[6] Makysm, P.A. and Chakraborty, T.T., Phys. Rev. Lett., 65 (1990) 108.

[7] Wagner, M., Merkt, U. and Chapllik, A.V., Phys. Rev. B, 45 (1992) 1951.

[8] Pfannkuche, D. and Gerharst, R.R., Physica B, 189 (1993) 6.

[9] S De Groote, J.J., Honos, J.E.M. and Chapllik, A.V., Phys. Rev. B, 46 (1992) 12773.

[10] Merkt, U., Huser, J. and Wagner, M., Phys. Rev. B, 43 (1991) 7320.

[11] Pfannkuche, D. and Gerhardts, R.R., Phys. Rev. B, 44 (1991) 13132.

[12] Zhu, K.D and Gu, S.W., Phys. Rev. Lett. A, 172 (1993) 296.

[13] Johnson, N.F. and Payne, M.C. Phys. Rev. Lett., 67 (1991) 1157.

[14] Klama, S. and Mishchenko, E.G., J. Phys. Condens. Matter, 10 (1998) 601.

[15] Zhu, J.L. *et al.*, Phys. Rev. B, 55 (1997) 15819.

[16] Dineykhan, M. and Nazmitdinov, R.G., Phys. Rev. B, 55 (1997) 133707.

[17] Bryant, G., Phys. Rev. Lett., 59 (1987) 1140.

[18] Zhu, J.L., Kawazoe, Y. and Yao, T., J. Phys. Condens. Matter, 11 (1999) 299.

[19] Animsomovas, E. and Matulis, A., J. Phys. Condens. Matter, 10 (1998) 601.

[20] Matulis, A. and Peeters, P.M., J. Phys. Condens. Matter, 6 (1994) 775.

[21] Blanter, Y.M., Kaputkina, N.E. and Lozovik, Y.E., Physica Scripta, 54 (1996) 539.

[22] Peters, F.M. and Schweigert, V.A., Phys. Rev. B, 53 (1996) 1468.

[23] Oh, J.H., Huang, K.J., Ihm, G. and Lee, S.J., Phys. Rev. B, 53 (1996) 13264.

[24] El-Said, M., Semicond. Sci. Technol., 10 (1995) 1310; Elsaid, M., Phys. Rev. B, 61 (2000) 13026.

[25] Nasmitdinov, R.G., Simonovic, N.S. and Rost, J.M., Phys. Rev. B, 65 (2002) 155307.

[26] Drouvelis, P.S., Schmelcher, P. and Diakonos, F.K., Phys. Rev. B, 69 (2004) 155312.

[27] Kandemir, B.S., Phys. Rev. B, 72 (2005) 165350.

[28] Burkard, G., Loss, D. and Di Vincenzo, D. P. Phys. Rev. B, 59 (1999) 2070.

[29] Ciftja, O. and Faruk, M.G., Phys. Rev. B, 72 (2005) 205334.

[30] Ciftja, O. and Anil Kumar, A., Phys. Rev. B, 70 (2004) 205326.

[31] Dyblaski, W. and Hawrylak, P., Phys. Rev. B, 72 (2005) 205432.

Volume 9, Number 2, 2016. pp. 95-102

Jordan Journal of Physics

ARTICLE

The Change in the Properties of ^{130}Xe - ^{130}Nd Isobar States

Imad Mamdouh Ahmed

Department of Physics, College of Education for Pure Sciences, University of Mosul, Mosul, Iraq.

Received on: 3/3/2016; Accepted on: 20/6/2016

Abstract: The properties of the ground and negative parity state bands of ^{130}Xe - ^{130}Nd isobars have been studied. The ratio E_{γ}/I has been calculated as a function of the spin (I) to determine the ground-state evolution. The ratio between the energies of the (I+2) and (I) states as a function of the spin (I) has been drawn to determine the property of the ground-state band. The odd-even staggering has been drawn to determine the difference of the energies of ground state band and negative parity band. The energy levels for the ground state band of ^{130}Xe - ^{130}Nd have been calculated using Bohr-Mottelson Model (BM), Interacting Boson Model (IBM-1), Interacting Vector Boson Model (IVBM) and Doma-El-Gendy (D-G) relation. The energy levels of the negative parity band have been calculated using BM and IVBM models. The calculated energy levels in comparison with the experimental data indicated the quality of the fitness presented in this work.

Keywords: Ground- state band; Negative parity band; E-GOS; The ratio between the energies of I+2 and I states; IBM-1; IVBM; D-G relation; Bohr and Mottelson.

PACS numbers: 21.60.Ev, 21.60.Fw, 21.10.Re.

Introduction

The different even-even nuclei properties vary with the number of constituent nucleons, which is associated with the corresponding changes in the nuclear excitation spectrum and in the decay properties of the excited states [1,2]. Even-even nuclei energy levels could be grouped into Ground State Band (GSB) with $I^{\pi}=0^{+},2^{+},4^{+},....$ and Negative Parity Band (NPB) with $I^{\pi}=1^{-},3^{-},5^{-},...$[3]. GSB and NPB become interwoven after the first few values of angular momentum *I*, forming a single octupole band with $I^{\pi}=0^{+},1^{-},2^{+},3^{-},.....$ [4-7]. Primary information on the property of the nucleus could be obtained from the position of the first excited state $(E2_{1}^{+})$ which is approximately equal 100, 300 and 500 keV and the ratio of the second excited state to the first excited state $(R=E4_{1}^{+}/E2_{1}^{+})$ which obeys $3<R\leq 3.3$, $2.4<R\leq 3$ *and* $2\leq R\leq 2.4$ for rotational, γ-soft and vibration nuclei, respectively [8]. The relationship between the gamma energy over spin E_{γ}/I as a function of the spin *I* (E-GOS) has indicated good information on the evolution that occurs in the yrast line of the nuclei. This was introduced by Regan *et al.* [9]. They have studied many nuclei around A=110 regions and observed the evolution in their yrast states [9]. The ratio between the energies of *I+2* and *I* states gives a good indication of the property of the nucleus [10,11], when being drawn *versus I* and then compared with the standard values of the vibration U(5), rotational SU(3) and γ-soft O(6) nuclei. A relation of the rotational energy *E* of an axially symmetric nucleus as a function of *I(I+1)* has been introduced by Bohr and Mottelson (BM) [3]. The complicated level scheme properties were well approximated in terms of the U(6) unitary group in interacting

Corresponding Author: Imad Mamdouh Ahmed **Email**: imad_mamdouh07@yahoo.com

boson model (IBM-1) studies. The group reduction scheme of the U(6) produces three limits that terminate in the O(2) group. The three limits are: the vibrational U(5), rotational SU(3) and γ-soft O(6) [12]. Nuclei might have an intermediate structure of the U(5) - SU(3), U(5)-O(6) and SU(3) - O(6) limits which is another phenomenological study [13]. The interacting vector boson model (IVBM) is based on two kinds of vector bosons, the proton *p* and the neutron *n* bosons that constitute the collective excitations in the nucleus. The IVBM developed by Ganev *et al.* [14] is used to describe the ground and octupole bands of the nucleus. Doma and El-Gendy (D-G) [15] applied the collective model to calculate the rotational and vibrational energies of some even-even nuclei. They introduced a new equation which depends on the moment of inertia as well as on the spin of the nucleus [15].

Many studies have been concerned with nuclei of mass $A \approx 130$ region. One of these studies tested the O(6) symmetry to ^{130}Xe,^{130}Ba and observed some deviation from a pure O(6) character. So, the authors added an SU(3) perturbation to the Hamiltonian [16]. P. Von *et al.* tested the O(6)-U(5) character of nuclei with $A = 130$ region [17]. L. Bettemana *et al.* compared the O(6) and O(6)-U(5) calculations with experimental and other calculation results of ^{130}Xe, ^{130}Ba and ^{130}Ce. They found that the O(6)-U(5) calculations are more reliable [18]. Salah A. Eid and M. Diab considered the ^{130}Xe nucleus that has the E(5) symmetry, where they used IBM-1 to calculate its energy levels and compared them with the measured values [19]. Since there are many opinions on these regions, in the present work, the E-GOS, the ratio of the energy states and the staggering methods are introduced to insure the property of ^{130}Xe – ^{130}Nd isobars. After indicating the property of each isobar, the energy levels of the GSB are calculated using the following models; BM, IBM-1, IVBM and D-G relation and the energy levels of NPB are also calculated using BM and IVBM models, for ^{130}Xe - ^{130}Nd isobars, then the results are compared with their experimental counterparts.

Methods of Calculation

The E-GOS method gives good information on the evolution in the excited states of several even-even nuclei when the plot of E_γ / I *versus* *I* is studied. A vibrational nucleus in the E-GOS curve drops quickly from its highest value (≈250keV) at $(I = 2_1^+)$ to its lower value (0) at (I→∞). For γ-soft nuclei, the curve drops slowly from its highest value (≈150keV) at $(I = 2_1^+)$ to the quartered first excited state $E2_1^+/4$ at (*I*→∞), but for rotational nuclei the curve increases slowly from its smallest value (≈50keV) at $(I = 2_1^+)$ to its highest value which is $4\hbar^2/2\vartheta$ at (I→∞) [9]. The relationships between gamma energy over spin $R = E_\gamma / I$ and the spin *I* for the three limit cases are given by [20,21]:

$$\text{Vibrator: } R = \frac{\hbar\omega}{I} \to 0 \text{ when } I\to\infty \ . \tag{1}$$

$$\text{Rotor: } R = \frac{\hbar^2}{2\vartheta}\left(4 - \frac{2}{I}\right) \to 4\frac{\hbar^2}{2\vartheta} \text{ when } I\to\infty \ . \tag{2}$$

$$\gamma\text{-soft: } R = \frac{E2_1^+}{4}\left(1 + \frac{2}{I}\right) \to \frac{E2_1^+}{4} \text{ when } I\to\infty . \tag{3}$$

The ratio between the experimental energy values of I+2 and I states as a function of I has been constructed to define the symmetry for the excited states of even-even nuclei [10, 11]:

$$\left. \begin{aligned} r\left(\frac{I+2}{I}\right) = \left[\left(\frac{R(I+2)}{I}\right)_{\text{exp.}} - \frac{(I+2)}{I}\right] \\ \times \frac{I(I+1)}{2(I+2)} \end{aligned} \right\} ; \tag{4}$$

where $\left(\frac{R(I+2)}{I}\right)_{\text{exp.}}$ is the experimental energy values ratio between I+2 and I states. The value of (r) has changed from 0.1 to 1.0 for yrast bands of even-even nuclei. The ratio (r) for vibrational, rotational and transitional nuclei is given by:

$0.1 \le r \le 0.35$ for vibrational nuclei.

$0.4 \le r \le 0.6$ for transitional nuclei.

$0.6 \le r \le 1.0$ for rotational nuclei.

In BM model, for small I, the energy E(I) can be expanded in power of I(I+1). The GSB and NPB levels are given by [3,6]:

$$E(I) = AI(I+1) - BI^2(I+1)^2 + CI^3(I+1)^3 ; \tag{5}$$

$$E(I) = E_0 + AI(I+1) - BI^2(I+1)^2 + CI^3(I+1)^3 ; \tag{6}$$

where E_0 is the band head energy of the NPB. The values of the coefficients A, B and C can be determined from a fitting to the available measured energy levels of the band.

The general Hamiltonian for IBM-1 is given by [22]:

$$H = \sum_{i=1}^{N} \varepsilon_i + \sum_{i<j}^{N} V_{ij} \quad ; \tag{7}$$

where ε is the intrinsic boson energy and V_{ij} is the interaction strength between bosons i and j. The multipole form the Hamiltonian is [23]:

$$\left.\begin{aligned} H &= \varepsilon\,\hat{n}_d + a_0\hat{P}^{+}\hat{P} + a_1\hat{L}.\hat{L} \\ &\quad + a_2\hat{Q}.\hat{Q} + a_3\hat{T}_3.\hat{T}_3 + a_4\hat{T}_4.\hat{T}_4 \end{aligned}\right\} ; \tag{8}$$

where n_d is the number of d-bosons; $P{\cdot}P$, $L{\cdot}L$, $Q \cdot Q$, $T3 \cdot T3$ and $T4 \cdot T4$ represent pairing, angular momentum, quadrupole, octupole and hexadecupole interactions between the bosons, while a_0, a_1, a_2, a_3 and a_4 are strengths of interaction of each term, respectively. The Hamiltonian used in terms of multipole expansion tends to reduce three forms of it to meet the requirements of the three symmetry limits; the vibrational U(5), rotational SU(3) and γ-soft O(6). In the U(5) limit, the effective parameter is ε. In the O(6) limit, the dominating parameter is a_o. In the SU(3) limit, the effective parameter is a_2. The eigenvalues for these three limits are given by [24]:

U(5):

$$\left.\begin{aligned} E(\varepsilon, n_d, v, L) &= \varepsilon\,\hat{n}_d + K_1 n_d(n_d+4) \\ &\quad + K_4 v(v+3) + K_5 L(L+1) \end{aligned}\right\} ; \tag{9}$$

O(6):

$$\left.\begin{aligned} E(\sigma, \tau, L) &= K_3[N(N+4) - \sigma(\sigma+4)] \\ &\quad + K_4\tau(\tau+3) + K_5 L(L+1) \end{aligned}\right\} ; \tag{10}$$

SU(3):

$$\left.\begin{aligned} E(\lambda, \mu, L) &= K_2(\lambda^2 + \mu^2 + 3(\lambda+\mu) \\ &\quad + \lambda\mu) + K_5 L(L+1) \end{aligned}\right\} ; \tag{11}$$

where, K_1, K_2, K_3, K_4 and K_5 are other forms of the strength of parameters. v is the number of bosons not coupled to zero angular momentum in U(5) symmetry, L is the angular momentum of the nucleus, N is the number of bosons in the nucleus, σ is the number of bosons not coupled to zero angular momentum in O(6) symmetry, τ is the number of d bosons s not coupled to zero and (λ, μ) are the angular momentum of bosons and its third component, respectively. Many nuclei have a transition property between two or three of the above limits and their eigenvalues for the yrast states are given by [23]:

U(5)-O(6):

$$\left.\begin{aligned} E(\varepsilon, n_d, \tau, L) &= \varepsilon\hat{n}_d + K_1 n_d(n_d+4) \\ &\quad + K_4\tau(\tau+3) + K_5 L(L+1) \end{aligned}\right\} ; \tag{12}$$

U(5)-SU(3):

$$\left.\begin{aligned} E(\varepsilon, \lambda, L) &= \varepsilon\hat{n}_d + K_2(\lambda^2 + 3(\lambda+\mu)) \\ &\quad + K_5 L(L+1) \end{aligned}\right\} ; \tag{13}$$

O(6)-SU(3):

$$\left.\begin{aligned} E(\tau, \lambda, L) &= K_2(\lambda^2 + 3(\lambda+\mu)) \\ &\quad + K_4\tau(\tau+3) + K_5 L(L+1) \end{aligned}\right\} . \tag{14}$$

The eigenvalues for the GSB and NPB states in IVBM are given by [7]:

$$E(I) = \beta I(I+1) + \gamma I \ . \tag{15}$$

$$E(I) = \beta I(I+1) + (\gamma + \eta) I + \zeta \ . \tag{16}$$

The values of β and γ can be determined from a fitness to the positive GSB, while η and ζ are estimated from the fitness to NPB. Analyzing Eqs. (15) and (16), it can be seen that the eigenstates of the GSB and NPB states consist of rotational *I(I+1)* and vibrational *I* modes. Doma and El-Gendy have derived a new formula of the rotational energy levels, that depends upon the spin *I* and the nuclear moment of inertia ϑ, by analyzing the well-known experimental rotational energy levels of the even-even deformed nuclei in the high mass region in the following simple form [15]:

$$E(I) = \frac{A I(I+1)}{\left[1 + \dfrac{D I(I+1)}{1 - C I(I+1)}\right]} \ ; \tag{17}$$

where *A* is the reciprocal moment of inertia of the nucleus, $A = \dfrac{\hbar^2}{2\vartheta}$. The values of *D* and *C* can be determined from a fit to the GSB.

The odd-even staggering (or $\Delta I=1$ staggering) can be measured by the quantity [6]:

$$\Delta E_{1,\gamma}(I)=\frac{1}{16}\left\{\begin{pmatrix}6E_{1,\gamma}(I)-4E_{1,\gamma}(I-1)\\ -4E_{1,\gamma}(I+1)\\ +E_{1,\gamma}(I-2)+E_{1,\gamma}(I+2)\end{pmatrix}\right\}; \quad (18)$$

where the transition energies are:

$$E_{1,\gamma}(I) = E(I+1) - E(I). \quad (19)$$

The quantity $\Delta E_{1,\gamma}(I)$ exhibits values of alternating sign over an extended region of the angular momentum. Odd-even staggering starts from relatively high values and then decreases with increasing angular momentum. Reaching a vanishing value ($\Delta E_{1,\gamma}(I)=0$), after staggering starts raising and then dropping again, it gives an overall picture of beats. When the staggering reaches a vanishing value, a phase change takes place [6].

Results and Discussion

Useful information on the shape transition of even-even nuclei can be obtained from the first excited state, the ratio of the second to the first excited states R(4/2), E-GOS curve and the ratio $r\left(\frac{(I+2)}{I}\right)$. Experimental energy levels of the ground and negative parity state band of $^{130}Xe{-}^{130}Nd$ isobars were taken from Ref. [25]. Table 1 shows the values of first excited states and the ratios R(4/2) for these isobars, which primarily indicate the vibrational property of ^{130}Xe nucleus, the γ-soft property of ^{130}Ba and ^{130}Ce nuclei and the rotational property of ^{130}Nd nucleus.

TABLE 1. Experimental values [25] of $E2_1^+$ and the ratio $R(4/2)=\frac{E\,4_1^+}{E\,2_1^+}$ for ^{130}Xe - ^{130}Nd isobars

Isobar	^{130}Xe	^{130}Ba	^{130}Ce	^{130}Nd
$E2_1^+$(keV)	536.07	357.38	253.85	159.05
R4/2	2.247	2.523	2.798	3.052

Fig. 1 shows the E-GOS curves of the ground state band of ^{130}Xe - ^{130}Nd isobars. A comparison of these curves with the ideal limits of vibrational, rotational and γ-soft nuclei gives good information of the property of the states of the isobars. The high drop of the curve of ^{130}Xe from the first excited state 2_1^+ to 10_1^+ state gives this isobar the vibrational property, but the behavior of the curve changes after the 10_1^+ state. The slow drop of the curve of ^{130}Ba gives it the γ-soft property. The behavior of the curve of ^{130}Ce is the slow drop of values up to 10_1^+ state, giving it the γ-soft property, and the behavior changes after this state. The curve of ^{130}Nd primarily raises slowly, then drops slowly which gives it the rotational- γ-soft property.

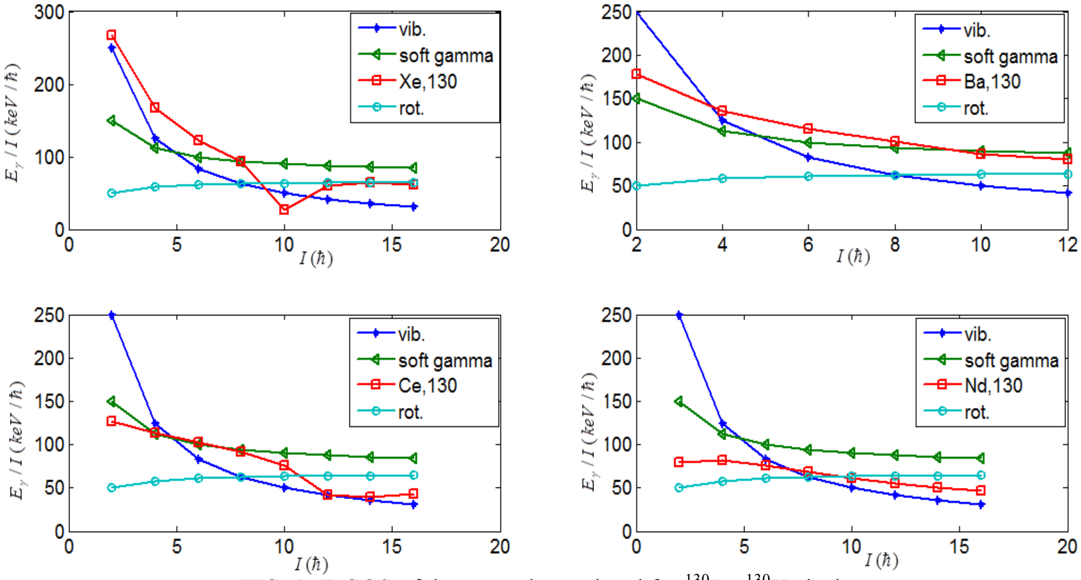

FIG. 1. E-GOS of the ground-state band for ^{130}Ba-^{130}Xe isobars.

Neither the first of two excited states nor the E-GOS curve gives the exact property of each isobar. For this reason, the relation between $r\left(\frac{I+2}{I}\right)$ and I is plotted and compared with the behavior of vibrational U(5), rotational SU(3) and γ-soft O(6) nuclei. Fig. 2 shows these curves, where the ratio for all values of I in ^{130}Xe is smaller than 0.5 passing limit values of the vibrational limit which gives this nucleus the U(5)-O(6) character. This ratio for ^{130}Ba is alternative within the limits of O(6) nuclei, which gives this property for this nucleus. However, the ratio $r\left(\frac{I+2}{I}\right)$ of ^{130}Ce is changed from the O(6) character to the 10_1^+ state and the character has been changed to the SU(3) after this state, while the ratio of ^{130}Nd nucleus is smaller than 0.8 and greater than 0.46, which gives an SU(3)-O(6) property to this nucleus.

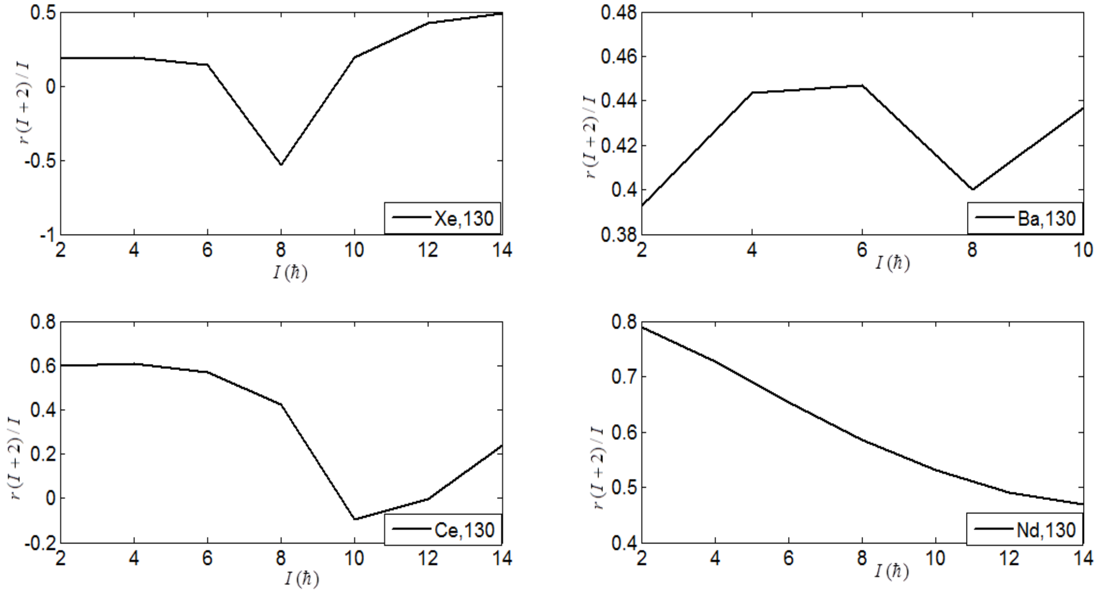

FIG. 2. The ratio $r(\frac{I+2}{I})$ as a function of I for ^{130}Ba-Xe isobars.

Fig. 3 shows the application of Eq. (18) to find out the experimental staggering factor $\Delta E_{1,\gamma}(I)$ of ^{130}*Xe*-^{130}*Nd* isobars. In all cases, one obtains a clearly pronounced staggering pattern, that is a zigzagging behavior of the quantity $\Delta E_{1,\gamma}(I)$ as a function of angular momentum I. The vanishing value of the staggering $\Delta E_{1,\gamma}(I)=0$ has not been reached, which means that each isobar has a saturation in its property along with its states; that is ^{130}*Xe* has a pure U(5) character, ^{130}*Ba* and ^{130}*Ce* have an O(6) character and ^{130}*Nd* stays in the SU(3)-O(6) property.

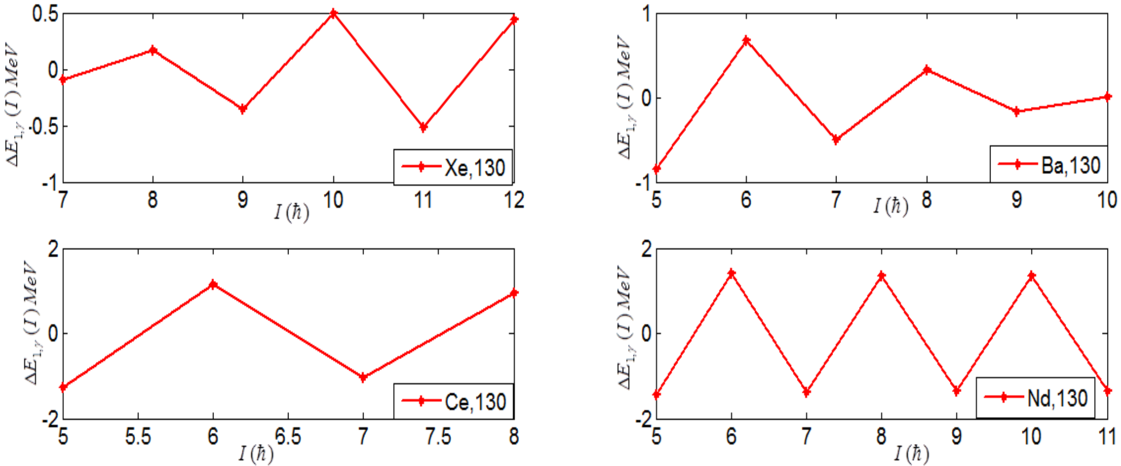

FIG. 3. Experimental staggering of ^{130}*Xe*-^{130}*Nd* isobars.

MATLAB 6.5 software is used to calculate the energy levels of the GSB and the NPB for ^{130}Xe-^{130}Nd isobars using BM, IBM-1, IVBM and D-G methods. The number of bosons and the best values of the parameters which give the best fitting between theoretical and experimental energy levels of the above isobars are represented in Table 2, into which the number of bosons has been calculated from the sum of proton bosons of the closed shell with magic number (50) and the neutron bosons of the closed shell with magic number (82). Table 2 shows the values of parameter A for the D-G formula which is chosen to be $\frac{\hbar^2}{2\vartheta} = E2_1^+/6$ according to the rotational energy relation, where $E(I) = \frac{\hbar^2}{2\vartheta} I(I+1)$, while its values according to BM are close to $\frac{\hbar^2}{2\vartheta} = E2_1^+/6$ only for ^{130}Nd, since it is a rotational nucleus. The other two parameters B and C of BM and C and D of D-G are determined by fitting each of the equations with the measured energy levels. The parameter ε which occurs only for ^{130}Xe is close to $E2_1^+ = 536 keV$ due to the vibration characteristic of this nucleus. The parameter K_4 for ^{130}Ba has the biggest value in comparison with the other nuclei, which means that this nucleus is a more $\gamma - soft$ nucleus than any other nuclei. The value of γ parameter of IVBM is a vibrational one and one can observe that this value of the vibrational nucleus ^{130}Xe is the highest one, while the smallest value is for the rotational nucleus ^{130}Nd. The smallest value of the rotational β parameter is for ^{130}Xe and one expects that the highest value is for ^{130}Nd. However, this will not happen, because of the fitting of the measured value of energy with the IVBM equation. The best fitting parameters of the NPB of BM and IVBM are shown in Table 3. The calculated and experimental energies of GSB and NPB of ^{130}Xe-^{130}Nd are shown in Table 4. It is obvious that the calculated energy levels are in good agreement with the experimental ones for all isobars and for all states and the calculation of IBM-1 and IVBM is more reliable than that of BM and D-G for the calculation of the first two excited states, especially for ^{130}Xe and ^{130}Ba nuclei, with a deviation of calculation from IVBM for the first excited state of ^{130}Nd. So, the IBM-1 calculation is the most suitable one in this work.

TABLE 2. BM, IBM-1, IVBM and D-G parameters of GSB in keV for ^{130}Xe-^{130}Nd isobars

Isobar	BM			IBM-1						IVBM		D-G		
	A	B	C* 10^{-3}	No. of bosons	ε	*K1*	*K2*	*K4*	*K5*	β	γ	A	C* 10^{-2}	D* 10^{-1}
^{130}Xe	53.9	0.28	0.6	5	487.9	11.7	---	8.4	-1.2	3.8	274.9	89.4	-0.5	0.3
^{130}Ba	47.9	0.25	0.8	7	---	---	---	126.8	-16.6	15.06	158.5	59.6	-1.9	0.52
^{130}Ce	38.9	0.19	0.7	9	---	---	---	79.6	-3.1	16.8	99.5	42.3	-4.5	1.32
^{130}Nd	24.2	0.05	0.1	11	---	---	-0.37	110.7	-19.5	11.6	77.4	26.6	-2.8	1.47

TABLE 3. BM and IVBM parameters of NPB in keV for ^{130}Xe-^{130}Nd isobars

Isobar	BM			IVBM	
	A	$B*10^{-2}$	$C*10^{-2}$	η	ξ
^{130}Xe	5.9	-6.5	-0.01	-34.77	633.9
^{130}Ba	5.65	-10.08	-0.03	-171.7	1806.3
^{130}Ce	11.3	-5.07	-0.01	-101.3	1806.4
^{130}Nd	10.97	-4.5	-0.01	-3.0	1418.4

TABLE 4. The experimental [25] and calculated energy levels in keV of GSB and NPB for ^{130}Xe-^{130}Nd isobars

Isobar															
	I_1^{π}		2_1^+	3_1^-	4_1^+	5_1^-	6_1^+	7_1^-	8_1^+	9_1^-	10_1^+	11_1^-	12_1^+	13_1^-	14_1^+
^{130}Xe	$E_{\exp.}$		536	---	1205	2060	1944	2375	2697	3072	2972	3893	3693	4540	4591
	$E_{cal.}$	BM	313	---	969	2292	1808	2571	2633	3017	3292	3648	3772	4433	4334
		IBM-1	573	---	1176	---	1809	---	2473	---	3167	---	3892	---	4647
		IVBM	573	---	1167	1949	1809	2528	2473	3137	3167	3777	3892	4447	4647
		D-G	456	---	1157	---	1840	---	2489	---	3148	---	3851	---	4622
^{130}Ba	$E_{\exp.}$		357	1949	902	2168	1593	2568	2395	3067	3260	3659	4222	4354	---
	$E_{cal.}$	BM	279	2030	864	2200	1623	2524	2425	3035	3230	3699	4229	4344	---
		IBM-1	407	---	935	---	1584	---	2352	---	3242	---	4251	---	---
		IVBM	407	1948	935	2192	1584	2557	2352	3043	3242	3649	4251	4376	---
		D-G	409	---	974	---	1600	---	2338	---	3221	---	4265	---	---
^{130}Ce	$E_{\exp.}$		254	1955	710	2313	1324	2761	2053	3320	2809	4027	…	…	…
	$E_{cal.}$	BM	227	2098	706	2337	1342	2724	2044	3287	2811	4026	---	---	---
		IBM-1	300	---	734	---	1302	---	2005	---	2842	---	---	---	---
		IVBM	300	2003	734	2301	1302	2734	2005	3302	2842	4004	---	---	---
		D-G	331	---	749	---	1287	---	1985	---	2858	---	---	---	---
^{130}Nd	$E_{\exp.}$		159	1825	486	2144	940	2587	1487	3133	2100	3765	2764	4463	3468
	$E_{cal.}$	BM	143	1963	463	2191	927	2558	1493	3082	2117	3753	2769	4509	3451
		IBM-1	124	---	516	---	972	---	1494	---	2082	---	2735	---	3454
		IVBM	224.3	1802	541.3	2163	951	2608	1454	3136	2049	3749	2737	4446	3517
		D-G	306	---	621	---	982	---	1433	---	1991	---	2659	---	3440

4. Conclusions

The measured values of the first excited states $E2_1^+$ and the ratios of the second to the first excited states $E4_1^+/E2_1^+$ as well as the E-GOS, the ratio $r\left(\frac{(I+2)}{I}\right)$ and the staggering curves have been applied for describing GSB and NPB for ^{130}Xe-^{130}Nd isobars. These studies insured that ^{130}Xe nucleus is lined up along the U(5) side, ^{130}Ba and ^{130}Ce have an O(6) property, whereas ^{130}Nd has an O(6)-SU(3) property. It has been demonstrated that the GSB and NPB in the studied isobars exhibit $\Delta I = 1$ staggering. The vanishing value of the staggering $\Delta E_{1,\gamma}(I)=0$ has not been reached, which means that each nucleus is stable in its property. The BM, IBM-1, IVBM and D-G formula have been applied for calculating energy levels of GSB and NPB using the BM and IVBM models. The calculated energy levels in comparison with the experimental data indicate the quality of the fit presented in this work. It can be concluded that the IBM-1 calculation is the most suitable one in this work.

References

[1] Iachello, F. and Talmi, I., Rev. Mod. Phys., 59 (1987) 339.

[2] Greiner, W. and Maruhn, J.A., "Nuclear Models", (Springer Verlag Heidelberg, 1996) 375.

[3] Bohr, A. and Mottelson, B.R., "Nuclear Structure", (World Scientific Publishing), II (1998) 748.

[4] Raymond, K.S. and Sood, P.C., Phys. Rev. C, 34 (1986) 2362.

[5] Phillips, W.R. *et. al.*, Phys. Rev. Lett., 57 (1986) 3257.

[6] Bonatsos, D. *et al.*, Phys. Rev. C, 62 (2000) 024301-12.

[7] Ganev, H. *et al.*, Phys. Rev. C, 69 (2004) 014305-7.

[8] Krane, K.S., "Introductory Nuclear Physics", (John Wiley and Sons, 1987).

[9] Regan, P.H. *et al.*, Phys. Rev. Lett., 90 (2003) 152502.

[10] Bonatsos, D. and Skoures, L.D., Phys. Rev. C, 43 (1991) 952R.

[11] Khalaf, A.M. and Ismail, A.M., Prog. Phys., 2 (2013) 98.

[12] Iachello, F. and Arima, A., "The Interacting Boson Model", (Cambridge, 1987).

[13] Iachello, F., Phys. Rev. Lett., 85 (2000) 17.

[14] Ganev, H., Garistov, V.P. and Georgieva, A.I., Phys. Rev. C, 69 (2004) 014305- 7.

[15] Doma, S.B. and El-Gendy, H.S., Inter. J. Mod. Phys. E, 21 (2012) 1250077.

[16] Servin, A., Heyde, K. and Jolie, J., Phys. Rev. C, 36(6) (1987).

[17] Von Brentano, P., Gelberg, A., Harissopulos, S. and Casten, R.F., Phys. Rev. C, 38(5) (1988).

[18] Bettemann, L., Fransen, C., Heinze, S., Jolie, J., Linnmann, A., Mucher, D., Rother, W., Ahn, T., Castin, A., Pietralla, N. and Luo, Y., Phys. Rev. C, 79 (2009) 034315.

[19] Eid, S.A. and Diab, S.M., Progress in Phys., 1 (2012).

[20] Scharff-Goldhaber, G. and Weneser, J., Phys. Rev., 98 (1955) 212.

[21] Bohr, A. and Mottelson, B.R., Mat. Phys. Med., 27 (1953).

[22] Scholten, O. *et al.*, Ann. Phys., 115 (1978) 325.

[23] Iachello, F., Abrahams, K., Allart, K. and Dieperink, A.E., "Nuclear Structure", (Plenum Press, New York, 1981).

[24] Iachello, F. and Aima, A., "The Interacting Boson Model", (Cambridge University Press, Cambridge, 1987).

[25] ENSDF, http:// www.nndc.bnl.gov/ensdf (Nuclear data sheet) (2009).

Volume 9, Number 2, 2016. pp. 103-108

Jordan Journal of Physics

ARTICLE

Robust High Resolution Fat-Water Separation in the Abdomen during Free-Breathing by Self-Gated 2D Radial TrueFISP Imaging

Riad S. Ababneh[a], **Thomas Benkert**[b] and **Felix A. Breuer**[b]

[a] *Physics Department, Yarmouk University, Irbid 21163, Jordan.*
[b] *Research Center of Magnetic Resonance, Würzburg, Bavaria, Germany.*

Received on: 20/3/2016; *Accepted on: 18/7/2016*

Abstract: Accurate high resolution fat-water separation in the abdomen is challenging due to respiratory motion. In this work, we propose a robust high resolution fat-water separation strategy in the abdomen during free breathing by employing radial sampling with a golden angle increment. To this end, a radial TrueFISP sequence was modified enabling the echo time TE to change from projection to projection, to force fat signals to behave in a conspicuous manner through time, so that they can be detected and separated from water signals through temporal processing. Thus, the center signal (DC) of each radial readout can then be used for respiratory gating, allowing the generation of multiple images at different TEs at multiple breathing states. Finally, any fat-water separation technique can be used to synthesize high resolution fat and water images at arbitrary breathing states. Good separation of fat and water signals was achieved using the radial TrueFISP sequence during free breathing without streaking artifacts or blurring due to respiratory motion.

Keywords: Fat-water separation; TrueFISP; Self-gating; Dynamic imaging; Free breathing.

Introduction

Invivo, Magnetic Resonance (MR) images usually contain both fat and water signals, which differ slightly in frequency, making it possible to generate images where these two types of tissues are separated [10]. In applications where fat tends to obscure the pathology, or where the disease itself has to do with adipose tissues, such ability can prove very valuable.

Fat water separation with free breathing is challenging due to motion artifacts. There are several methods to avoid the anatomy motion artifacts, such as breath holding, where this method requires patient cooperation, but is limited in use, because many patients have difficulty performing the necessary breath-holds [11, 12, 16]. Another method is respiratory self-gating [1-3], which uses the DC-signal in the central k-space. The DC-signal is induced by changes of spin density in the excited slice and formed by sampling the center of k-space repeatedly over time [4]. The self-gating technique is used with many applications like 2D and 3D Cartesian sequences [4-6] as well as radial ones [7, 8].

For abdominal imaging applications, several MRI techniques have been used for fat-water separation. These include the Dixon method [9.10], direct phase encoding (DPE) [11] and iterative decomposition of water and fat with echo asymmetry and least-square estimation (IDEAL) [12]. Respiratory motion can lead to image quality deterioration and inaccurate measurements, such as ghosting and blurring artifacts in the reconstructed data. While breath holding removes respiratory motion artifacts, at the same time it limits spatial resolution [13, 14]. Alternatively, free breathing abdominal imaging could be combined with the methods proposed to avoid respiratory motion artifacts, while continuing to provide a good temporal and

Corresponding Author: Riad S. Ababneh **Email**: riada@yu.edu.jo

spatial resolution. Therefore, established strategies for fat-water separation with free breathing are quite capable of separating fat and water signals, and require at least three images for the separation to be performed, making it difficult to achieve good temporal resolution in dynamic imaging [9-12]. In contrast, Ababneh *et al*. [16] succeeded in separating fat and water signals in dynamic MRI and provided improved temporal resolution by the combined three-point Dixon method for fat-water separation and Unaliasing by Fourier-encoding the overlaps using the temporal dimension (UNFOLD) [16, 17]. This method involves an assumption that fat signals are not very dynamic. Even when fat signals prove to be quite dynamic, suppressing their low temporal frequency content is expected to lead to significant overall suppression. The method provided a unique combination of imaging speed, high signal-to-noise ratio (SNR) and high contrast between myocardium and blood pool. In this work, fat-water separation method in [15] was combined with self-gating technique and used with free breathing in the abdomen. Therefore, a regular 2D radial TrueFISP sequence was modified to allow TE to vary from projection to the next. TE was adjusted here in a predetermined manner, to force fat signals to behave in a peculiar and readily recognizable fashion over time. Using temporal processing, the temporal variations imposed on fat signals can be recognized and fat signals can be separated from water signals.

Radial k-space trajectories became a part of this work, because they are suitable for dynamic imaging and have been used in many applications, such as cardiac imaging [18-21] and abdominal imaging [22, 23]. Radial MRI has a higher sampling density for the central k-space and higher spatial and temporal resolution and is insensitive to object motion during data acquisition [24, 25].

In the present work, we aimed to separate fat and water signals during free breathing abdominal imaging. Therefore, we integrated the fat-water separation method [15] with the self-gating technique while at the same time modifying the 2D radial TrueFISP sequence. Results were obtained *invivo* at 3T for the abdomen.

Materials and Methods

Healthy volunteers participated in the study following the guidelines of the local institutional review board, including written informed consent. This work uses the 2D radial TrueFISP sequence, characterized by a train of alternating excitation pulses (±α), separated by a constant time interval (repetition time TR). It starts with a number of dummy RF pulses to hasten the set-up of a steady state magnetization. The pulse sequences were modified to enable TE variations from one projection to the next, using the TE(t) pattern as in Fig. 1a. To achieve fat and water separation, the 2D radial TrueFISP pulse sequence was modified to make the echo time vary from one projection to the next as in Fig.1b for subsequent radial projections at constant TR [15]. A sequence of 4 TEs was periodically repeated following a radial golden angle projection order φ_{GR}=111.246°. Four images with different contrast were generated using DC gating technique for each data set. The coil channel providing the highest sensitivity towards respiratory motion was selected manually and gating windows were derived from the DC signal (Fig. 2). In this work, the width of the gating windows has been selected by choosing a constant number of projections. The signals within each gating window were used to generate images at different TEs using non-uniform fast Fourier transform (NUFFT) gridding [26]. In total, 2001 projections were acquired, where each window included 631 radial projections. Finally, the application of appropriate filters to the image series allows one to discriminate fat and water as described in Ref. [15]. The imaging parameters were: TR = 4.0 ms, (TE_1 = 1.6 ms, TE_2 = 2 ms, TE_3 = 2.4 ms), matrix size = 256 x 256, flip angle = 40°, FOV= 400x400 mm^2, slice thickness = 5 mm and resolution=1.56 x 1.56.

All data from self-gating scan was reconstructed offline using a MatLab software package (Math Works, Natick, MA). In this work, we integrate the fat-water separation method used in [15] with self-gating 2D radial technique during free breathing abdominal imaging. Results were obtained *invivo* at 3T for the abdomen.

In this study, the center signal (DC) of each radial readout used for respiratory gating allows the generation of multiple images at different TEs in multiple breathing states.

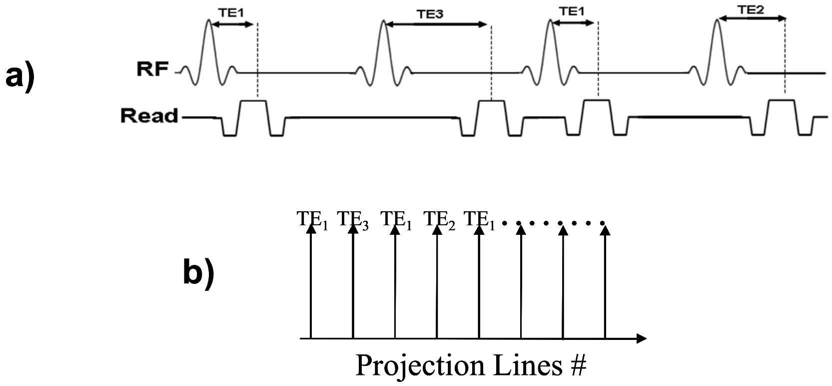

FIG. 1. a. The modified TrueFISP sequence. b. The acquired projections with different echo times are spaced by an angle increment of 111.246º.

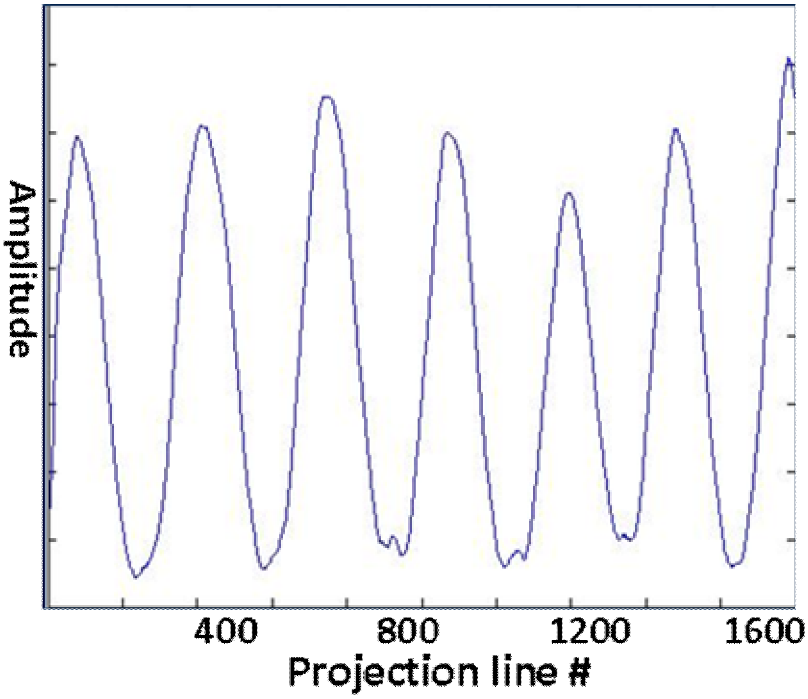

FIG. 2. The self-gating signal *vs*. the projection number from the coil channel number 15.

Results

Experiments were performed on a 3T system (Siemens, Erlangen, Germany) using a 32 spinal coil positioned about the mid portion of the body and body array. Fig. 2 shows the self-gating signal *vs*. the projection number from the coil channel number 15, which is selected manually, because it provides the highest sensitivity toward the respiratory motion. The two parallel lines indicate the chosen window for respiratory gating. Fig. 1 shows the modified sequence, where TE changes from projection to projection (Fig. 1b). As shown in Fig. 1a, TE (t) takes on the successive values of TEs, where TE1 = TE_o, TE2 = $TE_o + \Delta TE$ and TE3 = $TE_o + 2\Delta TE$. TE_o is the shortest possible echo time allowed by the unmodified sequence and ΔTE is the echo time increment. The echo time increment ΔTE was kept extremely short in this work (~ 400 µs). In comparison, in the original description of the three-point Dixon method [10], ΔTE would be the value required for an 180^o offset between the fat and water signals. This choice of a short 400 µs ΔTE stems from the need to keep TE and TR short in a TrueFISP sequence.

Fig. 3 shows the calculated water and fat in a healthy volunteer acquired under free breathing conditions, the calculated water (a and b) and fat (c and d), where a and c images represent the inspiration state and b and d images represent the expiration state. Fig. 4 is for another volunteer, where Fig. 4a shows the water image and Fig. 4b shows the fat image. The water-only and fat-only images were obtained using the algorithm proposed in [15]. Banding artifacts, common with TrueFISP sequences, were observed. The white arrow indicates banding artifacts in Fig. 3a.

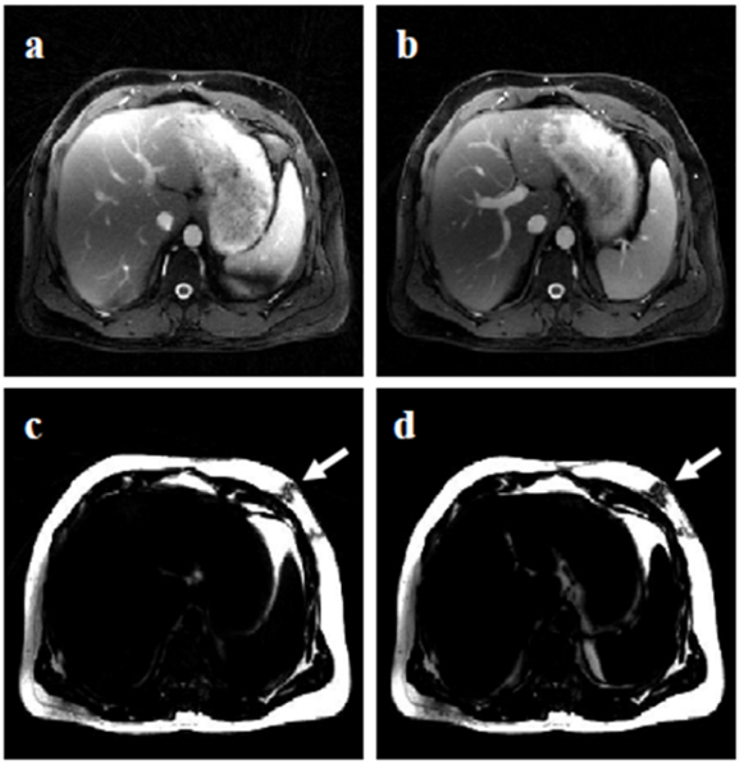

FIG. 3. One phase acquired at 3T in a healthy volunteer is shown here, (a) and (b). Water-only and fat-only results are shown in (c) and (d), respectively.

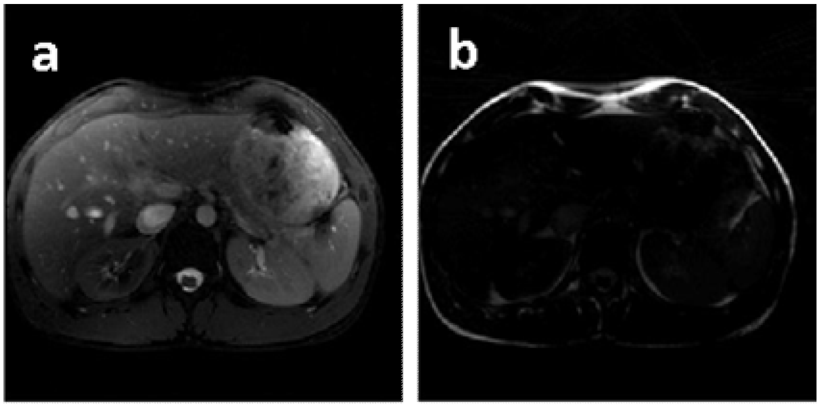

FIG. 4. One phase acquired at 3T for a different healthy volunteer is shown here. (a) Water-only, (b) fat-only.

Discussion

A novel approach to separate fat and water signals in the abdomen combined with self-gating radial TrueFISP is presented here. This approach provides good fat-water separation, reduces blurring artifacts caused by respiratory motion and enhances the image resolution. The self-gating method was successfully used to track respiratory motion. Therefore, fat-water separation is achieved in all breathing stages. Fig. 1 shows the accepted data for expiration and inspiration used for reconstruction, where 631 radial projections out of 2001 were used for each window. By comparing the DC-signal variations from all coils used in the scan, coil number 15 was selected manually, because it provided the highest sensitivity towards respiratory motion.

The selected number of projections for reconstruction takes into account the trade-off between better SNR and enhanced image resolution. Therefore, despite using a partial part of the acquired data (631 projections out of 2001), it was sufficient to achieve these goals.

The 2D radial TrueFISP sequence was modified by changing the echo time TE from projection to projection, to force fat signals to behave in a conspicuous manner through time, so that they can be detected and separated from water signals through temporal processing. The echo time increment ΔTE should be large enough to induce large phase differences between fat and water signals, yet small enough to avoid undue increases in TR in our TrueFISP sequence. A value of ΔTE = 400 μs was considered as an acceptable compromise between these two conflicting demands.

The present method is aimed at clinical applications, where good temporal resolution and good fat suppression are both crucial. While the concept has been demonstrated in 2D, future work will be targeted on extending the method to self-gated 3D radial imaging for robust fat-water separation in the abdomen. Further, the approach might prove to be particularly useful in contrast-enhanced breast imaging, where bright fat signals tend to obscure lesion-related water signals and where good temporal resolution is important to accurately capture dynamic signal enhancement.

The TrueFISP pulse sequence is sensitive to off-resonance effects, leading to banding artifacts. These artifacts result whenever off-resonance reaches a value equal to $\pm\frac{1}{2TR}$, which indicates the allowed range for banding-free imaging. The banding artifact shown in Fig. 3 was generated while using TR = 4.0 ms. The results of our study show that TrueFISP with radial acquisition during free-breathing is feasible for abdominal MRI studies and shows that even small variations in TE (0.4 ms) were sufficient to separate fat and water in dynamic objects.

Conclusion

This approach was tested in time resolved abdominal imaging. Good separation without streaking artifacts or blurring due to respiratory motion was obtained in all studied cases. The separation for free breathing was accomplished by incorporating the modified 2D radial TrueFISP sequence with self-gating technique. Self-gating reduces blurring artifacts caused by respiratory motion and enhances the image resolution.

Acknowledgements

The author are very thankful to the Deutsche Forschungsgemeinschaft DFG BR (4356/2-1) for funding and to SIEMENS, Healthcare Sector, Erlangen, Germany for technical support.

References

[1] Stehning, C., Bornert, P., Nehrke, K., Eggers, H. and Stuber, M., Magn. Reson. Med., 54 (2005) 476.

[2] Lai, P., Larson, A.C., Bi, X., Jerecic, R. and Li, D., J. Magn. Reson. Imaging, 28 (2008) 612.

[3] Lai, P., Larson, A.C., Park, J., Carr, J.C. and Li, D., Magn. Reson. Med., 59 (2008) 1378.

[4] Stefan, W., Felix, B., Philipp, E., Michael, V., Christian, H., Jurgen, B. and Peter, J., J. Magn. Reson. Imaging, 37 (2013) 727.

[5] Crowe, M.E., Larson, A.C., Zhang, Q. et al., Magn. Reson. Med., 52 (2004) 782.

[6] Brau, A.C.S. and Brittain, J.H., Magn. Reson. Med. 55 (2006) 263.

[7] Larson, A.C., White, R.D., Laub, G. et al., Magn. Reson. Med., 51 (2004) 93.

[8] Jing, L., Pascal, S., Noel, C., Thanh, N., Martin, P. and Yi, W., Magn. Reson. Med., 63(5) (2010) 1230.

[9] Farrelly, C., Shah, S., Davarpanah, A., Aoife, N., Keeling, C. and James, C., American Journal of Roentgenology, 199(1) (2012).

[10] Dixon, W.T., Radiology, 153 (1984) 189.

[11] Glover, G.H. and Schneider, E., Magn. Reson. Med., 18 (1991) 371.

[12] Xiang, Q.S. and An, L., J. Magn. Reson. Imaging, 7 (1997) 1002.

[13] Reeder, S.B., Wen, Z., Yu, H. et al., Magn. Reson. Med. 51 (2004) 35.

[14] Ning, B.S., Robert, J.L., Omary, R.A. and Larson, A.C., J. Magn. Reson. Imaging, 29 (2009) 860.

[15] Tang, C., Blatter, D.D. and Parker, D.L., J. Magn. Reson. Imaging, 3 (1993) 377.

[16] Ababneh, R., Yuan, J. and Madore, B., J. Magn. Reson. Imaging, 32 (2010) 962.

[17] Madore, B., Glover, G.H. and Pelc, N.J., Magn. Reson. Med., 42 (1999) 813.

[18] Madore, B., Hoge, W.S. and Kwong, R., Magn. Reson. Med., 55 (2006) 352.

[19] Larson, A.C. and Simonetti, O.P., Magn. Reson. Med., 46 (2001) 1059.

[20] Schaeffter, R., Weiss, S., Eggers, H. and Rasche, V., Magn. Reson. Med., 46 (2001) 1238.

[21] Peters, D.C., Epstein, F.H. and McVeigh, E.R., Magn. Reson. Med., 45 (2001) 562.

[22] Barger, A.V., Grist, R.M., Block, W.F. and Mistretta, C.A., Magn. Reson. Med., 44 (2000) 821.

[23] Glover, G.H. and Pauly, J.M., Magn. Reson. Med., 28 (1992) 275.

[24] Altbach, M.I., Outwater, E.K., Trouard, T.P., Krupinski, E.A., Theilmann, R.J., Stopeck, A.T., Kono, M. and Gmitro, A.F., J. Magn. Reson. Imaging, 16 (2002) 179.

[25] Katoh, M., Spuentrup, E., Buecker, A., Manning, W.J., Guenther, R.W. and Botnar, R.M., J. Magn. Reson. Imaging, 23 (2006) 757.

[26] Fessler, J.A. and Sutton, B.P., IEEE Trans. Med. Imaging, 51 (2003) 560.

Volume 9, Number 2, 2016. pp. 109-112

Jordan Journal of Physics

ARTICLE

Evaluation of Annual Effective Dose Due to Ingestion in Some Commonly Consumed Vegetables in Lagos State, Nigeria

M. A. Olaoye[a], **T. J. Aluko**[b], **J. A. RABIU**[c], **O. A. Jegede**[b] and **O. O. Adeleke**[b]

[a] *Department of Physics, Lagos State University, Ojo Lagos State, P.M.B. 101001, Ojo Lagos, 101001, Nigeria.*

[b] *Department of Physics, Federal University of Agriculture, Abeokuta Ogun State, P.M.B. 2240, Abeokuta, 110001,Nigeria.*

[c] *Department of Physics, Federal University, Kashere Gombe State, P.M.B. 0182, Kashere, 740001, Nigeria.*

Received on: 2/6/2016; Accepted on: 23/10/2016

Abstract: The activity concentrations of ^{40}K, ^{238}U and ^{232}Th in some commonly consumed vegetables in Badagry, Ikorodu and Ojo areas of Lagos state were determined. The highest concentration of ^{40}K was obtained in *Celosia argentea* (Lagos Spinach) with a value of 7807.51±402.48 Bq/kg, the highest concentration of ^{238}U with a value of 59.46±6.46 Bq/kg was found in *Amaranthus hybridus* (African Spinach) and the highest concentration of ^{232}Th was found in *Amaranthus hybridus* (African Spinach) with a value of 47.45± 2.80 Bq/kg. The highest concentrations were found in vegetables from Ikorodu. The lowest concentration of ^{40}K was found in *Hibiscus sabdariffa* (Roselle) with a value of 451.23±23.87 Bq/kg. *Celosia argentea* (Lagos Spinach) has the lowest concentration value of 0.79±0.10 Bq/kg for ^{238}U and a concentration value of 3.81± 0.22 Bq/kg was found in *Vernonia amygdalina* (Bitter Leaf) being the lowest concentration value of ^{232}Th. The mean annual effective doses of Badagry, Ikorodu and Ojo were 1.42mSv/y, 2.06mSv/y and 2.23mSv/y, respectively, which were higher than the world mean average of 0.294mSv/y.

Keywords: Activity concentration; Vegetables; Mean absorbed dose; Cancer risk.

Introduction

Radionuclides are found naturally in air, water and soil. They are even found in human beings. We are products of our environment, and we interact daily with radionuclides in the environment through ingestion and inhalation. [1, 2]

The level of terrestrial background radiation of radionuclides depends on the geological and geographical location which differs on regional bases [3, 4].Weathering and erosion of rocks (igneous and metamorphic) into sand, deposit minerals bearing natural radionuclides. These radionuclides are transmitted along with nutrients during mineral uptake through absorption and are accumulated in edible and non-edible parts of plants [5]. According to IAEA report [6], soil vegetables are recognized among the main path radionuclides transferred to man. Several studies have been performed in different countries to determine the radionuclides' concentrations in different food samples and dose assessment from food staff consumption by the populace [7-11].

Vegetables and fruits are important components of a healthy diet and the presence of the natural radionuclides ^{40}K, ^{238}U and ^{232}Th in them has certain radiological implications; not only on the foods, but on the consuming population [1, 12- 13].

In this study, activity concentrations of ^{40}K, ^{238}U and ^{232}Th are investigated in some common vegetables (*Corchorous olitorious*, *Vernonia*

Corresponding Author: T. J. Aluko **Email**: alukotywo@gmail.com

amygdalina, *Talium triagulare*, *Celosia argentea*, *Amaranthus hybridus*, *Telfaina occidentalise*) from Badagry, Ikorodu and Ojo areas of Lagos state, Nigeria. This study will provide a baseline data on radionuclides' concentrations in vegetables from these areas for further research.

Materials and Method

Commonly consumed vegetables were presented by the populace in the selected areas. The selection was such that six commonly consumed vegetables were collected from Badagry, Ikorodu and Ojo, respectively in the course of this study. These specimens (Veggies) were collected from local farmers. Measurements of the dry weight of the edible part (leaves) were used [6]. The vegetables were hand-cleaned to remove soil particles as to avoid contamination, then washed with tap water. The samples were air-dried for 10 days, oven-dried at 80°C in order to remove moisture and blended to powder. These were packed in 0.2kg lots by weight W_3 and airtight sealed in a white cylindrical PVC container.

$$W_3 = W_2 - W_1 . \quad (1)$$

W_3 is the weight of the dry sample, W_2 is the weight of the PVC container and sample together and W_1 is the weight of the PVC container.

The samples were left for 4 weeks, so that the secular equilibrium of the gaseous daughters of Uranium and Thorium series would be attained before counting. A high confident background level was established by measuring background radiation with an empty container for 10 hours. The activity concentrations of the samples were determined using the formula in Eq. 2.

$$C_{samp} = [C_{std} \times W_{std} \times N_{samp}] / [W_{samp} \times N_{std}] . \quad (2)$$

C_{samp} and C_{std} represent the activity concentrations of the sample and the standard sample, respectively. W_{samp} and W_{std} are the weights of the sample and the standard sample, while N_{samp} and N_{std} are the net counts of the photo peak area of the sample and the standard sample.

Radioactivity counting in this work was carried out using a lead shielded 76mm X 76mm NaI (TI) crystal detector (Model Number: 802 Series) by Canberra Inc., which is coupled to a Canberra series plus 10 Multi- Channel Analyzer (MCA) (Model number 1104) through a preamplifier base. The detector used has a resolution of about 8% at 0.662MeV line of ^{137}Cs for the measurement of ^{40}K, ^{238}U and ^{232}Th concentrations. Photo peak regions of (1.460MeV) ^{40}K, (1.76MeV) ^{214}Bi and (2.615MeV) ^{208}TI were used, respectively. Each sample E1- E7 in Table 1 was counted for 36,000 seconds for each study area using the same technique as in the background radiation.

TABLE 1. List of vegetables used in the study and their code names

S/N	Vegetable code	Vegetable name	Vegetable traditional name	Botanical name of the vegetable
1	E1	Jute Leaves	Ewedu	*Corchorous olitorious*
2	E2	Bitter Leaf	Ewuro	*Vernonia amygdalina*
3	E3	Water Leaf	Gbure	*Talinium triangulare*
4	E4	Lagos Spinach	Shoko Yokoto	*Celosia argentia*
5	E5	African Spinach	Efo Tete	*Amaranthus hybridus*
6	E6	Fluted Pumpkin Leaf	Ugu	*Telifairia occidentalis*
7	E7	Roselle	Ishapa	*Hibiscus sabdariffa*

Results and Discussion

The value and the associated tolerance (±) in the concentration of ^{40}K, ^{238}U and ^{232}Th were measured in vegetable samples in Badagry. As shown in Table 2, the activity concentration of ^{40}K ranges from 451.23 ± 23.87 Bq/kg to 5835.84 ± 309.12 Bq/kg, with the lowest concentration in Roselle (*Hibiscus sabdariffa*) and the highest concentration in Water Leaf (*Talium triagulane*). The activity concentration of ^{238}U ranges from ND to 39.80 ± 4.27 Bq/kg, with the highest concentration in Jute Leaves (*Corchorous olitorious*), while the activity concentration of ^{232}Th ranges from ND in Water Leaf (*Talium triangulane*) and Roselle (*Hibiscus sabdariffa*) to 35.83 ± 2.11 Bq/kg in Fluted Pumpkin Leaf (*Telfairia occidentalis*). The activity concentration values of ^{40}K, ^{238}U and ^{232}Th measured in Ikorodu are shown in Table 3. The activity concentration of ^{40}K ranges from 1269.75 ± 66.89 Bq/kg to 7807.51 ± 402.48

Bq/kg, with the lowest concentration in Jute Leaves (*Corchorous olitorious*) and the highest in Lagos Spinach (*Celosia argentea*). The activity of ^{238}U ranges from 15.21 ± 1.86 Bq/kg to 59.46 ± 6.46 Bq/kg, with the lowest concentration in Jute Leaves (*Corchorous olitorious*) and the highest concentration in African Spinach (*Amaranthus hybridus*). The activity concentration of ^{232}Th ranges from ND in Jute Leaves (*Corchorous olitorious*) to 47.45 ± 2.80 Bq/kg with the highest concentration in African Spinach (*Amaranthus hybridus*).

TABLE 2. Radioactivity concentration in vegetables in Badagry, Lagos

SAMPLES	^{40}K (Bqkg^{-1})	^{238}U (Bqkg^{-1})	^{232}Th (Bqkg^{-1})
E_1	4622.37 ± 238.83	39.80 ± 4.27	11.83±0.70
E2	2339.12 ± 122.34	25.31 ± 2.85	26.23±1.55
E3	5835.84 ± 309.12	ND	ND
E4	3376.06 ± 176.00	0.79 ± 0.10	6.20±0.37
E6	2539.33 ± 131.97	35.73 ± 3.88	35.83±2.11
E7	451.23 ± 23.87	6.79 ± 1.16	ND
WEIGHTED MEAN	3193.77 ± 167.02	18.07 ± 2.04	13.35 ± 0.79

TABLE 3. Radioactivity concentration in vegetables in Ikorodu, Lagos

SAMPLES	^{40}K (Bqkg^{-1})	^{238}U (Bqkg^{-1})	^{232}Th (Bqkg^{-1})
E1	1269 ± 66.89	15.21 ± 1.86	ND
E2	4036.57±209.16	18.99 ± 2.31	18.71± 1.11
E3	6637.95±344.13	41.96 ±5.00	17.50 ± 1.05
E4	7807.51±402.48	43.51 ±4.63	14.32 ± 0.85
E5	3007.58±156.47	59.46 ± 6.46	47.45 ± 2.80
E6	4524.65±234.34	32.20 ± 3.57	22.26 ± 1.32
WEIGHTED MEAN	4547.25±235.58	35.22 ± 3.97	20.04 ± 1.19

The activity concentration values of ^{40}K, ^{238}U and ^{232}Th measured in Ojo are shown in Table 4. The activity concentration of ^{40}K ranges from 608.07 ± 32.05 Bq/kg to 7320.47 ± 378.06 Bq/kg, with the lowest concentration in Fluted Pumpkin Leaf (*Telfairia occidentalis*) and the highest in Water Leaf (*Talium triangulane*). The activity concentration of ^{238}U ranges from 9.75 ± 1.23 Bq/kg to 57.70 ± 6.19 Bq/kg, with the lowest concentration in Bitter Leaf (*Vernonia amygdalina*) and the highest concentration in Lagos Spinach (*Celosia argentea*). The activity concentration of ^{232}Th ranges from 3.81 ± 0.22 Bq/kg to 43.65 ± 2.58 Bq/kg, with the lowest concentration in Bitter Leaf (*Vernonia amygdalina*) and the highest concentration in Lagos Spinach (*Celosia argentea*). The errors show the spatial variation within the samples and the weighted mean represents the average mean of each radionuclide in all vegetables in each study area.

Table 4: Radioactivity concentration in vegetables of Ojo, Lagos

SAMPLES	^{40}K (Bqkg^{-1})	^{238}U (Bqkg^{-1})	^{232}Th (Bqkg^{-1})
E1	6078.93 ± 314.09	18.85 ± 2.33	27.29 ±1.62
E2	4873.07 ± 250.54	9.75 ± 1.23	3.81 ± 0.22
E3	7320.47 ± 378.06	26.14 ± 3.31	33.36 ± 1.98
E4	4927.90 ± 255.10	57.70 ± 6.19	43.65 ± 2.58
E5	4951.89 ± 255.50	35.73 ± 3.88	35.83 ± 2.11
E6	608.07 ± 32.05	13.04 ± 1.91	19.24 ± 1.16
WEIGHTED MEAN	4793.38 ± 247.55	26.87 ± 3.14	27.19 ± 1.61

The doses received by a person consuming aquatic food stuff depends on the radionuclide concentration in the food and the quantity taken [1]. The effective dose equivalent by ingestion of nuclides was calculated using Eq. 3.

$$\text{Ingested dose} = \text{Concentration of radionuclides} \times \text{Annual intake per year} \times \text{DCF}\ ; \quad (3)$$

where DCF is the dose conversion factor and the annual intake of vegetables per year of an adult is 60 kg/y [4].

The mean annual effective dose values of Badagry, Ikorodu and Ojo were 1.42mSv/y, 2.06mSv/y and 2.23mSv/y, respectively, which were higher than the world mean value of 0.29mSv/y [4]. The annual collective effective dose equivalent was obtained using Eq. 4 [14].

$$S_e = H_i \times N\,(H)_i\,; \qquad (4)$$

where S_e is the collective effective dose equivalent, H_i is the average annual effective dose equivalent and $N\,(H)_i$ is the number of individuals in the population of the study area. The populations of Badagry, Ikorodu and Ojo are 237,731, 527,971 and 609,173 [15], which translate to a collective dose equivalent of 0.34×10^3 manSv/y, 1.09×10^3 manSv/y and 1.36×10^3 manSv/y.

Excess Lifetime Cancer Risk (ELCR) is calculated using Eq. 5 below.

$$ELCR = AEDE \times DL \times RF\,; \qquad (5)$$

where AEDE, DL and RF are the annual effective dose equivalent, duration of life and risk factor (S/v) of fatal cancer risk per Sievert for stochastic effects. ICRP 60 uses a value of 0.05 for the public [3]. A life time duration of 50 years is used. The calculated ELCR values are 0.36×10^{-3}, 0.52×10^{-3} and 0.56×10^{-3} for Badagry, Ikorodu and Ojo, respectively which are higher than the world average value of 0.29×10^{-3}. This indicates that the possibility of developing cancer cases among residents cannot be neglected.

Conclusion

The method of gamma spectrometry has been used to determine the nuclide concentration in commonly consumed vegetable samples in Badagry, Ikorodu and Ojo. The mean effective dose was also determined to assess the implication on consumer health. High concentrations of ^{40}K in all samples are due to the constant use of inorganic (N:P:K) fertilizers by farmers which are deposited in the edible parts of plants and are reflected in the high values of effective dose from ingestion of terrestrial radioisotopes and ELCR. The mean annual effective dose equivalent values for consumption of these vegetables are higher than the world mean dose equivalent of 0.29mSv/y [4]. Data from this study can serve as a reference for further studies.

References

[1] Eyebiokin, M.R., Arogunjo, A.M., Oboh, G., Balogun, F.A. and Rabiu, A.B., Nigeria Journal of Physics, 17S (2005) 187.

[2] Olomo, J.B., Nucl. Inst. and Methods in Phys. Res. A, 299 (1990) 666.

[3] Maniganadan, P.K. and Chandar Shekar, B., Journal of Radiation Research and Applied Sciences, 7 (2014) 310.

[4] UNSCEAR, United Nations Scientific Committee on the Effects of Atomic Radiation, Sources and Effects of Ionizing Radiation, United Nations, (New York, 2000).

[5] Islam, A., Begum, A., Yeasmin, S. and Sultana, M.S., International Journal of Radiation Research, 12(3) (2014).

[6] IAEA, Measurement of Radionuclides in Food and Environment, IAEA Technical Report Series No. 295, (Vienna; IAEA,1989).

[7] Al-Ghamdi, A.H., Journal of American Science, 10(11) (2015) 164.

[8] James, J.P., Dileep, B.N., Mulla, R.M., Joshi, R.M., Vishnu, M.S., Nayak, P.D., Ravi, P.M. and Sarkar, P.K., Radiation Protection Dosimetry, 153(1) (2013) 56.

[9] Awudu, A.R., Faanu, A., Darko, E.O., Emi-Reynolds, G., Adukpo, O.K., Kpeglo, D.O., Otoo, F., Lawluvi, H., Kpodzro, R., Ali, I.D., Obeng, M.K. and Agyeman, B., J. Radioanal Nucl. Chem., 291 (2012) 635.

[10] Nasreddine, L., El-Samad, N., Hwalla, N., Baydoun, R., Hamze, M. and Parent-Massin, D., Radiation Protection Dosimetry, 131(4) (2008) 545.

[11] Hosseini, T., Fathivand, A.A., Abbasisiar, F., Karimi, M. and Barati, H., Radiation Protection Dosimetry, 121(3) (2006) 236.

[12] Awviri, G.O., Osarolube, E. and Alao, A.A., International Journal of Scientific Research, 2(2) (2013).

[13] Fortunati, P., Brambilla, M., Speroni, F. and Carini, F., Journal of Environmental Radioactivity, 71 (2004) 187.

[14] ICRP, Recommendation of the International Commission on Radiological Protection, Pergamon (1994).

[15] NPC, National Population Commission (2006).

Volume 9, Number 2, 2016. pp. 113-122

Jordan Journal of Physics

ARTICLE

Effects of Thermal Annealing on Structural and Optical Properties of Nanocrystalline $Cd_xPb_{1-x}S$ Thin Films Prepared by CBD

S. M. Ahmad[a], **S. J. Kasim**[a] and **L. A. Latif**[b]

[a] *Physics Department, College of Science, University of Basra, Iraq.*
[b] *Physics Department, College of Science, University of Mustansyria, Iraq.*

Received on: 13/6/2016; Accepted on: 24/10/2016

Abstract: $Cd_xPb_{1-x}S$ thin films with (x=0, 0.4) were successfully deposited on glass substrates using chemical bath deposition (CBD) method. It was confirmed from the X-ray diffraction (XRD) analysis that all the films exhibited a polycrystalline nature with preferential orientation along (200) plane. The deposited films were thermally annealed in order to investigate the effect of thermal annealing on the structural and optical properties. From the XRD analysis, better crystallization was observed with increasing crystallite size as the annealing temperature was raised from (298 to 573) K, while optical absorption measurements showed that the allowed direct band gap of the annealed samples decreased from 1.59 to 1.55 eV and from 1.7 to 1.65 eV for PbS and $Cd_{0.4}Pb_{0.6}S$, respectively. The effect of thermal annealing on optical constants, such as extinction coefficient (k), refractive index (n),real and imaginary dielectric constants (ϵ_1,ϵ_2), was discussed. Each of the photo luminescence (PL) spectra revealed a single peak red emission around (680) nm for PbS and (670) nm for $Cd_{0.4}Pb_{0.6}S$.

Keywords: Optical properties; Thin films; CBD; Thermal annealing; XRD.
PACS: 79.60.Dp.

Introduction

A considerable attention was paid to the deposition of ternary derivative semiconductors due to the possibility of controlling the energy gap and lattice constant [1]. Lead sulfide is a member of an important narrow–band IV-VI compound semiconductor group, and is widely used as infrared sensor (due to it's 0.4 eV direct band gap) [2]. This material has also been utilized in many fields, such as photography [3]. There are several methods to prepare lead sulfide thin films, such as spray pyrolysis [4], photo-accelerated chemical deposition [5], microwave heating [6], electro deposition [7], photoelectro-chemical deposition using olive oil [8] and chemical bath deposition [9,10]. The last method is an easy, inexpensive and most energy efficient method and has been traditionally used in chalcogenide semiconductor thin film preparation [11]. The narrow band gap of PbS semiconductor can be modified by adding a molar ratio of a wide band gap compound, such as CdS (2.4) eV. Mixing thin films of PbS and CdS ($Cd_xPb_{1-x}S$) has attracted special attention, since they are promising in many physical applications, such as photo-electronics, optical switches, solar cells and infrared photo - detectors [13,14]; as their band gap could be adjusted to match the ideal band gap (~1.5 eV) needed to produce most efficient solar cells. $Cd_xPb_{1-x}S$ has been employed in several techniques, such as chemical vapor deposition [15], successive ionic layer reaction [16] and sol-gel method [17]. Many studies highlighted the electrical and optical properties of CdPbS [18-20]. In this paper, we reported the influence of thermal treatment on structural and optical properties of $Cd_xPb_{1-x}S$ (x = 0, 0.4) prepared by CBD. The resulting films have been characterized in terms of structural and optical properties using XRD and UV-VIS-NIR spectrophotometer techniques, respectively.

Corresponding Author: S. M. Ahmad **Email**: smahmood42@yahoo.com

Experimental Process

Specimens of PbS and $Cd_xPb_{1-x}S$ thin films were grown on ordinary glass slides (7.5x2.5 cm). Deposition was carried out in a reaction solution prepared in 100 ml beaker containing 0.1 M solution of lead acetate ($Pb(CH_3COO)_2$), 0.1 M of cadmium acetate ($Cd(CH_3COO)_2$), ammonia (NH_3) and 0.1M of thiourea ($(NH_2)_2SC$). Lead acetate acts as the source of cation (Pb^{+2}) as cadmium acetate (Cd^{+2}) does and thiourea was the source of anion (S^{-2}). NH_3 was used to maximize growth by providing an alkaline medium. The deposition of $Cd_xPb_{1-x}S$ thin films started with mixing lead acetate and cadmium acetate (x=0, x=0.4) with 1 ml NH_3. The solution was completed to 50 ml with distilled water, then heated up to 323 K. The glass substrates were immersed vertically and then 10 ml of thiourea was added gradually (drop by drop) and heated to 333 K in a bath. This temperature was kept constant for about 90 minutes, then the substrates were taken out, washed with distilled water and dried. The resulting films were homogeneous, well adhered to the substrate, with a mirror-like surface for PbS thin films and yellowish dark for $Cd_xPb_{1-x}S$ thin films. The average thickness of films estimated by weighing method was around 3000±10 Å. The CBD depends on sequential reactions at the surface of substrate. The formation of $Cd_xPb_{1-x}S$ may involve the following steps [21]:

$$Pb(CH_3COO)_{2-} \rightarrow Pb^{+2} + 2\,CH_3COO^-$$
$$Pb^{+2} + 4\,NH_3 \rightarrow Pb(NH_3)_4^{2+}$$
$$Cd(CH_3COO)_2 \rightarrow Cd^{+2} + 2\,CH_3COO^-$$
$$Cd^{+2} + 4\,NH_3 \rightarrow Cd(NH_3)_4^{2+}$$

In alkaline medium, dissociation of $(NH_2)_2SC$ takes place.

$$(NH_2)_2SC + OH \rightarrow CH_2N_2 + H_2O + SH^-$$
$$SH^- + OH \rightarrow S^{2-} + H_2O$$

The overall chemical reaction is as follows:

$$(1-x)[Pb(NH_3)_4]^{2+} + x[Cd(NH_3)_4]^{2+} + (NH_2)_2SC \xrightarrow{NH_4OH} Cd_xPb_{1-x}S + 6\,NH_3 + CO_3^{2-} + H_2O$$

A change has been noticed in the reaction solution color after heating, marking a chemical reaction that resulted in deposition of homogenous $Cd_xPb_{1-x}S$ films, formed within optimum conditions. After complete drying, the films were annealed in atmosphere at 473 K and 573 K for one hour. The structure of the films was characterized by X-ray diffraction (XRD) using Cu Kα radiation (λ =1.54 Å), where the average diameter (D) of grain size of $Cd_xPb_{1-x}S$ was calculated using Scherer formula [22]:

$$D = 0.9\lambda/\beta\cos\theta\ ;$$

where β is the experimentally observed diffraction peak width at full wave half maximum intensity (FWHM) and θ is Bragg angle. The strain ξ of the deposited films was obtained from the following relation [23]:

$$\cos\theta/\lambda = 1/D + \xi \sin\theta/\lambda\ \beta\ .$$

The grain size value can be used in the relation $\delta=1/D^2$ to obtain the value of dislocation which shows the amount of defect in the crystal as it appears in Table 1 and Table 2.

TABLE 1. Values of energy gap, grain size, dislocation and strain of PbS thin films

T°C	Eg eV	D nm	nm^{-2} ó	ξ
Without annealing	1.59	38	0.0006	0.018
200	1.57	45	0.0004	0.008
300	1.55	56	0.0003	0.007

TABLE 2. Values of energy gap, grain size, dislocation and strain of $Cd_{0.4}Pb_{0.6}S$ thin films

T°C	Eg eV	D nm	nm^{-2} ó	ξ
Without annealing	1.7	22	0.008	0.0178
200	1.67	30	00011	0.0134
300	1.65	37	00007	0.028

Results and Discussion

Structural Properties

Fig. 1 and Fig. 2 indicate the XRD spectra of $Cd_xPb_{1-x}S$ (x=0,0.4) thin films annealed at (298, 473, 573)K. The main features of diffraction patterns are similar in case of (x = 0). Peak positions observed agree with the fcc structure of PbS and are represented by Miller indices of (111), (200), (220) and (311) planes of cubic observed at diffraction angles of 25°, 30°, 43° and 53°, respectively. The narrow peaks show that the material has good crystalinty. There is no clear thermal annealing effect on the crystal structure of the compound apart from becoming more accurate. Comparing the XRD patterns of PbS and $Cd_{0.4}Pb_{0.6}S$ films clearly shows a decrease in peak intensities after adding Cd^{+2}; a behavior that can be attributed to the increase in heterogeneity of the film, to host lattice occupation by Cd^{+2} and to decrease the crystalline size to nano-scale levels. Similar results have been found elsewhere [21,24]. In addition, a plane existed that does not belong to either PbS or CdS; thus there must be a solid formation, which is CdPbS in composition. The highest peaks in all deposited thin films were those around (200), which indicates the preferential crystallite orientation. X-ray diffraction analysis showed that $Cd_xPb_{1-x}S$ (x=0,0.4) thin films were polycrystalline in nature and exhibited better crystallization with increasing grain size as the annealing temperature was raised from as deposited to 573 K and no more intense diffraction peaks were observed for the annealed samples. Tables 1 and 2 show that film growth is influenced by adding Cd^{+2} to PbS which causes a reduction in crystalline size. Also, the average crystalline sizes increase with increasing thermal annealing due to decrement in strain and dislocation which are related to the lattice misfit. This tendency is caused by a variation in the crystal structure and inter planar distances of films, which in turn depends on the deposition conditions. Optical microscope Fig. 3(a, b) and Fig. 4(a, b) show a globular structure composite of nano-crystals. This reveals good homogeneity of material on substrate surface and average crystallite size that decreases with adding Cd^{+2} to the bath. Moreover, black color for PbS and brown yellowish color for CdPbS were seen.

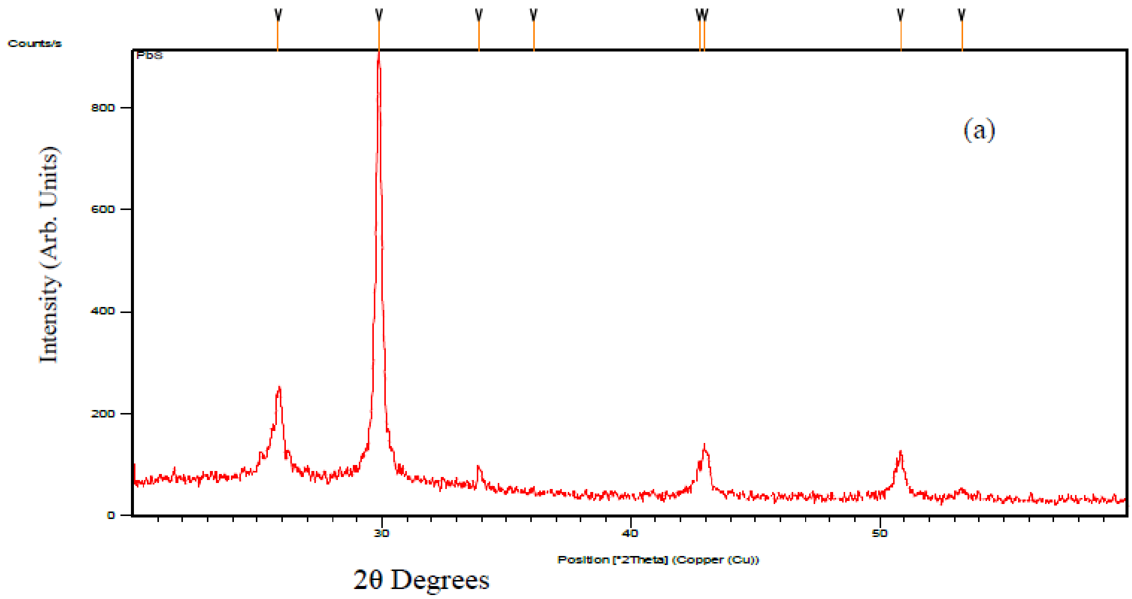

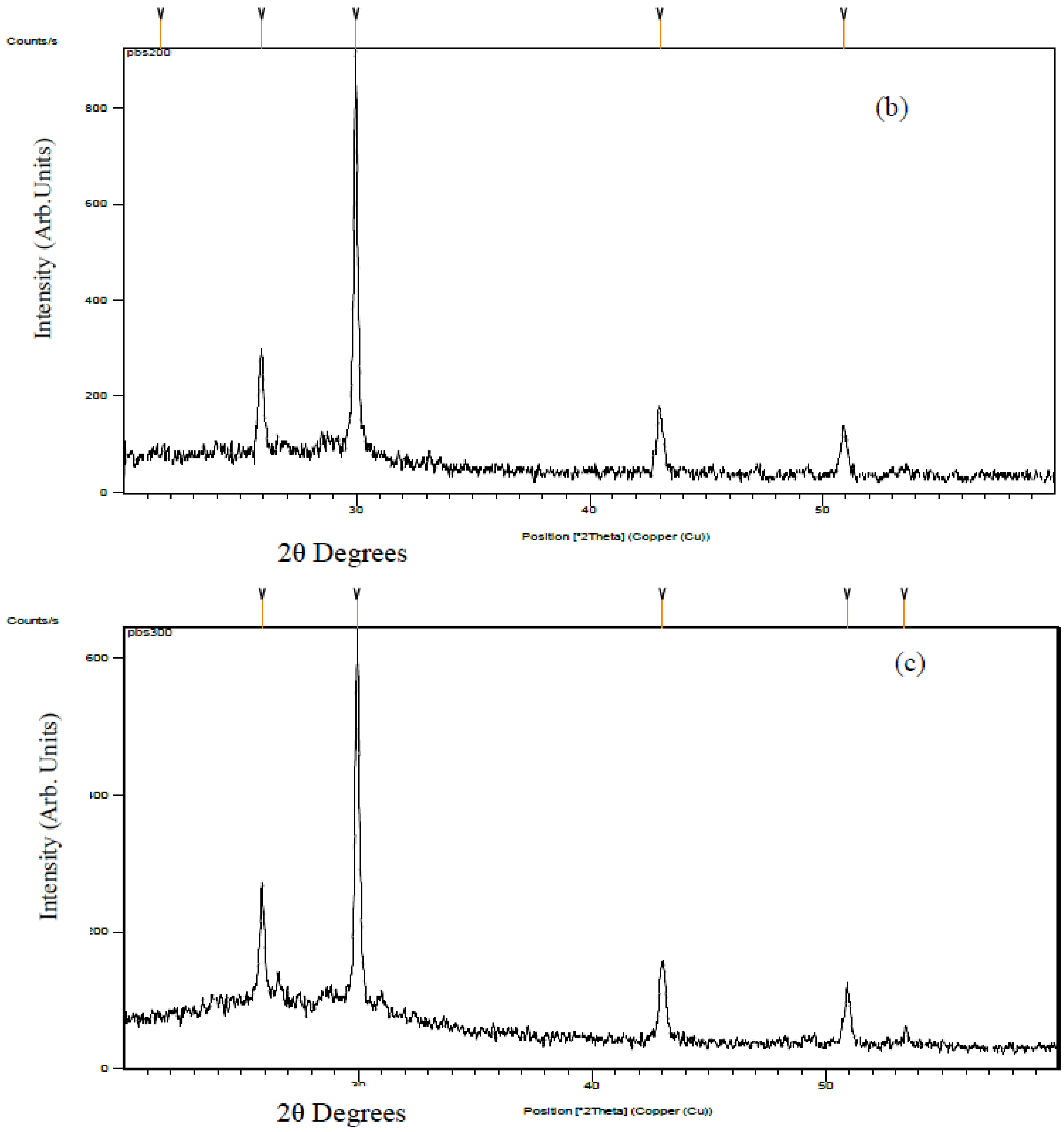

FIG. 1. X-ray diffraction of PbS thin films; (a) as deposited. (b) annealed at 473K. (c) annealed at 573 K.

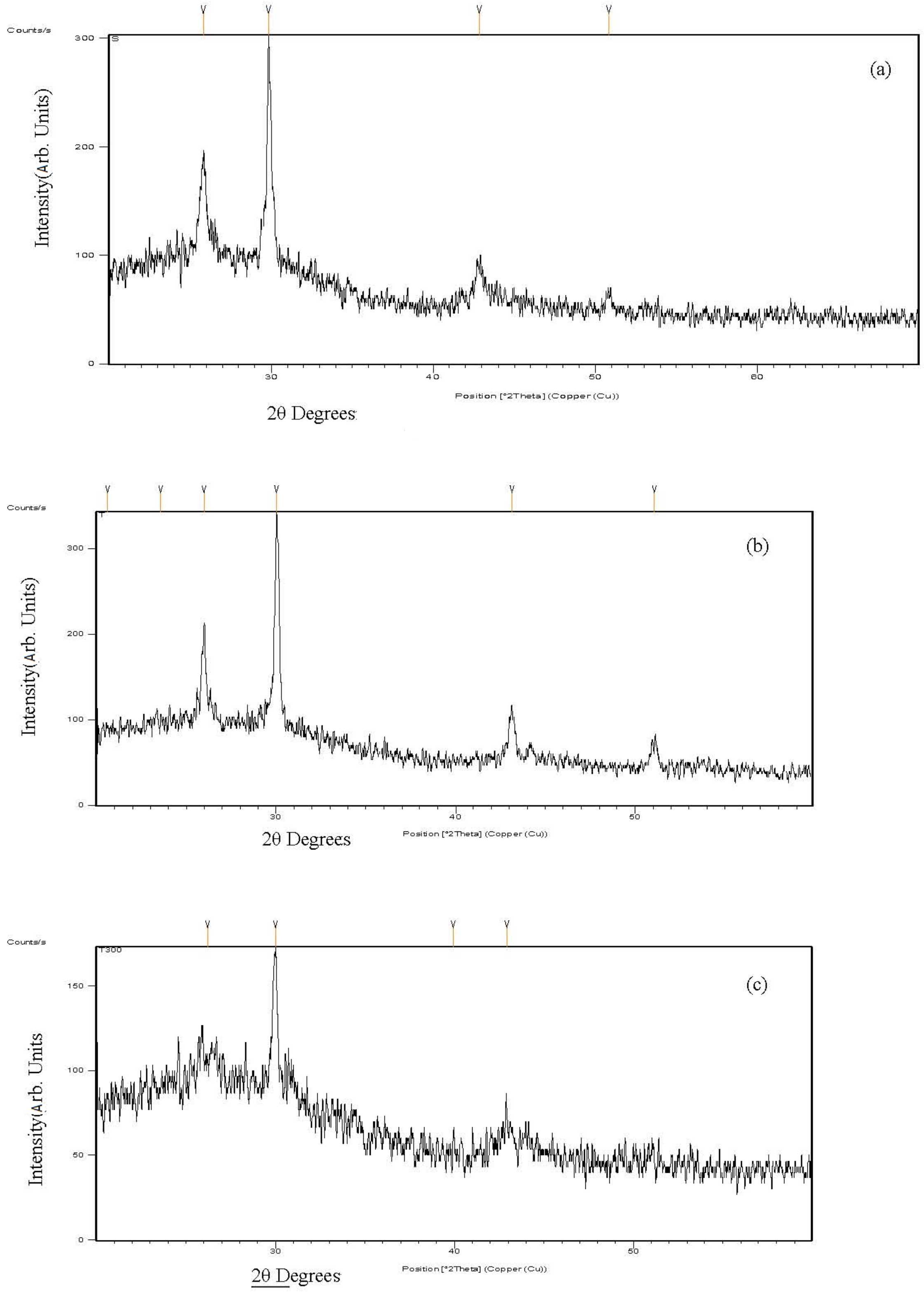

FIG. 2. X-ray diffraction of $Cd_{0.4}Pb_{0.6}S$ thin films; (a) as deposited. (b) annealed at 473K. (c) annealed at 573 K.

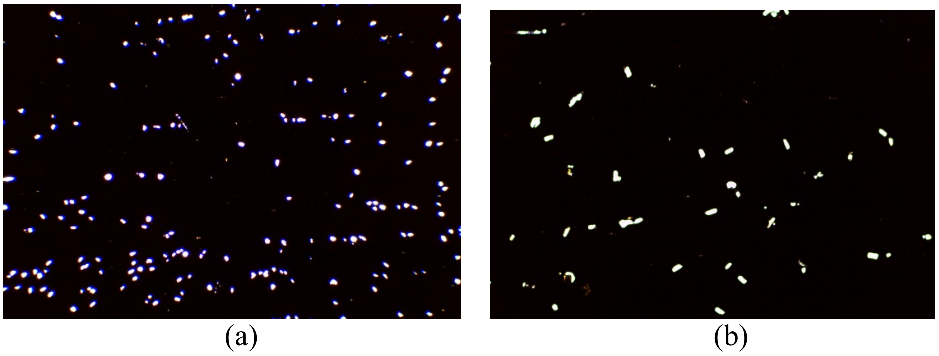

FIG. 3. Photo-microscope image of PbS thin films; (a) 100x. (b) 400x.

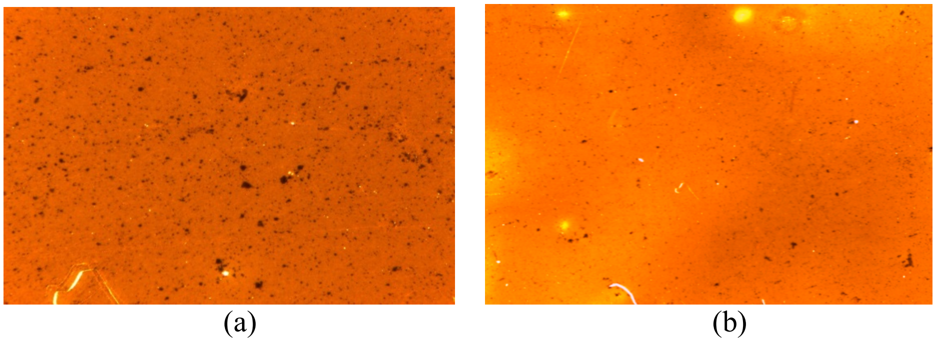

FIG. 4. Photo-microscope image of $Cd_{0.4}Pb_{0.6}S$; (a) 100x. (b) 400x.

Optical Properties

Optical absorbance and transmittance in the UV-VIS-NIR regions of the as deposited and annealed films are shown in Fig. 5(a, b) and Fig. 6(a, b), respectively. Fig. 5(a, b) demonstrates that absorbance is higher for the annealed film than for the as deposited one, while Fig. 6(a, b) reveals an increase in transmittance values for annealed films. This manner is because of some physical effects, such as defect density and structural surface irregularity. The band gap energy was obtained by plotting $(\alpha h\nu)^2$ against photon energy. The linearity of the plot means that these films have a direct band gap material as seen from Fig. 7(a, b). The annealed samples revealed a relative decrement in band gap values, which may result from the reduction in strain within the films or from the increase in grain size. The influence of grain size on the optical band gap arises out of quantum confinement effect [25]. The extinction coefficient (k), which is a measure of the fraction of light lost by scattering and absorption per unit distance in the participating medium, is obtained from the relation $k=\alpha\lambda/4\pi$. The spectral dependence of k, n, ϵ_1, ϵ_2 in Fig. 8(a, b) and Fig. 9(a, b) shows higher k values with increasing photon energy, but lower values with thermal annealing. Refractive index (n) is regarded as one of the essential properties of optical materials due to its correlation with the electronic polarization of ions and local field inside the material. Evaluation of refractive indices of optical materials is substantial for application in some integrated optic devices, such as switches and filters and is a key parameter for the device design [26]. Fig. 9 shows the increase in refractive index value after annealing treatment, which is due to the increase in grain size. Calculation of real and imaginary parts of the dielectric constant was made by applying the relation [27]:

$$\epsilon_1 = n^2 - k^2 \qquad \epsilon_2 = 2nk\ .$$

It is worth noticing that the behavior of ϵ_1 is similar to that of refractive index because of the smaller value of k^2 compared to n^2, while ϵ_2 depends mainly on k values. Fig. 10(a, b) and Fig. 11(a, b) show the variation of ϵ_1, ϵ_2 for as deposited and annealed films. The decrease in ϵ_2 is proposed to enhance the reduction in the concentration of lattice imperfections originating from lattice misfit in the film.

The photo-luminescence emission in semiconductors is affected by the stoichiometric defects in electronic levels. In the current study, since the effect of thermal annealing on photo-luminescence was small, we preferred to take one temperature (573K). Fig. 12 shows the photo-luminescence of nanocrystalline $Cd_xPb_{1-x}S$. When the films are excited at (520) nm, single red emission peaks were observed at wavelengths of (680) nm and (670) nm for PbS and $Cd_{0.4}Pb_{0.6}S$, respectively, which is attributed to both direct recombination and recombination through shallow surface states [28]. The intensity of peaks rises as x content increases. This is because PbS has a narrow band and exceptionally large exciting Bohr radius (-18 nm), which makes it susceptible to charge carrier quantum confinement effects. These features of PbS nano-crystals would prevent them from producing high yield of PL, as most of the energy is lost through non- radiative processes. This enables us to produce high luminescence by either over-coating with a higher band gap material like CdS or by the attachment of ligands [29]. On the other hand, as the particle diameter (D) is reduced for CdPbS, the confinement energy increases and a blue–shift occurs due to the quantum confinement effect [30]. In this study, PL spectrum has a blue-shift with increasing x content by addition of Cd element to PbS, which also may enhance photo-luminescence properties [31], since PbS is weakly luminescent at room temperature [32].

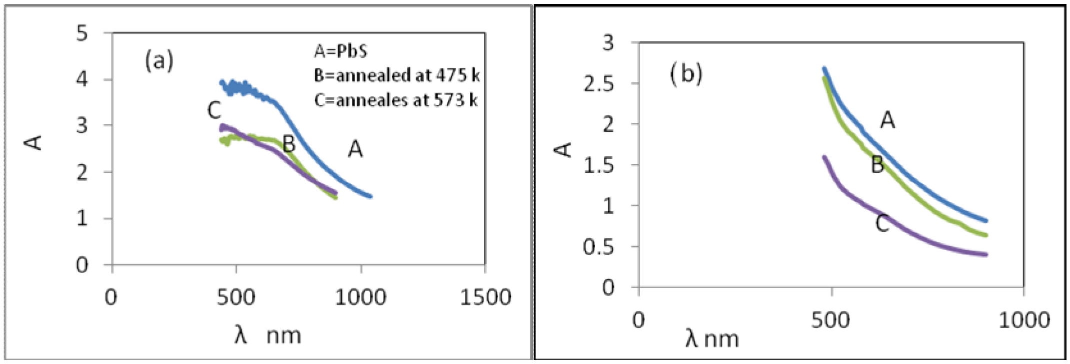

FIG. 5. Absorption spectra of (a) PbS, (b) $Cd_{0.4}Pb_{0.6}S$.

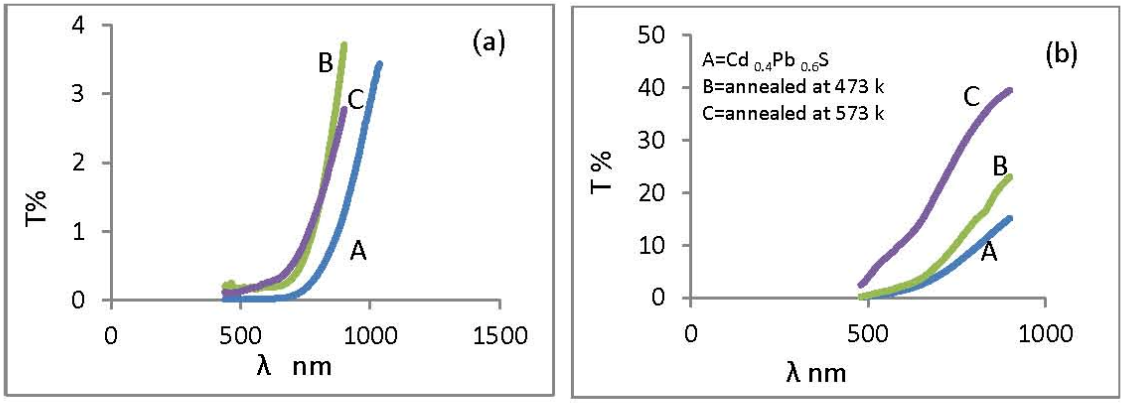

FIG. 6. Transmission spectra of (a) PbS, (b) $Cd_{0.4}Pb_{0.6}S$.

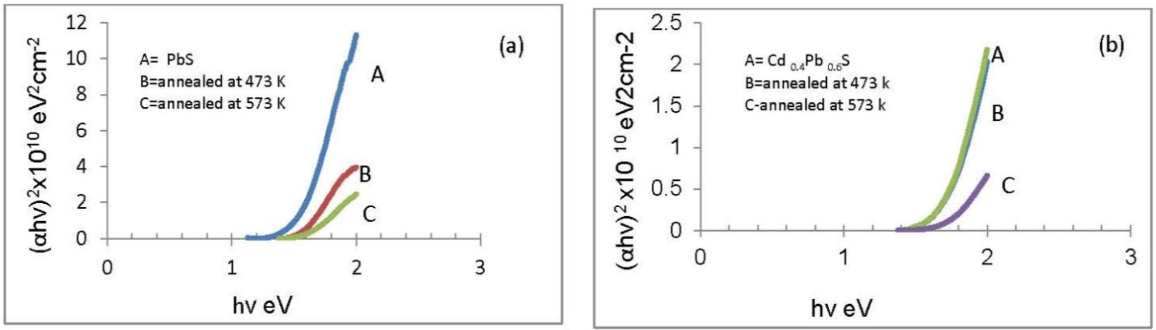

FIG. 7. Plot of $(\alpha h\nu)^2$ *vs*. hν of (a) PbS, (b) $Cd_{0.4}Pb_{0.6}S$ annealed at different temperatures.

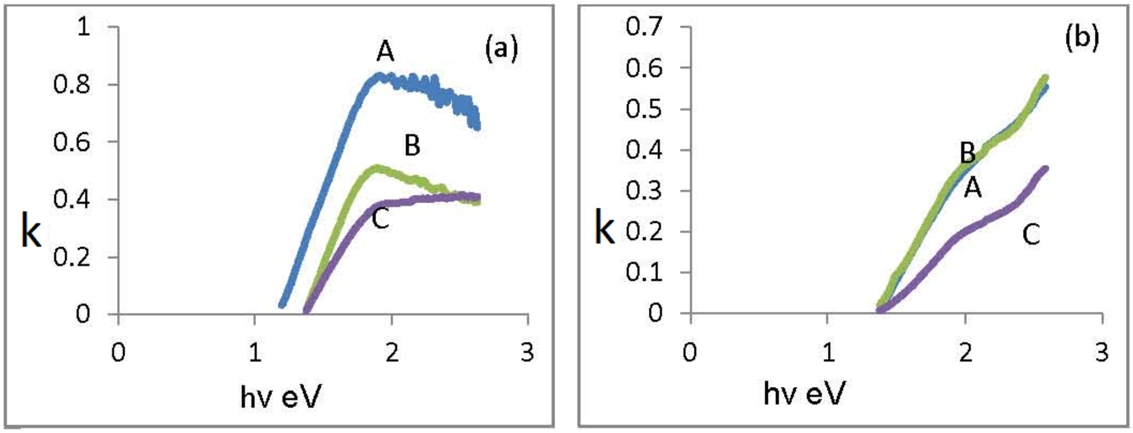

FIG. 8. Plot of k *vs*. photon energy of (a) PbS, (b) $Cd_{0.4}Pb_{0.6}S$ annealed at different temperatures.

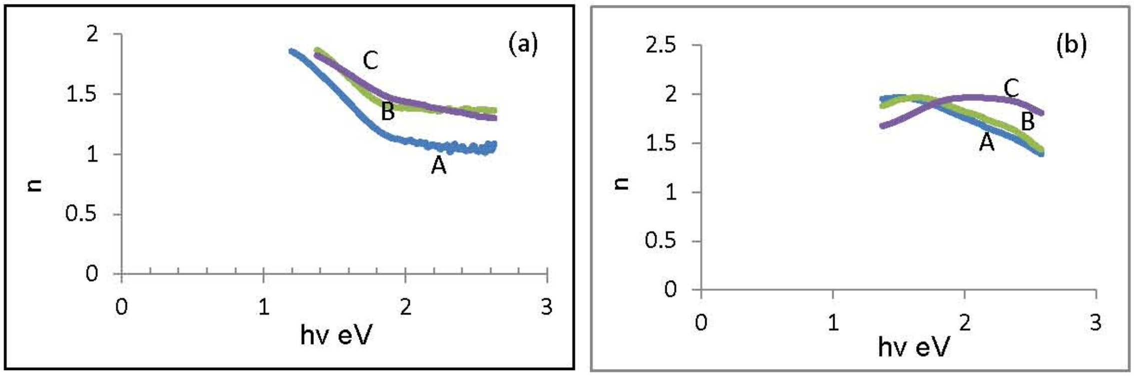

FIG. 9. Plot of n *vs*. photon energy of (a) PbS, (b) $Cd_{0.4}Pb_{0.6}S$ annealed at different temperatures.

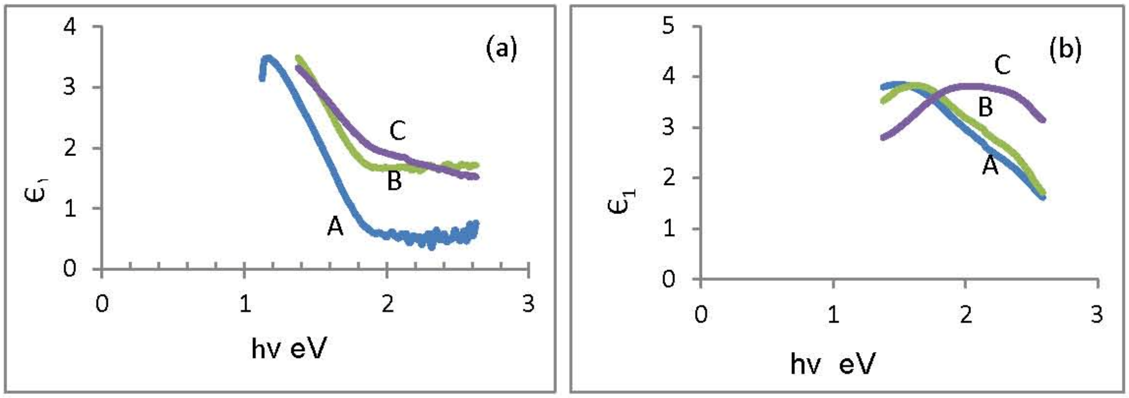

FIG. 10. Plot of Є1 *vs*. photon energy of (a) PbS, (b) $Cd_{0.4}Pb_{0.6}S$ annealed at different temperatures.

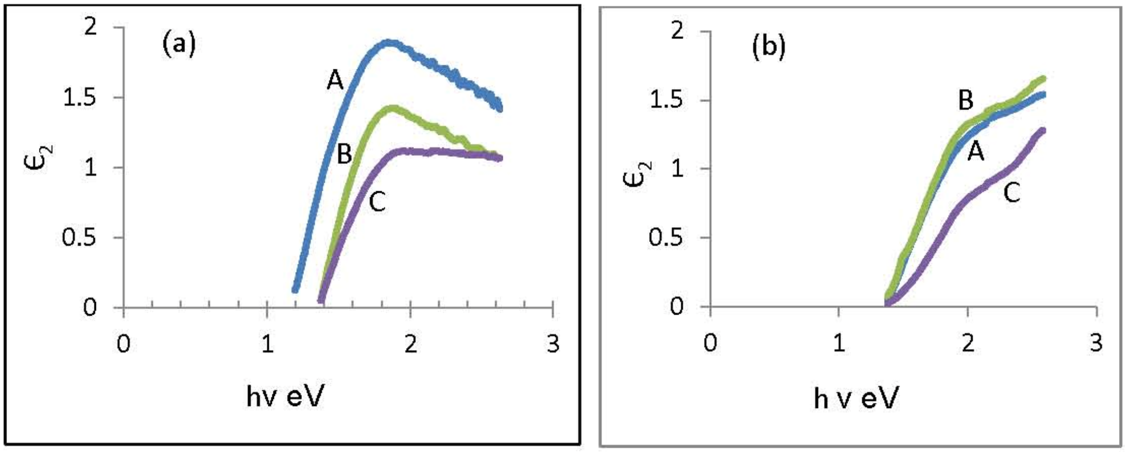

FIG. 11. Plot of €2 *vs*. photon energy of (a) PbS, (b) $Cd_{0.4}Pb_{0.6}S$ annealed at different temperatures.

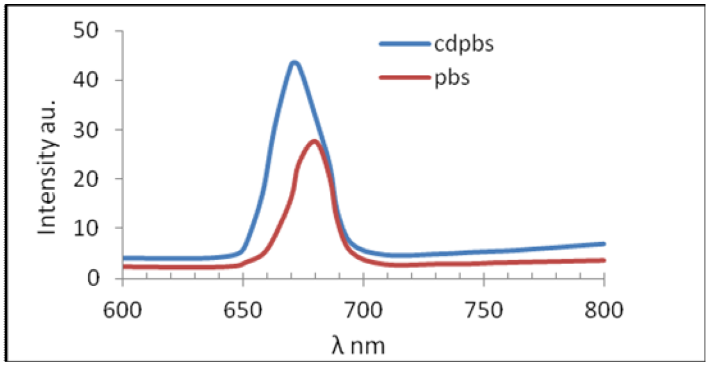

FIG. 12. PL luminescence spectra of PbS and $Cd_{0.4}Pb_{0.6}S$.

Conclusion

Nano-crystalline CdPbS thin films were prepared using chemical bath deposition (CBD) method.Thin films exhibited a good stoichiometry when analyzed by XRD. Also, XRD analysis showed that CdPbS thin films have a cubic structure with predominant (200) orientation. The influence of thermal annealing on structural and optical properties was investigated. It was revealed that the increase in grain size and the decrease in strain and dislocation lead to a decrease in the band gap with thermal annealing. This behavior makes the compound suitable to be used in IR opto-electronic devices. Optical constants, such as extinction coefficient (k), refractive index (n), real and imaginary dielectric constants were calculated. From photo-luminescence spectra, two single peaks for PbS and $Cd_{0.4}Pb_{0.6}S$ were noticed. Moreover, we can improve the weak luminescence of PbS by adding Cd ion to form CdPbS.

Acknowledgements

The first author is thankful to the University of Basra for its help in providing the materials.

Special thanks are also due to Dr. Ihsan S. Mahmood and Dr. Noori S. Jarih for their help in finalizing the presentation of this article.

References

[1] Sankagal, B.R. and Lokhande, C.D., Materials Chemistry and Physics, 14 (2002) 126.

[2] Lui, X. and Zhang, M., J. of Infrared and Millimeter Waves, 21 (2000) 1697.

[3] Nair, P.K., Gomezdaza, O. and Nair, M.T.S., Adv. Mater. Opt. Electron., 1 (1992) 139.

[4] Thangaraju, B. and Kaliannan, P., Semicond. Sci. Technol., 15 (2000) 849.

[5] Nair, P.K., Garcia, V.M., Hernandez, A.B. and Nair, M.T.S., J. Phys. D: Appl. Phys., 24 (1991) 1466.

[6] Zhao, Y., Liao, X.H., Hong, J.M. and Zhu, J.J., Mater. Chem. Phys., 87 (2004) 149.

[7] Sharon, M., Ramaiah, K.S., Kumar, M., Neumann-Spallart, M. and Levy-Clement, C., Electroanal. Chem., 436 (1997) 49.

[8] Akhtar, J., Mailk, M.A., Brien, P. and Wijayantha, K.G.U., J. Mater. Chem., 20 (2010) 2336.

[9] Ubale, A.U., Junghare, A.R., Wadibhasme, N.A. and Daryapurkar, A.S., Turk. J. Phys., 31 (2007) 279.

[10] Seghaier, S., Kamoun, N., Brini, R. and Amara, A.B., Mater. Chem. and Phys., 97 (2006) 71.

[11] Kumar, D. and Agarwal, G., J. of Alloys and Comp., 484 (2009) 463.

[12] Oliva, A.I., Castro-Rodri, R. and Quintana, P., Thin Solid Films, 391 (2001) 28.

[13] Herna, N.B.J. and Vorobiev, Y.V., Mater. and Sol. Cells, B405 (2011) 1882.

[14] Seghier, S., Kamoun, N., Birni, R. and Amara A.B., Mat. Chem. and Phys., 79 (2006) 71.

[15] Frige, D.H., Khan, O.F.Z. and Obrien, P., J. Crys. Growth, 6 (1989) 989.

[16] Nicolon, Y.F. and Dupuy, M., J. Electrochemical Soc., 137 (1990) 2915.

[17] Ray, S.C., Karanjai, M.K. and Dashupta, D., Thin Solid Films, 322 (1998) 117.

[18] Bushan, S., Mukhenjee, M. and Bose, P., J. Mat. Sci., 13 (2002) 581.

[19] Modaffer, A., Mousa, M.A.M. and Ponpon, J.P., J. of Semicond. Tec. and Sci., 9 (2009) 117.

[20] Pentia, E., Draghici, V., Sarau, G. and Mereu, B., J. Electrochem. Soc., 151 (2004) 729.

[21] Thangavel, S., Ganesan, S., Chandramohan, S. and Sudhhagar, P., J. of Alloys and Comp., 495 (2010) 234.

[22] Willeke, G., Dasbach, R., Sailer, B. and Bucher, E.E., Thin Solid films, 271 (1992).

[23] Quadri, S., Skelton, E., Hsu, D. and Dinsmore, A., Phys. Rev. B, 609191 (1999).

[24] Deshmukh, L.P., More, B.M., Rotti C.B. and Shahani, Mat. Chem. and Phys., 45 (1996) 145.

[25] Yu, L., Isobe, T. and Seena, M., Mat. Res. Bull., 75 (1995).

[26] Mahmouda, S.A., Aki, A.A. and Al-Shomar, Physica B, 404 (2010) 2151.

[27] Guneri, E. and Kariper, A., J. of Alloys and Compounds, 516 (2012) 20.

[28] Fernee, M.J., Watt, A., Warner, J. and Cooper, S., Nanotechnology, 15 (2004) 1329.

[29] Warner, J.H., Watt, A.R. and Fernee, M.J., Nanotechnology, 16 (2005) 479.

[30] Dhlamini, M.S., PhD Thesis, University of the Free State (2008).

[31] Patel, A.A., Wu, F.X., Zhang, J.Z. and Torres-Martinez, C.L., J. Phys. Chem. B, 104 (2000) 11598.

[32] Hines, M.A. and Guyot-Sionnest, P., J. Phys. Chem. B, 102 (1998) 3655

Volume 9, Number 2, 2016. pp. 123-130

Jordan Journal of Physics

ARTICLE

Applying Titius-Bode's Law on Exoplanetary Systems

M. B. Altaie, Z. Yousef and **A. I. Al-Sharif**

Department of Physics, Yarmouk University, 21163 Irbid, Jordan.

Received on: 24/7/2016; Accepted on: 24/11/2016

Abstract: We report the application of Titius-Bode's law on 43 exoplanetary systems containing four or more planets. Due to the fact that most of these systems have their planets located within compact regions extending for less than the semi-major axis of Mercury, we found the necessity to scale down the Titius-Bode's law in each case. In this paper, we present sample calculations for three systems out of the whole set. Results show that most systems studied are verifying the applicability of the law with high accuracy. Consequently, our investigation verifies practically the scale invariance of Titius-Bode's law. The results of this study buildup the confidence in predicting positions of the exoplanets according to Titius-Bode's law besides enabling diagnosing possible reasons of deviations.

Keywords: Titius-Bode's law; Exoplanets; Scale invariance.

Introduction

The Titius-Bode's law (hereafter TB law) is a sequence of numbers that was originally set by Johann Daniel Titius in 1766. The sequence is given as 4, 7, 10, 16, 28, 52, 100, …. It was associated at first with the name of Johann Elert Bode, who announced it as a law in a footnote of his book. The above sequence can be taken to indicate approximately the distances of the planets from the Sun measured in AU (the semi-major axis of the Earth's orbit around the Sun). If we just divide the numbers in the sequence by 10, where we get 0.4, 0.7, 1.0, 1.6, 2.8, 5.2, 10, …., this has to be compared with the actual values of the semi-major axis of the planets in the solar system measured in AU: Mercury, Venus, Earth, Mars, Jupiter and Saturn, which are known to be 0.38, 0.72, 1.0, 1.52, 5.2 and 9.54. Historically, the first support for the law came through its role in discovering Uranus, where the position of the seventh planet in our solar system was predicted at 19.6 AU by this law. In 1781, William Herschel found that there is a planet at 19.218 AU which deviates only by 1.9% from the expected distance. Uranus could have been discovered earlier if the TB relation had been taken more seriously [1]. Although the TB law did not give an accurate prediction for the distance of Neptune from the Sun, it played an important role in discovering the Asteroid Belt, where the median of position was predicted with high accuracy. Many modified formulae were presented for the TB law because of the large deviation suffered in its prediction in the case of the outer planets. The first modification was suggested by Wurm in 1803 and the last to date was presented by Pankovic and Radacovic in 2009 [2].

During the last two decades, many exoplanetary systems have been discovered, most of which contain one or two planets, but a large number of systems contain more than three exoplanets. It would be worth to study the spacing between these planets in order to know whether the spacing satisfies the so-called Titius-Bode's law or not. A positive result will provide support for this law and may inspire more studies to find its physical foundation.

The configuration of the discovered exoplanetary systems can be compared with our solar system. In a given multiple exoplanetary

Corresponding Author: M. B. Altaie **Email**: **maltaie@yu.edu.jo**

system, there could be planets that have not been discovered yet. That may occur because of the lack of sufficient data, such as planetary masses or radii that are below the detection limits [3]. Here, the TB law could be a useful tool for making predictions about the positions of exoplanets in multiple exoplanetary systems. This study aims at testing this idea. We first try to check if the multiple exoplanetary systems fit well with the TB law, then we use the law to make predictions about the positions of undetected exoplanets in systems under our study.

Several studies have considered applying the TB law to the spacing between the exoplanets discovered in multiple planetary systems. These studies followed different approaches and have different strategies. Poveda and Lara [4] tried to investigate whether the 5 planets of the 55 Cancri (also called 55Cnc) fit the TB law or not. They found that if the largest known semi-major axis to be allocated for the sixth planet, then the exponential form of the TB law fits well with the five observed semi-major axes for that system. Hence, they predict the existence of a planet at $a = 2.0$ AU in the large gap between the fourth planet ($a = 0.781$ AU) and the sixth planet (at $a = 5.22$ AU). Moreover, they predicted another new planet for the system at $a = 15.0$ AU. After publishing their paper, the semi-major axis for the most inner planet was updated from 0.038 AU to 0.015 AU [6].

Raymond *et al.* [5] mapped out the region in 55 Cancri between the known planets 55Cnc f and 55Cnc d, where an additional planet, designated g, might exist. Because there is a wide region of stability between them, they found that this region can accommodate a Saturn-mass planet which is a giant planet. So, they suggested that there could be even two or three additional planets.

Lovis *et al.* [7] applied the generalized TB relation to multiple exoplanetary systems detected by the radial velocity method only and found reasonable fits. But, they did not make any predictions for positions of new planets.

Cuntz [8] used the TB relation to predict the existence of new planets in the 55 Cancri systems. He predicted the existence of four planets at distances of $0.085, 0.41, 1.50$ and 2.95 AU from their host star. He also predicted the distance of the next possible outer planet in the system to be between 10.9 AU and 12.2 AU. None of the above predictions is observationally confirmed.

Bovaird and Lineweaver [9] studied the applicability of TB relation on a sample of multiple exoplanetary systems containing four planets and more. They found that the majority of their sample adheres to the TB relation more than the solar system does. They inferred that if any system does not follow the TB relation as close as our Solar System, there is a high probability that one or more exoplanets in this system are not detected so far. They used the TB relation to list their predictions for the existence of 141 exoplanets in 68 multiple exoplanetary systems.

Huang and Bakos [3] used the Kepler mission data to search 97 planets of those studied by Bovaird and Lineweaver [9] in 56 multi-planetary systems and found only five planetary candidates around their predictions. They considered that the remaining predicted planets could not be discovered by Kepler mission yet. They concluded that the ability of the TB law at making predictions in extrasolar planetary systems is questionable.

In this article, we present sample calculations for three exoplanetary systems and report a summary of our investigation of 43 systems, showing the results for the adherence to the TB law presented in terms of an average of the fitting percentage. Detailed calculations for the remaining 40 systems are given in Altaie *et al.* [10].

Method

The strategy of our study is based on the understanding that TB law is a configuration description rather than a law with fixed numbers. This means that the numbers given by the law 0.4, 0.7, … etc. are only set as scale configurations. The way that the TB law was deduced confirms this understanding. Accordingly, we feel that a scaling of the configuration is always possible and therefore can be taken as a reference for the application of the TB law, as long as the relative arrangement is preserved. From this point of view, this study is a novel one that could open the door wide for other studies in the field, motivating new constraints on the way exoplanetary systems are configured.

We prepared a survey for the exoplanets reported by NASA Exoplanet Archive about the multiple exoplanetary systems under study. The confirmed exoplanets discovered up to date (21/1/2016) are 1932 planets. 259 of these exoplanets belong to 58 multiple exoplanetary systems (in which the same star hosts more than 3 planets). We have excluded 15 multiple exoplanetary systems with 66 exoplanets for lack of data about their semi-major axes. Our sample contains the remaining 193 exoplanets that are hosted by 43 stars. Thirty five systems hosting 153 of these planets were detected by the transit method, seven systems involving 36 planets were detected by the radial velocity method and only one system (HR8799) with 4 planets was detected by direct imaging. Our data on exoplanets reported in this article are obtained from the NASA Exoplanet Archive (http://exoplanetarchive.ipac.caltech.edu) [11].

TB Law Scaling

We noticed that most of the known exoplanetary systems under study have their planets located within regions of distances less than the semi-major axis of Mercury. This means that we need to scale the TB law for each of those systems. For this purpose, our method was to choose one of the planets of the given system to be satisfying the TB law at a given order of our choice, calculate the scaling factor which comes to be the ratio between the planet's semi-major axis and the corresponding distance in TB law and accordingly go on scaling all the system with the same factor. Such a scaling of the distances may also be understood as a scaling of the measuring units, as we can calculate this factor for any system by dividing the new astronomical unit by the corresponding distance in the TB law. Every individual system has its own scaling factor. The choice of the order of the planet to fit the TB law is done with the best fit and minimum deviation from the distance given by the law for that order.

Once we get the scaling factor, the configuration of the system becomes known to us. Accordingly, we can place the planets in their positions and the order of TB law which we have chosen up to 10 positions. This resulted, in many cases, in leaving some empty positions for planets that are not discovered yet or that even may not have formed at all, as it is the case with the Asteroid Belt. These empty positions are considered as predictions from our point of view.

The justification for our scaling was theoretically validated by Graner and Dubrulle [12], who showed that the law is both scale - and rotation - invariant. This important work has established the theoretical basis for the invariance of TB law. In our work, we see that the scaled exoplanetary systems are indeed satisfying the TB law with high accuracy.

Fitting Results

Out of the 43 systems that we have studied, we will choose only three systems. The first is the one with the best fitting percentage of 97.78% which is Kepler-215 system. The second is arbitrarily chosen from the systems which showed values near the average fitting percent of about 90.4% and the last system is the one which showed the worst fitting percentage of 65.27%, which is Kepler-444 system. Error calculation which is taken as a measure of adherence has been presented in the tables below. This is easily done through calculating the absolute error by taking the absolute value of the difference between predicted and observed values and is presented in column (4) of each table as:

$$abs.error = | observed - predicted |;$$

where it is measured in AU. The relative error is calculated as:

$$rel.error = \frac{| abs.error |}{observed}.$$

The average relative error for all the planets in the system can be then easily calculated producing the adherence of the system to TB law. This is called in the tables the fitting percentage, which is an indication of the adherence of the system to TB law.

$$\begin{aligned} &Fitting\ percentage\ (adherence) \\ &\quad = 100\% - rel.error. \end{aligned}$$

These results are given in the table belonging to each system.

KEPLER-215

This is a G-type star similar to our Sun. Its mass is about 0.98 solar mass with a radius of about 1.0 solar radius and a surface temperature of about $5739\,\mathrm{K}$. This exoplanetary system harbors 4 confirmed planets which were detected by the transit method. The positions of the confirmed planets in the system are as shown in the second column of Table (1). The scaling factor for this system was calculated by positioning the second planet which has a semi-major axis of 0.113 AU in order $n=3$. Accordingly, the scaling factor should be 0.113. The planet configuration becomes as shown in Table (1).

We predict an inner planet at order $n=1$ positioned at 0.0452 AU and the rest of the predicted planets are all in the outer region at 0.5876 AU and beyond. We have shown the absolute and the relative fitting errors marking the deviation from the standard TB law in order to expose the error contribution from each planet. This might be useful in analyzing the pathology of the system and may help designating some reasons for deviations from the TB law. With the suggested configuration, the average fitting percentage for the system is calculated to be 97.78%. If we look at the configuration, we see high similarity with the solar system apart from the scale factor. The fitting result of the planets of this system is shown in Fig. (1).

TABLE 1. The predicted configuration of Kepler-215 system

n	observed (AU)	predicted (AU)	abs. error (AU)	rel. error
1	–	0.0452	–	–
2	0.084	0.0791	0.0049	0.0583
3	0.113	0.113	0.0000	0.0000
4	0.185	0.1808	0.0042	0.0227
5	0.314	0.3164	0.0024	0.0076
6	–	0.5876	–	–
7	–	1.1300	–	–
8	–	2.2148	–	–
9	–	4.3844	–	–
10	–	8.7236	–	–
		Avg. rel. error		2.22%
		Fitting Percent		97.78%

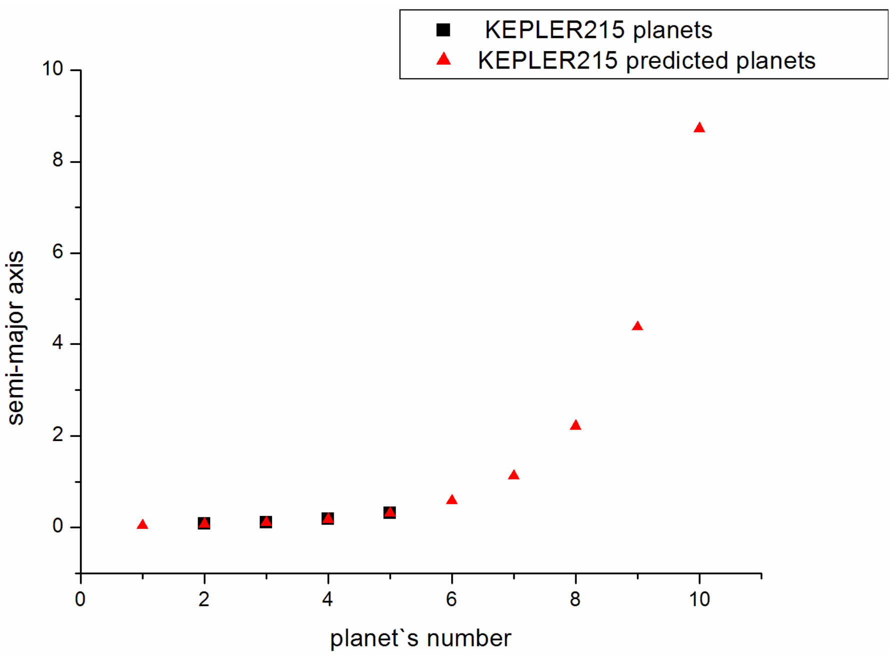

FIG. 1. Fitting of Kepler-215 system.

HD 160691

The star is a G type star, with a mass of about 1.08 solar mass. Its surface temperature is very close to that of our sun at about 5780K. It is older than our sun with an age of about 6.3 Gyr [13]. The system contains four confirmed planets that have been discovered by radial velocity method.

The semi-major axes of the confirmed planets are as shown in the second column of Table (2). The best fitting for the system is obtained when we place the 4th confirmed planet in the 9th position. This makes the scaling factor be 0.13492. Clearly, the system has a very large gap between the 2nd and the 3rd confirmed planet. This could be because there might be planets that are not discovered yet. Consequently, the fitting allows us to predict the existence of several planets: an inner one at 0.0540 AU and three intermediate ones after the second confirmed planet at 0.1349 AU, 0.2159 AU and 0.3778 AU. Two more planets are predicted in the outer region at 1.497 AU and 2.6445 AU. Outer planets at 10.416 AU and more may also exist.

The average fitting percentage for this system is 90.61%, which is within the average obtained for the 43 systems under study. The fitting curve for the system is as depicted in Fig. (2).

TABLE 2. The predicted configuration of HD 160691 system

n	observed (AU)	predicted (AU)	abs. error (AU)	rel. error
1	–	0.0540	–	–
2	0.0909	0.0944	0.0035	0.0386
3	–	0.1349	–	–
4	–	0.2159	–	–
5	–	0.3778	–	–
6	0.9210	0.7016	0.2194	0.2382
7	1.497	1.3492	0.1478	0.0987
8	–	2.6445	–	–
9	5.235	5.2350	0.0000	0.0000
10	–	10.416	–	–
		Avg. rel. error		9.39%
		Fitting Percent		90.61%

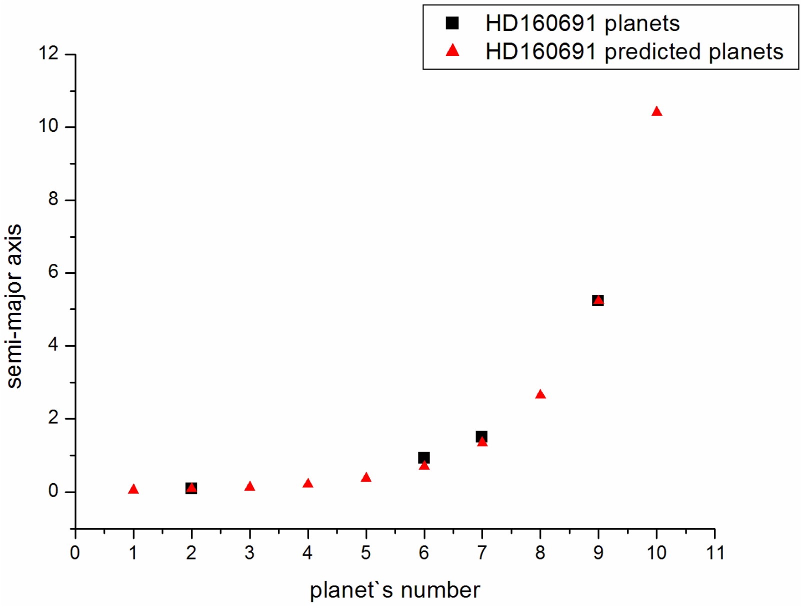

FIG. 2. Fitting of HD160169 system.

KEPLER-444

This is a system with extreme dynamical conditions. It harbors three stars (triple-star system). There are 5 confirmed planets orbiting Kepler-444A which is a K-type star in a tightly packed region. The mass of this primary star is about 0.76 solar mass with a radius of about 0.75 solar radius. This star is believed to be 11.2 Gyr old. This is the oldest star known to date harboring exoplanets. The other two stars (Kepler-444B and Kepler-444C) are small M-type stars orbiting the center of mass of the whole system at a distance of about 40 AU. So, the whole known system is composed of the three stars and the five planets with a size less than that of our solar system. As for the Kepler-444A system, the five planets orbit the host star at distances shown in Table (3). All the predicted planets are in the outer region at 0.2262 AU and beyond.

To obtain a fitting for this system, we found that the best possible fit will be obtained if we position the 4th planet in $n = 4$ of the TB order. This gives a scaling factor of 0.04350. Consequently, we obtain the configuration given in Table (3), where we see that the confirmed planets are arranged sequentially. The fitting percentage is 65.27 %, which is very poor as compared to the fitting percentages of the other planetary systems in this study. The reason is clear; the dynamical setup of the system having three stars at the play makes the system highly unstable. The orbits of this system are coinciding. Orbits of planets c and d, e and f are coinciding. This causes instability in the system. The fitting curve of the system is shown in Fig (3).

TABLE 3. The predicted configuration for Kepler-444

n	Observed (AU)	Predicted (AU)	abs. error (AU)	rel. error
1	0.0418	0.0174	0.0244	0.5835
2	0.0488	0.0304	0.0148	0.3762
3	0.0600	0.0435	0.0165	0.2750
4	0.0696	0.0696	0.0000	0.0000
5	0.0811	0.1218	0.0407	0.5018
6	–	0.2262	–	–
7	–	0.4350	–	–
8	–	0.8526	–	–
9	–	1.6878	–	–
10	–	3.3582	–	–
		Avg. rel. error		34.73%
		Fitting Percent		65.27

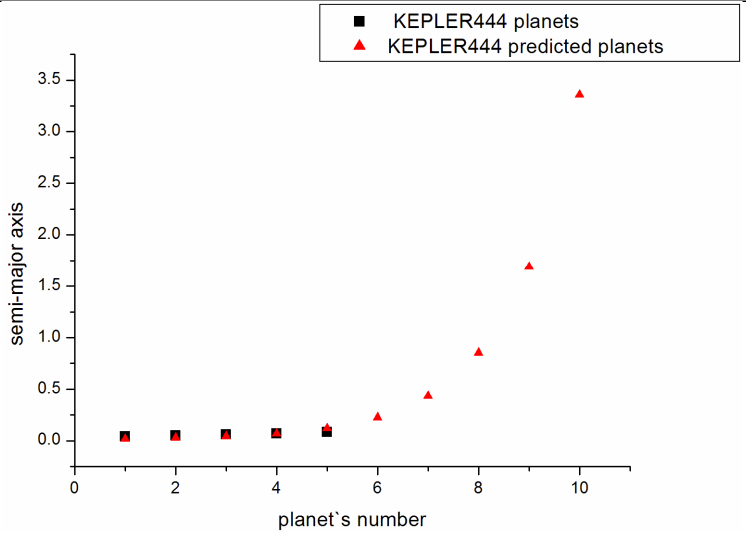

FIG. 3. Fitting of Kepler-444 system.

Discussion and Conclusions

In this article, we have chosen to present three systems out of a set of 43 exoplanetary systems which have been fitted in accordance with the TB law [10]. We find that the majority of our large set adheres to the TB law with an average adherence of about 90.40%. The examples given in this short article have been chosen to show the highest, the median and the lowest of the fitting percentages. Generally, we notice that the adherence to the TB law for exoplanetary systems under our study has different percentages. There are several reasons for these differences; one of them is the age of the system indicated by the age of the hosting star. Young systems with ages of less than 1 Gyr are normally under formation and might not have dynamically settled yet. Such systems suffer jostling during planetary system formation; this is a messy process which can include planetary scattering and migration [9]. This applies to exoplanetary system Kepler-90 (not presented here), which we found to adhere to TB law with a fitting percentage of $72.22\,\%$ and is estimated to have an age of $0.5\,\mathrm{Gyr}$ (Altaie *et al.* 2016). The other reason for deviating from the TB law may happen if the system under consideration may be too old, and consequently may suffer from dynamical changes that affect the positions of the planets in the system. This applies to Kepler-444 system presented above which is thought to be 11.2 Gyr old. Similarly, Kepler-11 system is found to have a fitting percentage of $73.24\,\%$ which is much below the average.

To get an idea about the adherence of our solar system to TB law using the method presented here, we note that the overall fitting percentage obtained is about 85.80%. This is less than the average which we have obtained for the set of 43 systems that we have studied. However, it should be noted that the relative error that we get for Neptune is about 27.46%, whereas the relative errors for the other 7 planets inside the orbit of Neptune including the Asteroid Belt range from 1.0% to 5.26%. If we would include Pluto in these calculations, we find that the relative error in its position is about 95.74%. But, if we exclude Pluto and do not count it as a planet as it was decided by the IAU in 2006, then we obtain a fitting percentage of 94.89%.

The results presented in our study show that, assuming high confidence in the TB law applicability and adherence, we can have systematic speculations in respect of diagnosing the status of some pathological exoplanetary system which show low fitting percentages. Such speculative diagnosis can be tested by observations, including possible errors in observations or calculations. For example, the system Kepler-33 is found to have a fitting percentage of $78.09\,\%$ which is again much below the average percentage for the set considered, despite the fact that it is nearly an ideal system harboring 5 planets with the host star being a Sun-like star with an age of about $4.3\,\mathrm{Gyr}$. This suggests that here we have a pathological case for further studies. Other systems are also analyzed in this respect and could prove that the degree of adherence to TB law might be very useful for analyzing exoplanetary systems.

References

[1] Nieto, M., “The Titius-Bode Law of Planetary Distances: Its History and Theory”, (Pergamon Press, Oxford, New York, 1972).

[2] Flores-Guti'errez, J. *et al*., Revista Mexicana de Astronom'a y Astrof'sica, 47 (2011) 173.

[3] Huang, C. and Bakos, G., MNRAS 442(1) (2014) 674.

[4] Poveda, A. and Lara, P., Rev. Mex. Astron. Astrophys., 44 (2008) 243.

[5] Raymond, S.N. *et al*., Ap. J., 689 (2008) 478.

[6] Winn, J.N. *et al*., Ap. J., 737 (2011) L18.

[7] Lovis, C. *et al*., A&A, 528 (2011) A112.

[8] Cuntz, M., PASJ, 64 (2012) 73.

[9] Bovarid, T. and Lineweaver, C.H., MNRAS, 435 (2013) 1126.

[10] Altaie, M.B., Yousef, Z. and Al-Sharif, A.I., “Verifying the Scale Invariance and the Applicability of Titius-Bode's Law in Exoplanetary Systems”, (2016), in preparation.

[11] NASA Exoplanet Archive. Retrieved on August, 8, 2014 from: http://exoplanetarchive.ipac.caltech.edu

[12] Graner, F. and Dubrulle, B., Astron. Astrophys., 282 (1994) 262.

[13] Soriano, M. and Vauclair, S., Astron. Astrophys., 513 (2010) A49.

Authors Index

A. I. Al-Sharif. 123
A. Khalef 81
A. Shaer 87
F. A. Breuer 103
H. I. Hasan 81
I. M. Ahmed 95
J. A. RABIU. 109
L. A. Latif. 113
M. A. Olaoye 109
M. B. Altaie. 123
M. Elhasan 87
M.K. ELSAID 87
O. A. Jegede. 109
O. A. Lafi. 71
O. O. Adeleke. 109
R. S. Ababneh 103
S. J. Kasim. 113
S. M. Ahmad 113
T. Benkert 103
T. J. Aluko. 109
Y. Y. Kasim 81
Z. Yousef. 123

Subject Index

Activity concentration 109
AEDE 81
Bohr and Mottelson 95
Cancer risk 109
CBD 113
Chalcogenide glasses 71
CR-39 81
Crystallization activation energy 71
D-G relation 95
Differential scanning calorimeter (DSC) 71
Dimensionality of crystal growth 71
Dynamic imaging 103
E-GOS 95
Exchange energy 87
Exoplanets 123
Fat-water separation 103
Free breathing 103
Ground- state band 95
IBM-1 95
IVBM 95
Magnetic field 87
Mean absorbed dose 109
Negative parity band 95
Optical properties 113
PAEC 81
Quantum dots 87
Radon-222 concentration 81
Scale invariance 123
Self-gating 103
The ratio between the energies of I+2 and I states 95
Thermal annealing 113
Thin films 113
Titius-Bode’s law 123
TrueFISP 103
Variational method 87
Vegetables 109
XRD 113

المراجع: يجب طباعة المراجع بأسطر مزدوجة ومرقمة حسب تسلسلها في النص. وتكتب المراجع في النص بين قوسين مربعين. ويتم اعتماد اختصارات الدوريات حسب نظام Wordlist of Scientific Reviewers.

الجداول: تعطى الجداول أرقاما متسلسلة يشار إليها في النص. ويجب طباعة كل جدول على صفحة منفصلة مع عنوان فوق الجدول. أما الحواشي التفسيرية، التي يشار إليها بحرف فوقي، فتكتب أسفل الجدول.

الرسوم التوضيحية: يتم ترقيم الأشكال والرسومات والرسومات البيانية (المخططات) والصور، بصورة متسلسلة كما وردت في النص.

تقبل الرسوم التوضيحية المستخرجة من الحاسوب والصور الرقمية ذات النوعية الجيدة بالأبيض والأسود، على ان تكون أصيلة وليست نسخة عنها، وكل منها على ورقة منفصلة ومعرفة برقمها بالمقابل. ويجب تزويد المجلة بالرسومات بحجمها الأصلي بحيث لا تحتاج إلى معالجة لاحقة، وألا تقل الحروف عن الحجم 8 من نوع Times New Roman، وألا تقل سماكة الخطوط عن 0.5 وبكثافة متجانسة. ويجب إزالة جميع الألوان من الرسومات ما عدا تلك التي ستنشر ملونة. وفي حالة إرسال الرسومات بصورة رقمية، يجب أن تتوافق مع متطلبات الحد الأدنى من التمايز (1200 dpi Resolution) لرسومات الأبيض والأسود الخطية، و 600 dpi للرسومات باللون الرمادي، و300 dpi للرسومات الملونة. ويجب تخزين جميع ملفات الرسومات على شكل (jpg)، وأن ترسل الرسوم التوضيحية بالحجم الفعلي الذي سيظهر في المجلة. وسواء أرسل المخطوط بالبريد أو عن طريق الشبكة (Online)، يجب أرسال نسخة ورقية أصلية ذات نوعية جيدة للرسومات التوضيحية.

مواد إضافية: تشجع المجلة الباحثين على إرفاق جميع المواد الإضافية التي يمكن أن تسهل عملية التحكيم. وتشمل المواد الإضافية أي اشتقاقات رياضية مفصلة لا تظهر في المخطوط.

المخطوط المنقح (المعدَل) والأقراص المدمجة: بعد قبول البحث للنشر وإجراء جميع التعديلات المطلوبة، فعلى الباحثين تقديم نسخة أصلية ونسخة أخرى مطابقة للأصلية مطبوعة بأسطر مزدوجة، وكذلك تقديم نسخة إلكترونية تحتوي على المخطوط كاملا مكتوبا على Microsoft Word for Windows 2000 أو ما هو استجد منه. ويجب إرفاق الأشكال الأصلية مع المخطوط النهائي المعدل حتى لو تم تقديم الأشكال إلكترونيا. وتخزن جميع ملفات الرسومات على شكل (jpg)، وتقدم جميع الرسومات التوضيحية بالحجم الحقيقي الذي ستظهر به في المجلة. ويجب إرفاق قائمة ببرامج الحاسوب التي استعملت في كتابة النص، وأسماء الملفات على قرص مدمج، حيث يعلَم القرص بالاسم الأخير للباحث، وبالرقم المرجعي للمخطوط للمراسلة، وعنوان المقالة، والتاريخ. ويحفظ في مغلف واقٍ.

الفهرسة: تقوم المجلة الأردنية للفيزياء بالإجراءات اللازمة لفهرستها وتلخيصها في جميع الخدمات الدولية المعنية.

حقوق الطبع

يُشكِّل تقديم مخطوط البحث للمجلة اعترافاً صريحاً من الباحثين بأنَ مخطوط البحث لم يُنْشَر ولم يُقَدَّم للنشر لدى أي جهَة أخرى كانت وبأي صيغة ورقية أو إلكترونية أو غيرها. ويُشترط على الباحثين ملء أنموذجٍ يَنُصُ على نقْل حقوق الطبع لتُصبح ملكاً لجامعة اليرموك قبل الموافقة على نشر المخطوط. ويقوم رئيس التحرير بتزويد الباحثين بإنموذج نقل حقوق الطبع مع النسخة المُرْسَلَة للتنقيح. كما ويُمنع إعادة إنتاج أيِّ جزء من الأعمال المنشورة في المجلَة من دون إذن خَطِّيٍّ مُسْبَق من رئيس التحرير.

إخلاء المسؤولية

إن ما ورد في هذه المجلة يعبر عن آراء المؤلفين، ولا يعكس بالضرورة آراء هيئة التحرير أو الجامعة أو سياسة اللجنة العليا للبحث العلمي أو وزارة التعليم العالي والبحث العلمي. ولا يتحمل ناشر المجلة أي تبعات مادية أو معنوية أو مسؤوليات عن استعمال المعلومات المنشورة في المجلة أو سوء استعمالها.

معلومات عامة

المجلة الأردنية للفيزياء هي مجلة بحوث علميّة عالمية متخصصة مُحكمة تصدر بدعم من صندوق دعم البحث العلمي، وزارة التعليم العالي والبحث العلمي، عمان، الأردن. وتقوم بنشر المجلة عمادة البحث العلمي والدراسات العليا في جامعة اليرموك، إربد، الأردن. وتنشر البحوث العلمية الأصيلة، إضافة إلى المراسلات القصيرة Short Communications، والملاحظات الفنية Technical Notes، والمقالات الخاصّة Feature Articles، ومقالات المراجعة Review Articles، في مجالات الفيزياء النظرية والتجريبية، باللغتين العربية والإنجليزية.

تقديم مخطوط البحث

تقدم البحوث عن طريق إرسالها إلى البريد الإلكتروني : jjp@yu.edu.jo

تقديم المخطوطات إلكترونيًا: اتبع التعليمات في موقع المجلة على الشبكة العنكبوتية.

ويجري تحكيمُ البحوثِ الأصيلة والمراسلات القصيرة والملاحظات الفنية من جانب مُحكِّمين اثنين في الأقل من ذوي الاختصاص والخبرة. وتُشَجِّع المجلة الباحثين على اقتراح أسماء المحكمين. أما نشر المقالات الخاصّة في المجالات الفيزيائية النَشِطَة، فيتم بدعوة من هيئة التحرير، ويُشار إليها كذلك عند النشر. ويُطلَب من كاتب المقال الخاص تقديم تقرير واضح يتّسم بالدقة والإيجاز عن مجال البحث تمهيداً للمقال. وتنشر المجلةُ أيضاً مقالات المراجعة في الحقول الفيزيائية النشطة سريعة التغيُر، وتُشَجَع كاتبي مقالات المراجعة أو مُستَكتبيها على إرسال مقترحٍ من صفحتين إلى رئيس التحرير. ويُرفَق مع البحث المكتوب باللغة العربية ملخص (Abstract) وكلمات دالة (Keywords) باللغة الإنجليزية.

ترتيب مخطوط البحث

يجب أن تتم طباعة مخطوط البحث ببنط 12 نوعه Times New Roman، وبسطر مزدوج، على وجه واحد من ورق A4 (21.6 × 27.9 سم) مع حواشي 3.71 سم ، باستخدام معالج كلمات ميكروسوفت وورد 2000 أو ما اسْتَجَد منه. ويجري تنظيم أجزاء المخطوط وفق الترتيب التالي: صفحة العنوان، الملخص، رموز التصنيف (PACS)، المقدّمة، طرق البحث، النتائج، المناقشة، الخلاصة، الشكر والعرفان، المراجع، الجداول، قائمة بدليل الأشكال والصور والإيضاحات، ثَمَّ الأشكال والصور والإيضاحات. وتُكْتَب العناوين الرئيسة بخطٍ **غامق**، بينما تُكْتَب العناوين الفرعية بخطٍ *مائل*.

صفحة العنوان: وتشمل عنوان المقالة، أسماء الباحثين الكاملة وعناوين العمل كاملة. ويكتب الباحث المسؤول عن المراسلات اسمه مشارا إليه بنجمة، والبريد الإلكتروني الخاص به. ويجب أن يكون عنوان المقالة موجزا وواضحا ومعبرا عن فحوى (محتوى) المخطوط، وذلك لأهمية هذا العنوان لأغراض استرجاع المعلومات.

الملخص: المطلوب كتابة فقرة واحدة لا تزيد على مائتي كلمة، موضحة هدف البحث، والمنهج المتبع فيه والنتائج وأهم ما توصل إليه الباحثون.

الكلمات الدالة: يجب أن يلي الملخص قائمة من 4-6 كلمات دالة تعبر عن المحتوى الدقيق للمخطوط لأغراض الفهرسة.

PACS: يجب إرفاق الرموز التصنيفية، وهي متوافرة في الموقع http://www.aip.org/pacs/pacs06/pacs06-toc.html.

المقدمة: يجب أن توضّح الهدف من الدراسة وعلاقتها بالأعمال السابقة في المجال، لا أن تكون مراجعة مكثفة لما نشر (لا تزيد المقدمة عن صفحة ونصف الصفحة مطبوعة).

طرائق البحث (التجريبية / النظرية): يجب أن تكون هذه الطرائق موضحة بتفصيل كاف لإتاحة إعادة إجرائها بكفاءة، ولكن باختصار مناسب، حتى لا تكون تكرارا للطرائق المنشورة سابقا.

النتائج: يستحسن عرض النتائج على صورة جداول وأشكال حيثما أمكن، مع شرح قليل في النص ومن دون مناقشة تفصيلية.

المناقشة: يجب أن تكون موجزة وتركز على تفسير النتائج.

الاستنتاج: يجب أن يكون وصفا موجزا لأهم ما توصلت إليه الدراسة ولا يزيد عن صفحة مطبوعة واحدة.

الشكر والعرفان: الشكر والإشارة إلى مصدر المنح والدعم المالي يكتبان في فقرة واحدة تسبق المراجع مباشرة.

Subscription Form

Jordan Journal of
PHYSICS

An International Peer-Reviewed Research Journal issued by the Support of the Scientific Research Support Fund

Published by the Deanship of Research & Graduate Studies, Yarmouk University, Irbid, Jordan

Name: .... :الأسم

Specialty:...:التخصص

Address: ....:العنوان

P.O. Box:... : صندوق البريد

City & Postal Code: ....:المدينة/الرمز البريدي

Country: ....:الدولة

Phone: ....:رقم الهاتف

Fax No:.. :رقم الفاكس

E-mail:.. :البريد الإلكتروني

No. of Subscription: .... :عدد الإشتراكات

Method of Payment:... :طريقة الدفع

Amount Enclosed:.. :المبلغ المرفق

Signature: ....:التوقيع

Cheques should be paid to Deanship of Research and Graduate Studies - Yarmouk University.

I would like to subscribe to the Journal

For

- ☐ One Year
- ☐ Two Years
- ☐ Three Years

One Year Subscription Rates

	Inside Jordan	Outside Jordan
Individuals	JD 8	€ 40
Students	JD 4	€ 20
Institutions	JD 12	€ 60

Correspondence

Subscriptions and Sales:

Prof. Nehad M. Tashtosh
Deanship of Research and Graduate Studies
Yarmouk University
Irbid – Jordan
Telephone: 00 962 2 711111 Ext. 2075
Fax No.: 00 962 2 7211121

المملكة الأردنية الهاشمية

جامعة اليرموك

المجلة الأردنية
للفيزياء

مجلة بحوث علمية عالمية متخصصة محكّمة
تصدر بدعم من صندوق دعم البحث العلمي

المجلد (9)، العدد (2)، 2016م / 1438هـ

المجلة الأردنية

للفيزياء

مجلة بحوث علمية عالمية محكّمة

المجلد (9)، العدد (2)، 2016م / 1438هـ

المجلة الأردنية للفيزياء: مجلة علمية عالمية متخصصة محكّمة تصدر بدعم من صندوق دعم البحث العلمي، وزارة التعليم العالي والبحث العلمي، الأردن، وتصدر عن عمادة البحث العلمي والدراسات العليا، جامعة اليرموك، إربد، الأردن.

ترسل البحوث إلى العنوان التالي:

الأستاذ الدكتور نهاد محمد طشطوش
رئيس تحرير المجلة الأردنية للفيزياء
عمادة البحث العلمي والدراسات العليا، جامعة اليرموك
إربد ، الأردن
هاتف 00 962 2 7211111 **فرعي** 2075
E-mail: *jjp@yu.edu.jo* **Website**: *http://Journals.yu.edu.jo/jjp*